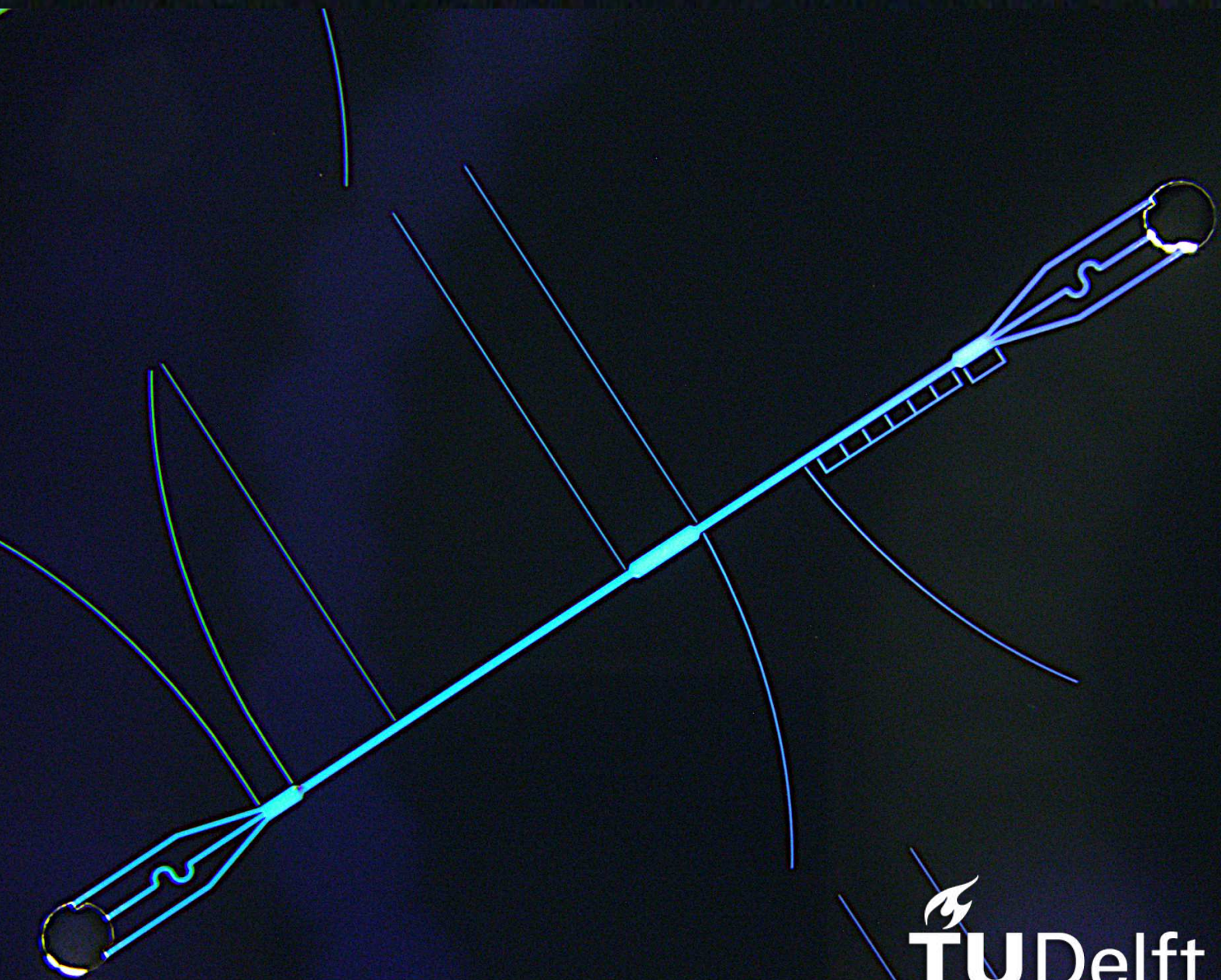


CMUT-based Acoustic Cell Sorting

Jia-Jun Yeh



CMUT-based Acoustic Cell Sorting

by

Jia-Jun Yeh

in partial fulfillment of the requirements for the degree of

Master of Science in Biomedical Engineering

January 24, 2022

Supervisors:	Prof.dr.ir. R. Dekker,	TU Delft, Philips
Daily Supervisors:	Ir. S. Kawasaki, Ir. J. Li,	TU Delft, Philips TU Delft, Philips
Thesis committee:	Prof.dr.ir. R. Dekker, Prof.dr. P.J. French, Prof.dr.ir. J.M.J. den Toonder	TU Delft, Philips TU Delft TU Eindhoven

PREFACE

This thesis is submitted for the degree of Master of Science in Biomedical Engineering at Delft University of Technology. The research described herein was conducted under supervision of Professor R. Dekker, Ir. S. Kawasaki and Ir. J. Li at Philips MEMS MicroDevices department in Eindhoven.

Part of this work has been presented in the following publications:

S. Kawasaki¹, J. Yeh, M. Saccher, J. Li, and R. Dekker, "Bulk Acoustic Based Microfluidic Particle Sorting with capacitive Micromachined Ultrasound Transducers," 35th IEEE International Conference on MEMS, January 9-13, 2022.

ABSTRACT

Particle sorting is an important step in many biological and biomedical techniques. One sorting technique that has received a lot of attention is based on acoustophoresis. Manipulating cells with acoustic forces allows for a sorting method based on physical properties in a non-invasive, label-free, and biocompatible manner. To date, acoustic sorting devices have been developed using either an interdigitated transducer (IDT) or a lead zirconate titanate (PZT) as an acoustic source. IDTs generate surface acoustic waves (SAW) that can sort particles with high precision, however only low throughput is possible. PZT, on the other hand, generates bulk acoustic waves (BAW) that allows for a simple device architecture with high throughput. Nevertheless, the current research done on BAW sorting devices also shows the disadvantage of frequency restrictions.

An attractive alternative to PZT in acoustic sorting devices that has yet to be researched, are the capacitive Micromachined Ultrasonic Transducers (CMUT). CMUTs are well-known for their broad bandwidth, batch production and the possibility for complex designs and integration with electronic circuits. In this work, we present proof-of-concept devices to examine that CMUTs can be used as an acoustic source for particle sorting. Two different acoustic-microfluidic device interfaces were considered, namely the sidewall and the top area of the CMUT. Additionally, the presence of an acoustic pressure within the silicon substrate of the CMUT's die was investigated.

Experiments show that CMUTs generate an acoustic pressure within the silicon substrate of the CMUT's die. This acoustic pressure increased 6.4 times when a phase alignment approach was used compared to when no phase alignment approach was used. Following these findings, acoustic-based sorting devices were assembled to perform particle alignment experiments. It was shown that continuous particle sorting could be demonstrated efficiently for both interfaces by using a pressure field based on standing waves. Additionally, structures integrated into the microfluidic devices, such as a vacuum horn, have the potential to amplify the acoustic signal. These findings indicate that CMUT-based microfluidic devices could provide a promising method for sheathless particle sorting.

Keywords: microfluidics, acoustic separation techniques, bio-applications, bulk acoustic waves, surface acoustic waves

ACKNOWLEDGEMENTS

Completing this thesis, I am deeply grateful to many people who have greatly inspired and supported me throughout my thesis.

In particular, I would like to express my gratitude to my supervisor, Prof. Dr. Ir. Ronald Dekker, for the opportunity to work under his supervision, as well as for his ongoing support and guidance throughout this project. Furthermore, I am grateful for his patience, motivation, and enthusiasm for all of his students. I will not forget those enjoyable and insightful discussions with him during my thesis. I could not have asked for a better mentor for my thesis.

I would like to express my gratitude to Peter Dirksen for providing me with this fascinating and challenging project. Your ideas, which I would never have considered, were very interesting and enjoyable to work on.

In addition, I would like to thank Shinnosuke Kawasaki and Jian Li for being my daily supervisors. This thesis would not be possible without your assistance. I am grateful to Shinnosuke Kawasaki for his guidance and patience in assisting me to understand and carry out my experiments. Despite the fact that I knew very little about my project, he was always eager and willing to help in any way he could. Your vast knowledge of CMUTs and measurement instruments has been extremely helpful. I am grateful to Jian Li, who guided me through the whole process of mask design until the fabrication of the final device. I am also very thankful for the flowchart he made for my designs. Your advice, knowledge, and connections have helped me learn more about microfabrication, which was a completely new field for me, as well as how to work in a cleanroom.

I would also like to thank Dr. Ir. Johan Klootwijk for not only assisting me in arranging the first CMUT samples, but also for his patience and enthusiasm in explaining these devices, as well as his assistance with administrative procedures. I enjoyed our conversation, and I value your advice on my future plans.

My gratitude also goes to Ir. Eugene Timmering for his assistance and support during the assembly and experiments of my device. I am grateful for his amusing jokes and enthusiasm during my stay.

I would like to thank Sieger Swaving, Wouter Dekkers, Marcel Mulder, Bas Jacobs, Hans Huiberts and Micha in 't Zandt. Their generous supports were crucial for the completion of this thesis.

I want to thank Indu for being such a good and funny friend, to whom I could always turn for a quick chat and support. My thanks also goes to Marta, Sevda, Youri, Dino, Eric, Laurent, Sai, Christiaan, Medha and everyone else who helped make my time so memorable.

Finally, I would like to express my gratitude to my family and friends for their faith and continuous support throughout this journey. I am extremely grateful to my parents for their encouragement and trust. I would also like to express my gratitude to my sister and her partner for their great assistance and support while I was in Eindhoven.

CONTENTS

1	INTRODUCTION	3
1.1	Microfluidics	4
1.2	Flex-to-Rigid (F2R) platform	5
1.3	Problem statement and research aim	5
1.4	Thesis outline	7
2	MICROFLUIDIC PARTICLE MANIPULATION	9
2.1	Microfluidics	9
2.2	Acoustic forces acting on particles	10
2.2.1	Primary acoustic radiation force	11
2.2.2	Secondary acoustic radiation force	12
2.2.3	Acoustic streaming	12
2.3	Acoustic resonator	13
2.4	General overview of acoustic-based devices	15
2.4.1	Surface acoustic wave devices	15
2.4.2	Bulk acoustic wave devices	18
2.5	Capacitive Micromachined Ultrasound Transducers	19
3	ACOUSTIC SIDEWALL PRESSURE OF THE CMUT	21
3.1	Excitation of a single element	22
3.1.1	Results	22
3.2	Excitation of multiple elements	26
3.2.1	Results	28
3.3	Particle alignment	30
4	DESIGN AND SIMULATION	33
4.1	Design of the microfluidic devices	33
4.2	Velocity profile in the microchannel	33
4.2.1	Model	35
4.2.2	Results	36
4.3	Simulations of acoustic particle tracing	36
4.3.1	Model	37
4.3.2	Results	38
5	FABRICATION AND ASSEMBLY	43
5.1	The fabrication of the microchannel device	43
5.1.1	Mask design	43
5.1.2	Fabrication process	44
5.1.3	Fabrication results	45
5.2	Experimental setup	47
6	RESULTS	51
6.1	Actuation	51
6.2	Particle alignment approach	52
6.3	Acoustic-microfluidic interfaces	53
6.3.1	Sidewall interface results	53
6.3.2	Top interface results	54
6.4	Conclusion	56
7	CONCLUSION	57
A	OVERVIEW OF DIFFERENT ACOUSTIC-BASED DEVICES	59
B	ACOUSTIC MEASUREMENT DATA	61
B.1	CM12	61
B.2	CM5 phase alignment	63
C	SIMULATION DATA	65
C.1	Velocity profile for CM12-based microchannel	65

c.2	Flow and pressure distribution in CM12-based devices	66
c.3	Particle sorting for CM5-based devices	67
c.4	Particle sorting for CM12-based devices	68
D	FABRICATION DATA	69
D.1	Mask design	69
D.2	Flowchart	70
D.3	Components	71
E	PUBLICATION	73

LIST OF FIGURES

Figure 1.1	Microfluidic cell sorting methods based on precise and large amount sorting [1]	3
Figure 1.2	Schematic overview of microfluidic cell sorting methods [2].	4
Figure 1.3	(a) Standardized IC-based process steps for the fabrication of embedded microchannels. The first two steps consist of etching small holes into a SiO_2 layer and the silicon. The residual silicon is removed with a CF_4 etch. Finally, the hole are closed by depositing a thin layer of SiO_2 and an observation port is formed by deep eching from the back. (b) Cross-sectional view of the embedded microchannels [3].	5
Figure 1.4	The working principle of a CMUT: on the left side the CMUT operates as an ultrasound receiver and the other side the CMUT operates as an ultrasound source [4].	6
Figure 1.5	Schematic overview of the different acoustic-microfluidic device interfaces: (a) microfluidic device next to the CMUT and (b) microfluidic decive on top of the CMUT.	6
Figure 2.1	Schematic overview of acoustic wave propagation in a microfluidic device: (a) BAW propagation, (b) standing SAW propagation and (c) traveling SAW propagation. [5].	10
Figure 2.2	The working mechanism of acoustic forces on particles in a standing wave. (a) Particles are randomly distributed in a channel. (b) By activating ultrasound in the channel, the particles will experience the primary radiation force that move the particles into the pressure nodes. (c) The lateral radiation force align the particle to the center of the acoustic field. When the distance between the particles get close enough, secondary acoustic radiation forces attract the particles to each other. (d) The final outcome is the centered cluster of particles in the middle of the channel [6].	11
Figure 2.3	Influence of the primary acoustic radiation force on polystyrene particles with a diameter ranging from $2.5 \mu m$ to $15 \mu m$. The acoustic wavelength is $375 \mu m$ that corresponds to a frequency of 2 MHz and the acoustic pressure is 0.03 MPa in deionized water. The fluid compressibility, fluid density, particle compressibility and particle density are as $4.58 \cdot 10^{-10} Pa^{-1}$, $1000 kg \cdot m^{-3}$, $2.46 \cdot 10^{-10} Pa^{-1}$ and $1050 kg \cdot m^{-3}$, respectively	12
Figure 2.4	Schematic overview of the Rayleigh streaming with an inner streaming (gray) in the viscous boundary layer (δ_v) and the outer streaming (white) present in a channel with standing waves that propagates in the x direction of $\frac{\lambda}{2}$ with the pressure node at $x = 0$ [7].	13
Figure 2.5	Acoustic resonators: (a) layered resonator and (b) transversal resonator [8].	14
Figure 2.6	(a) Schematic overview of particle sorting using IDTs, where particles propagate from the sidewall to the center.(b) Forces that play a role in particle alignment given at two different locations: (1) particles enters the acoustic field and (2) repositioning of the particles [9].	16

Figure 2.7	(a) Schematic overview of focused IDTs device for standing SAW sorting. (b) Geometry of the focused IDTs where θ is the degree of the arc, R is the radius of the inner IDT finger and O is the focal point. The focused IDTs are positioned symmetrically around the O-axis. (c) Image of the sorting device compared to a coin [10].	16
Figure 2.8	The method of the tilted SAW sorting device for three different particle sizes [11].	17
Figure 2.9	Schematic overview of the traveling SAW device: (a) Spiral microchannel for hydrodynamic focusing of the cells in the center, (b) further alignment of the main flow is performed by two sheath flow and it allows for spacing between the cells and (c) fluorescent-labeled cells are detected by a microscope and acoustically pushed into the sorting outlet [12].	17
Figure 2.10	(a) Schematic overview of the microfluidic device. (b) Working mechanism to sort blood cells from the platelets[13].	18
Figure 2.11	The working principle of a CMUT: on the left side the CMUT operates as an ultrasound receiver and the other side the CMUT operates as an ultrasound source [4].	19
Figure 2.12	The left image illustrates a schematic overview of a CMUT in collapse. The right image outlines the layers of a fabricated CMUT [14].	19
Figure 2.13	Equivalent circuit of a transmitter CMUT. The model consists of an electrical, mechanical and acoustic part [15].	20
Figure 3.1	(a) A schematic overview of the hypothesized acoustic wave generation in silicon-water as a result of the AC voltage on a CMUT in collapsed state. (b) Several CMUT drums operated in collapse mode.	21
Figure 3.2	Experimental setup for transmitting and receiving ultrasound based on Tx CMUT chips (CM5) and a hydrophone. (a) Top view of the acoustic pressure measurement. The optical hydrophone was partly immersed in water at the sidewall of the CMUT. The diameter of a single drum and the pitch between two drums are $355 \mu m$ and $315 \mu m$, respectively. (b) Pressure measurement setup. (c) Schematic of the experimental setup.	23
Figure 3.3	The transient output pressure from element 2 with a driving condition of 150 V bias voltage, 4.4 MHz acoustic frequency and 1 pulse of sine wave.	24
Figure 3.4	Pressure profile of the CM5' sidewall taken from the center point of the die, where the 0.2 mm represents the top and -0.2 mm represents the bottom in the Z-direction. The corresponding parameters are 1 sine wave, frequency of 3 MHz, bias voltage of 150 V and V_{rf} of 30 V.	24
Figure 3.5	Measured acoustic pressure of a single excited CM5 element: (a) Element 2, (b) element 3 and (c) element 4.	25
Figure 3.6	Measured acoustic pressure of a single excited CM12 element: element 94.	26
Figure 3.7	Experimental setup for multiple element excitation, where a CM5 is mounted on a WUP board.	27
Figure 3.8	The relationship between the acoustic velocity and the time delay between each elements.	27
Figure 3.9	Schematic overview of multiple elements excitation with a beam steering technique.	28
Figure 3.10	Attenuation profile in silicon.	28

Figure 3.11	Peak-to-peak pressure with respect to the time delay. The dotted line represents the pressure measured when no beam steering was applied ($\Delta t = 0ns$).	29
Figure 3.12	Peak-to-peak pressure with respect to the velocity: (a) 2 cycles and (b) 15 cycles.	30
Figure 3.13	Schematic overview of a BAW-based particle alignment setup.	31
Figure 3.14	Sorting performance of BAW particle alignment between the sidewall of a CM5 and a reflector using a large amount of $10 \mu m$ diameter polystyrene particles. The top image shows the situation when the transducers were off with no particle alignment. The bottom image was when the transducers were on and particle aligned was visible. This alignment corresponds to half a wavelength in less than 5 seconds.	31
Figure 3.15	(a) Schematic overview of the device with a $375 \mu m$ microchannel at the sidewall of a CM5. (b) The top image shows a clear alignment of $10 \mu m$ polystyrene particles flowing through an open microchannel at a low speed, while the bottom image illustrates the situation after the transducers are turned off and unfocused particles are seen.	32
Figure 4.1	Microfluidic designs for (a) CM5-based microchannels and (b) CM12-based microchannels.	34
Figure 4.2	Simulated cross sectional velocity profile of the fluid flow in the CM5-based microchannel at $z = 20 \mu m$ and inlet velocity of 1 mm/s : (a) scenario 1 and (b) scenario 2.	36
Figure 4.3	3D flow profile taken at the intersection of the three outlets in a rectangular microchannel under condition of an inlet velocity of 1 mm/s : (a) scenario 1 and (b) scenario 2.	37
Figure 4.4	The acoustic boundary sources are shown as the blue selected walls for (a) CM12-based microchannel and (b) CM5-based microchannel.	38
Figure 4.5	Numerical simulation steps necessary for particle simulation.	38
Figure 4.6	CM5-based microchannel design. (a) Velocity distribution of the fluid flow along the streamlines inside the microchannel. Wave plots (red positive, blue negative) of the acoustic pressure field at resonance in a water-filled microchannel with a pressure of 80 kPa and a frequency of (b) 2 MHz (c) 4 MHz	39
Figure 4.7	Particle trajectories inside the CM5-based microchannel for a pressure of 80 kPa and a frequency of 2 MHz at different times: (a) 1 s , (b) 2 s and (c) 3.1 s . A particle scale factor of 3 was applied to make the particle more visible.	41
Figure 5.1	Section of the mask design used to fabricate the microfluidic designs: (a) enlarged section of the squares used to define the microchannel (b) section of a port with the inlets or outlets.	43
Figure 5.2	Fabrication process of the microfluidic channels (cross-section view): (a) silicon wafer and (b) SOI wafer.	44
Figure 5.3	Results after the Si dry etch as SEM cross-sections and top-views of main channels: (a) cross-section at the port of the CM5-based microfluidic design, (b) cross-section at the in- or outlet with the visible square holes in the membrane used to define the microchannel, (c) top-view of the $187.5 \mu m$ microchannel with an intact membrane and (d) top-view of the $375 \mu m$ microchannel with a damaged membrane.	45
Figure 5.4	(a) SEM cross-section of a microchannel. (b) SEM cross-section of $3 \mu m \text{ Si}_2$ PECVD sealing of the membrane	46
Figure 5.5	SEM cross-section for DRIE cycle numbers of (a) 18 and (b) 22.	47

Figure 5.6	Cross-section of the microfluidic setup: (a) CM5-based microfluidic device and (b) CM12-based microfluidic device.	47
Figure 5.7	(a) Overview of the used CMUTs: CM5 (right) and CM12 (left). (b) Top view of CM5 CMUT devices. The diameter of a single drum and the pitch between two drums are $355 \mu\text{m}$ and $315 \mu\text{m}$, respectively.	48
Figure 5.8	(a) Schematic overview of the different acoustic-microfluidic device interfaces: microfluidic device next to the CM5 CMUT devices (left) and microfluidic device on top of the CM5 CMUT devices (right). An acoustofluidic device made of microfluidic chips attached to CMUTs mounted on PCBs: (a) CM5-based microfluidic interface and (b) CM12-based microfluidic interface.	49
Figure 5.9	System overview for (a) CMUT excitation with no phase excitation (Bias Tee connection) and CMUT excitation with phase excitation (WUP board connection). (b) Experimental setup for phase excitation.	50
Figure 6.1	Cross-section overview of the assembled sorting device, showing the microchannel with the CMUTs either attached to (a) the sidewall or (b) on top of the transducers.	51
Figure 6.2	The chosen area of interest (I, II and III) in the microfluidic device for the particle alignment analysis.	52
Figure 6.3	(a) A cross-sectional view of a standing wave in the microchannel with a wavelength of 1λ . Channel width: $350 \mu\text{m}$. Channel depth: $60 \mu\text{m}$. (b) Focusing of $10 \mu\text{m}$ particles after introducing a frequency of 4 MHz in 3 seconds.	53
Figure 6.4	The particle focusing extent is characterized for (a) low particle concentration and (b) high particle concentration. The top image on the left represents the particle distribution at area II. The bottom image is a grayscale variant of the top image after a background filter has been applied. The average gray value profile in the channel width is represented by the curve on the right.	54
Figure 6.5	(a) Cross-sectional views of a standing wave in a microchannel with wavelengths of $\lambda/2$ and 1λ at area II. Channel width: $350 \mu\text{m}$. Channel depth: $60 \mu\text{m}$. (b) Focusing of $10 \mu\text{m}$ particles after introducing a frequencies of 2 and 4 MHz for the top and bottom image, respectively.	55
Figure 6.6	Particle trajectories at area I for a frequency change of 4 to 2 MHz.	55
Figure 6.7	(a) Focusing of particles after introducing a frequency of 2 MHz at area III. (b) The top and bottom grayscale images show particle focusing extent characterized for frequencies of 2 and 4 MHz, respectively. Each average gray value profile in the channel width is shown on the right side.	56
Figure B.1	Measured acoustic pressure of a single excited CM12 element: (a) Element 96, (b) element 94 and (c) element 92.	62
Figure B.2	Measured acoustic pressure of multiple elements excitation of a CM5: (a) reference and (b) phase alignment.	63
Figure C.1	Simulated cross sectional velocity profile of the fluid flow in the CM12-based microchannel at $z=20 \mu\text{m}$ and inlet velocity of 1 mm/s	65
Figure C.2	3D flow profile taken at the intersection of the three outlets in a CM5-based microchannel under condition of an inlet velocity of 1 mm/s : (a) scenario 1 and (b) scenario 2.	66

Figure C.3	CM ₁₂ -based microchannel design. (a) Velocity distribution of the fluid flow along the streamlines inside the microchannel. (b) Wave plot (red positive, blue negative) of the acoustic pressure field at resonance in a water-filled microchannel with a frequency of 8 MHz and applied pressure of 60 kPa.	66
Figure C.4	Particle trajectories inside the CM ₅ -based microchannel for a pressure of 80 kPa and 4 MHz at different times: (a) 0.7 s, (b) 2 s and (c) 3.5 s. A particle scale factor of 3 was applied to make the particle more visible.	67
Figure C.5	Particle trajectories inside the microchannel for 55 kPa at different times: (a) 0.4 s, (b) 1 s and (c) 2.2 s	68
Figure D.1	Mask design of (a) CM ₁₂ -based microfluidic chip and (b) CM ₅ -based microfluidic chip.	69
Figure D.2	Schematic overview of (a) the CM ₅ -based microfluidic device, (b) the glass plate with a specific inner and outer diameter (ID and OD) and (c) the connector block.	71

LIST OF TABLES

Table 2.1	Overview of the speed of sound in different materials.	18
Table 4.1	Overview of the structures used in the microfluidic device with parameters for each microchannel with $\rho_{water} = 997kg/m^3$, $v = 1mm/s$ and $\mu = 0.89mPa \cdot s$	35
Table 4.2	Material properties used to model top-view of microfluidic device.	37
Table 4.3	Overview of sorting efficiencies depending on frequency and flow rate: i and ii represent the CM5-based and CM12-based devices, respectively.	40
Table 5.1	Summary of the fabrication processing steps performed on the front side of the wafers.	44
Table 6.1	Overview of the acoustic interface with their respective CMUT excitation method(s).	52
Table 7.1	Comparison of different acoustic-microfluidic interfaces for particle alignment.	57
Table A.1	Comparison of different acoustic particle separation devices.	59
Table D.1	Summary of processing steps performed on the frontside of all wafers.	70

In the last few years, the interest in a number of emerging medical fields, such as regenerative medicine, personalized medicine, and immunology, have increased substantially. A crucial step in many techniques for these fields is to distinguish, separate and target specific cells, proteins, and other relevant substances. Biological samples are in general a mixture of such substances, where for many applications the importance is in the recognition and separation of specific groups in these samples. Utilizing sorted cells enhances the homogeneity of the sample and decreases the deviation among the analysis. A particular challenge is to sort specific cells at microscale. The analysis of these sorted cells can provide information that plays a significant role for personalized medicine.

Numerous techniques have been developed and are used to sort cells, where the interest in microfluidic devices is rapidly growing. Figure 1.1 divides the microfluidic sorting methods in the ability to sort the number of cells [1]. Precise sorting allows for single cell manipulation (instantaneous force) and only uses active sorting, while large amount sorting allows for the sorting of multiple cells (continuous force) at the same time and uses active and passive sorting.

Opposed to precise sorting methods, large amount sorting methods are especially useful for high sample throughput and to filter out non-relevant substances. The large amount sorting methods are divided into active and passive sorting. Active sorting is based on dielectrophoresis, magnetophoresis or acoustophoresis. The dielectrophoretic sorting method is based on the intrinsic dielectric characteristics of particles. This allows for label-free sorting of particles based on their properties. However, electric fields can harm the cells, which make them less suitable. Magnetophoretic sorting is based on the sorting of magnetic labeled cells by a magnetic field. Nonetheless, this method needs target cell labeling that is hard to remove and it can influence the characteristics of the cells.

In contrast to these methods, the acoustophoretic sorting method is a sorting method that allows for label-free sorting with a minimum effect on the cell viability. It is based on an acoustic source that generates acoustic pressure waves in a mi-

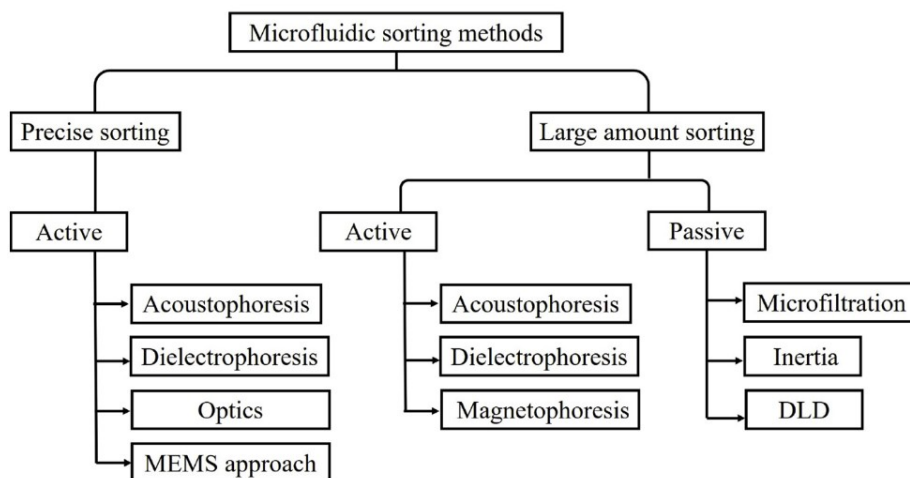


Figure 1.1: Microfluidic cell sorting methods based on precise and large amount sorting [1]

crochannel where particles will either move to an anti-pressure node or a pressure node. Here, particles do not require physical contact to sort, thus providing minimum mechanical impact and a reduced heat conducted from the ultrasound transducers [16]. The acoustic wave propagation in microfluidic devices is classified in surface acoustic waves (SAW) or bulk acoustic waves (BAW) [5]. The compressibility, density, and size of cells in contrast to the medium are important characteristics that determine the trajectory of cells. Summarizing, acoustophoresis is a powerful biocompatible sorting method to manipulate particles that can be used for sorting and separation. Figure 1.2 gives an overview of different cell sorting approaches [2].

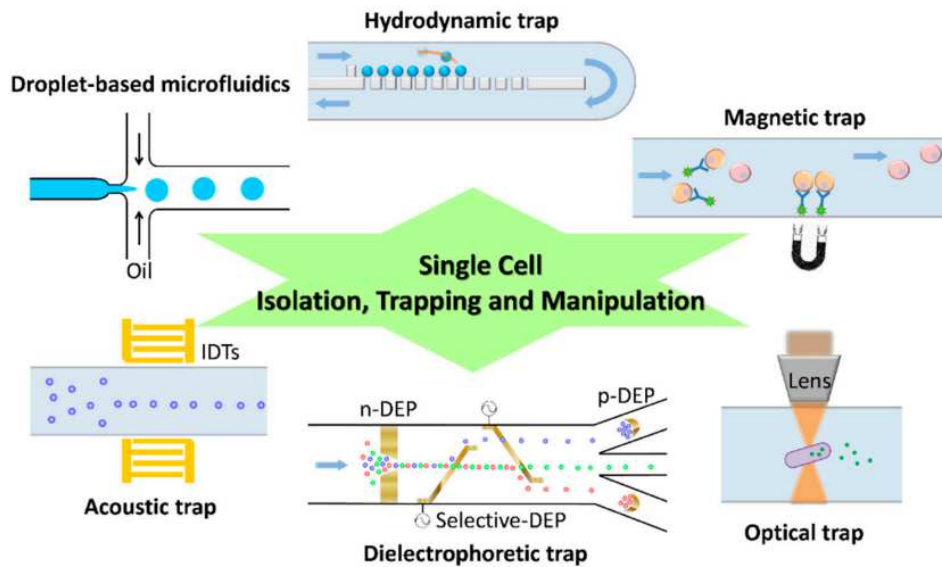


Figure 1.2: Schematic overview of microfluidic cell sorting methods [2].

1.1 MICROFLUIDICS

Microfluidics is the science of precise control and manipulation of the behavior of fluids inside micrometer-sized channels. In microfluidic devices, it is especially useful to analyse physiological and pathological cellular environments on a small scale. To make this process easier, cell sorting can be applied to remove irrelevant particles. Cell sorting is an important technique to separate specific cells in fluid mixed with different cells. In this way, the sorted cells can be used for different purposes such as analysing and experimenting.

The materials used in microfluidics can be divided into Polydimethylsiloxane (PDMS), polymer, silicon, glass, and others. PDMS is currently the dominant material in the microfluidics with a market share of 34.7 % [17]. This material provides the possibility for fast fabrication that is widely used. The main advantages are optical transparency, low cost, and elasticity. However, there are certain limitations for using PDMS, such as the channel deformation due to its high mechanical compliance, absorption of molecules on its surface and penetration of water vapor due to the permeability of PDMS [18; 19]. A suitable alternative is silicon with the advantages of chemical compatibility, electrical conductivity, and surface stability. This additionally allows for the integration of electronics on microfluidic chips [20].

1.2 FLEX-TO-RIGID (F2R) PLATFORM

The silicon processing-based flex-to-rigid (F2R) platform gives the possibility of miniature and flexible integrated circuits (IC) fabrication [21]. This technology is based on connecting silicon devices by polyimide-based interconnects. Minimally invasive instruments can now be made even smaller with the same functionality. Catheters are an example of devices that have been explored with this technology.

The F2R platform not only gives the opportunity to create flexible IC devices, but it can also be used for microfluidic devices [3]. In this fabrication flow, microfluidic channels are formed by using the buried trench patterning on silicon-on-oxide (SOI) wafers as shown in Figure 1.3. General micro-assembly with industrialized techniques can be used to develop IC devices and microfluidic microchannels. This allows the F2R platform to be used for flexible devices and microfluidic devices.

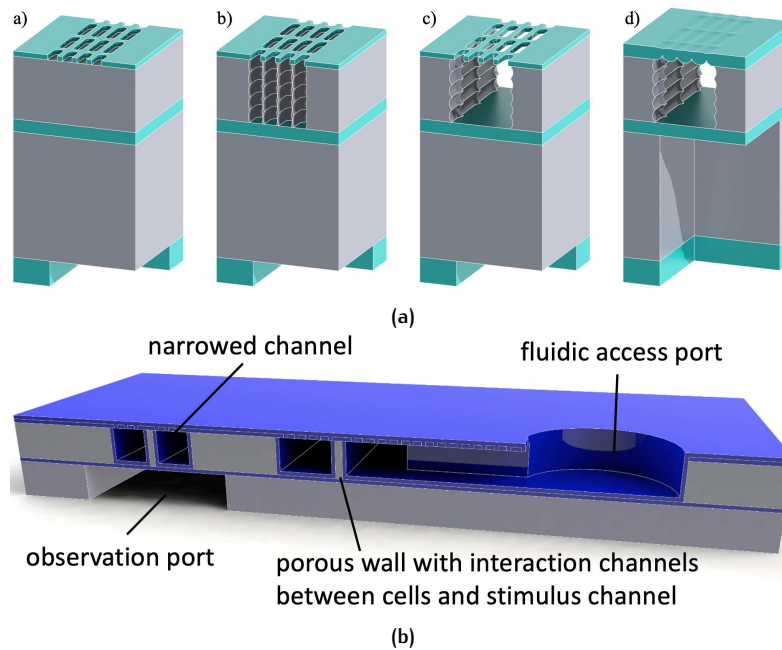


Figure 1.3: (a) Standardized IC-based process steps for the fabrication of embedded microchannels. The first two steps consist of etching small holes into a SiO_2 layer and the silicon. The residual silicon is removed with a CF_4 etch. Finally, the hole are closed by depositing a thin layer of SiO_2 and an observation port is formed by deep etching from the back. (b) Cross-sectional view of the embedded microchannels [3].

1.3 PROBLEM STATEMENT AND RESEARCH AIM

As previously mentioned, the acoustophoretic sorting method is a sorting method with many benefits, such as a label-free and biocompatible sorting system. Two types of acoustic sorting methods are distinguished, namely surface acoustic wave (SAWs) based and bulk acoustic waves (BAWs) based. In SAW-based microfluidic devices, interdigitated transducers (IDTs) play a key role in the formation of acoustic waves in microfluidic channels [9; 12; 22; 10]. IDTs are metal electrodes patterned on piezoelectric material and often operated with frequencies in the megahertz to gigahertz range. These acoustic waves will lead to the generation of Rayleigh SAWs that are leaked into the microfluidic channel. The throughput of the acoustic energy strongly depends on the distance between the transducer and the microchannel and the width of the microchannel.

BAW-based microfluidic devices are acoustic resonators that generally consist of an acoustic transducer and a microchannel with hard walls. These two components are connected by an acoustic impedance matching layer. Microchannels are usually made of materials such as silicon, steel, or glass. The high acoustic impedance of these materials allows for the wall of the microchannel to behave as a reflector due to the mismatch between the fluid and the walls. However, over the past few years only piezoelectric transducers (PZT) have been applied for BAW-based microfluidic devices, which limits the operating condition of the chips [13; 23; 24].

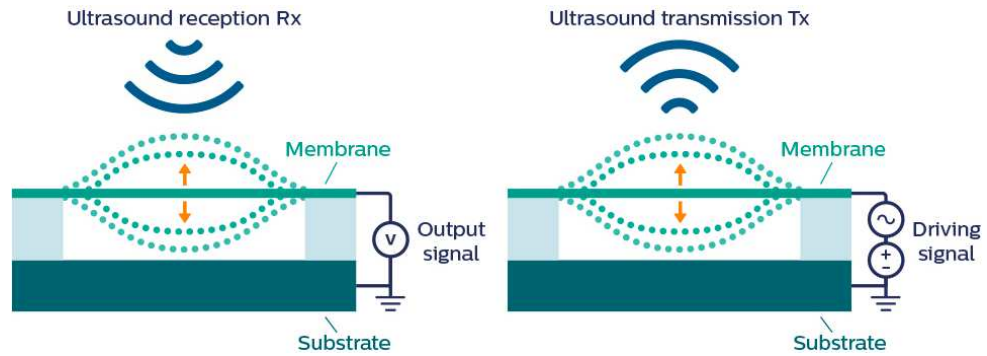


Figure 1.4: The working principle of a CMUT: on the left side the CMUT operates as an ultrasound receiver and the other side the CMUT operates as an ultrasound source [4].

Another acoustic source which has yet to be investigated for microfluidic applications is the Capacitive Micromachined Ultrasound Transducer (CMUT). A CMUT contains a flexible top and fixed bottom plate separated by a vacuum gap [4]. CMUTs can be operated as an ultrasound receiver or transmitter, as seen in Figure 1.4. For an acoustic sorting device, CMUTs are operated in collapse mode, which allows for high efficiency in transmission and receiving modes. An alternating voltage and a bias voltage are applied to generate electrostatic forces, which in turn produces oscillation of the membrane to send ultrasound. The generated ultrasound can couple into the substrate through the collapsed area, and propagates within the silicon substrate. If this is possible, CMUTs can be used as an acoustic source for particle sorting.

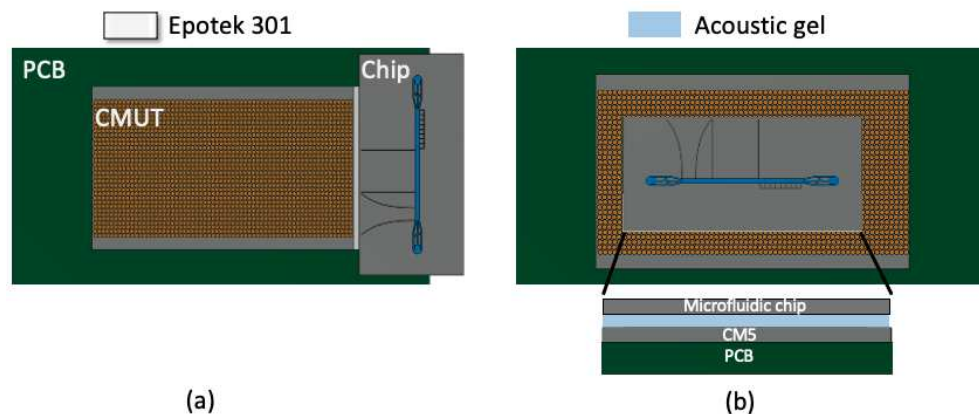


Figure 1.5: Schematic overview of the different acoustic-microfluidic device interfaces: (a) microfluidic device next to the CMUT and (b) microfluidic device on top of the CMUT.

In this work, novel BAW-based sorting devices using CMUTs and F2R are proposed. Two different acoustic-microfluidic device interfaces are considered, namely the sidewall and the area on top of the CMUTs (Fig. 1.5). First of all, the presence of an acoustic sidewall pressure is investigated to determine if this interface is suit-

able for particle sorting. This is followed by designing and simulating the devices to determine if particle alignment is possible. Subsequently, the fabrication of the devices and the particle alignment experiments are performed.

1.4 THESIS OUTLINE

Chapter 2 describes the theoretical background of acoustic-based sorting devices. This includes the different acoustic forces on particles, acoustic resonators and already existing acoustic-based devices. Chapter 3 investigates the presence of an acoustic sidewall pressure in CMUT devices and the possibility to amplify the output pressure. Chapter 4 presents the designs and simulations of the acoustic-based sorting devices required for particle sorting. Chapter 5 describes the fabrication method and results, followed by the experimental setups used for the particle alignment experiment. Chapter 6 presents the results of the particle alignment experiments. Finally, the thesis is concluded in Chapter 7, also including recommendations for future work.

2

BACKGROUND AND METHODOLOGY

Sound is in general the result of the vibration of a body, and it propagates in the form of a wave. The vibration of the particles in a material allows the sound wave to propagate through the material. The human auditory system can hear sound waves with frequencies of up to 20 kHz, whereas frequencies above 20 kHz, known as ultrasound, are not audible. The use of high acoustic frequencies allows for fluid manipulation on the same scale as the micrometer-sized channels of most microfluidic devices. Acoustofluidics describes the technique that integrates acoustic waves in microfluidic systems. Acoustofluidics has a number of advantages, including straightforward fabrication, integration with other integrated circuit components, a quick and powerful fluid actuation, contact-free and non-invasive particle manipulation, and a high biocompatibility [25].

2.1 MICROFLUIDICS

Microfluidics focuses on the behavior of fluids in micrometer-sized channels with the possibility of accurate control and manipulation of particles and their surroundings. Laminar flow in microfluidics is characterized by smooth streamlines, parabolic velocity profiles and particle trajectories in straight and parallel lines [26].

The Reynolds number (Re) predicts if the flow pattern is laminar or turbulent and is defined as

$$Re = \frac{\rho v d}{\eta}, \quad (2.1)$$

where ρ denotes the density of the fluid, v is the flow velocity, d is the characteristic length and η is the fluid viscosity. A Re less than 2000 indicates a laminar flow and the transition to turbulent flow starts at 2000. In microfluidics, the Re is generally less than 100 due to the small dimensions of the microchannels.

Acoustic waves have been extensively applied in microfluidic devices, where the acoustic wave propagation is divided into bulk acoustic waves (BAWs) or surface acoustic waves (SAWs)(Fig. 2.1)[5]. BAWs are acoustic waves propagating through the solid material and create standing waves in microfluidic channel. BAWs are defined as the acoustic wave propagation through the solid material and create standing acoustic waves in the microfluidic channel (Fig. 2.1(a)).

In an acoustic-based device with microfluidic channels, the acoustic impedance for the substrate is in general much higher than the one for the fluid, which is given as

$$Z = \rho c \quad (2.2)$$

where ρ is the density and c is the speed of sound of the material. The fluid-to-solid interface will therefore result in an abundant amount of reflected acoustic waves. The traveling acoustic waves are superimposed on the opposing reflected waves resulting in standing waves in the microfluidic channel. SAWs are characterized in standing SAWs and traveling SAWs. The standing SAWs are created by two acoustic sources or an acoustic source where acoustic waves are reflected (Fig. 2.1(b)). The traveling SAWs illustrate SAWs that move away from the acoustic source (Fig. 2.1(c)). Both BAWs and standing SAW microfluidic devices create standing waves

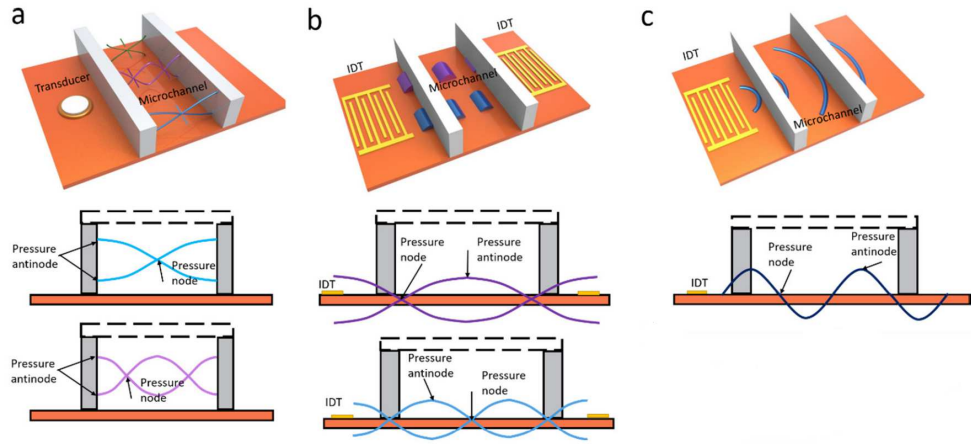


Figure 2.1: Schematic overview of acoustic wave propagation in a microfluidic device: (a) BAW propagation, (b) standing SAW propagation and (c) traveling SAW propagation. [5].

in the microfluidic channel that are characterized by pressure nodes and anti-pressure nodes.

To determine a particle motion relative to a medium, it is important to consider the viscous drag that opposes this motion formed by the laminar fluid flow in the microchannels. Consider a particle that moves with a specific velocity, v_p , through a fluid with a velocity, the viscous Stokes drag, F_{drag} , on the particle is defined as

$$F_{drag} = 6\pi\eta av_p, \quad (2.3)$$

where a is the particle radius [27]. This Stokes' law shows that when a particle radius and/or velocity increases, drag force increases linearly. It is therefore important to consider that drag force is proportional to the particle radius for the influence of the acoustic force on the particles.

2.2 ACOUSTIC FORCES ACTING ON PARTICLES

To understand the influence of acoustic waves on a particle in a microfluidic channel, it is important to distinguish the type of acoustic wave and to describe the forces that play a role on these particles. The acoustic waves formed in the microfluidic channel are either a standing wave or traveling wave depending on the transducer and the materials. The acoustic waves propagating in the microfluidic channel will induce a force on the particles due to the mismatch in acoustic properties of the particle and its surrounding. This force consists of the primary and secondary acoustic radiation force, where the focus will lie on standing waves instead of traveling waves (Fig. 2.2) [5].

Acoustic waves generated in a microfluidic channel are divided into standing or traveling acoustic waves. The traveling acoustic waves are characterized by the generation of waves away from the acoustic source and defined as

$$y(x, t) = A \sin(t \pm kx) \quad \text{with} \quad \omega = \frac{2\pi}{T} \quad \text{and} \quad k = \frac{2\pi}{\lambda}, \quad (2.4)$$

where T is the time period of one wave, A is the amplitude, t is the time, x is the position of the wave displacement and λ is the wavelength.

Standing waves are formed by two opposing propagating waves with the same frequency, amplitude and speed that interfere with each other. These waves are generated by two transducers in opposite directions or one transducer and a reflector. A standing wave is characterized by its confined movement and its fixed pressure

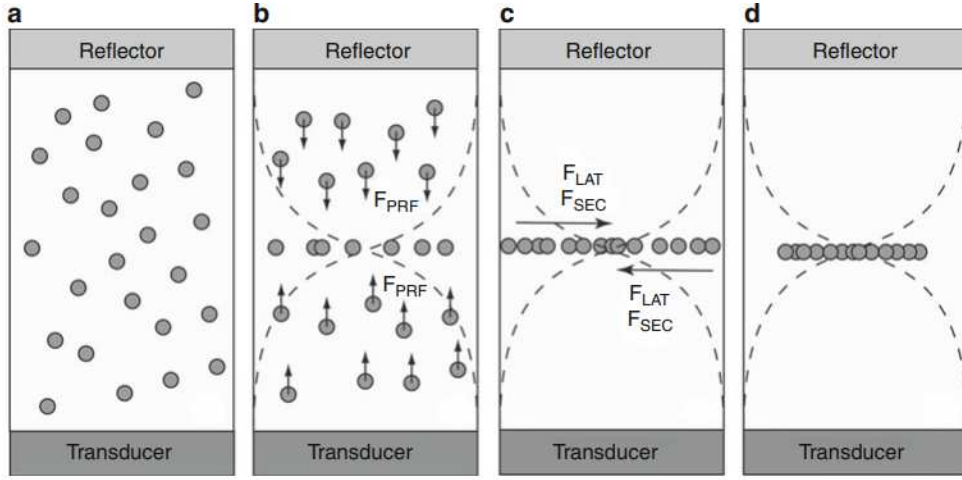


Figure 2.2: The working mechanism of acoustic forces on particles in a standing wave. (a) Particles are randomly distributed in a channel. (b) By activating ultrasound in the channel, the particles will experience the primary radiation force that move the particles into the pressure nodes. (c) The lateral radiation force align the particle to the center of the acoustic field. When the distance between the particles get close enough, secondary acoustic radiation forces attract the particles to each other. (d) The final outcome is the centered cluster of particles in the middle of the channel [6].

and anti-pressure nodes. The anti-pressure node is the location with the highest amplitude (highest displacement), whereas the pressure node has the lowest amplitude (no displacement). The displacement function is given as:

$$y(x, t) = A \cos(kx) \sin(\omega t). \quad (2.5)$$

2.2.1 Primary acoustic radiation force

In acoustic-based sorting devices, the most dominant force used to manipulate particles is known as the primary acoustic radiation force, F_{PRF} . This force is created by standing waves in the microfluidic channel and consists of axial and lateral components. This force consists of axial and lateral components. The axial component (Fig. 2.2(a)) is defined as

$$F_{PRF_{ax}} = -\frac{\pi p_o^2 V_p \beta_m}{2\lambda} \phi(\beta, \rho) \sin(2kx) \quad (2.6)$$

$$\text{with } \phi(\beta, \rho) = \frac{5\rho_p - 2\rho_m}{2\rho_p + \rho_m} - \frac{\beta_p}{\beta_m} \quad \& \quad k = \frac{2\pi}{\lambda},$$

where p is the acoustic pressure amplitude, V_p is the volume of the particle, $\beta_{p/m}$ is the compressibility of particle or the medium, λ is the wavelength of the acoustic wave, ϕ is the acoustic contrast factor, $\rho_{p/m}$ is the density of the particle or the medium, k is the wave number and x is the distance between the particle and the pressure node.

The particle volume, V_p , is proportional to the $F_{PRF_{ax}}$ and is therefore greatly size dependent. This plays a significant role in the behavior of the $F_{PRF_{ax}}$ (Fig. 2.3). The larger the particle diameter, the more the acoustic radiation force will act on the particle. Thus, allowing for faster particle alignment to a pressure node compared to smaller particles. Furthermore, the acoustic contrast factor, ϕ , depends on the density and compressibility of the particle and the medium. If ϕ is positive, the particles will migrate to a pressure node, while for a negative ϕ the particles will move to an anti-pressure node. The lateral component (Fig. 2.2(b)) is defined as

$$F_{PRF_{lat}} = 3d_p^3 \nabla E_{ac} \frac{\rho_p - \rho_m}{\rho_m + 2\rho_p}, \quad (2.7)$$

where ∇E_{ac} is the acoustic energy gradient and d_p is the distance between the central point of the particles. This component is responsible for the attraction movement between the particles in the nodal plane.

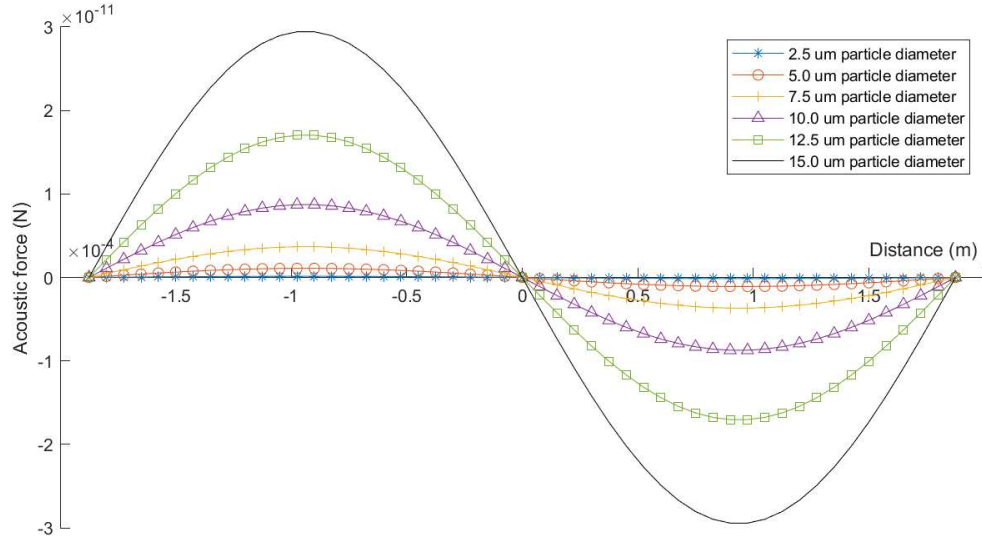


Figure 2.3: Influence of the primary acoustic radiation force on polystyrene particles with a diameter ranging from $2.5 \mu m$ to $15 \mu m$. The acoustic wavelength is $375 \mu m$ that corresponds to a frequency of 2 MHz and the acoustic pressure is 0.03 MPa in deionized water. The fluid compressibility, fluid density, particle compressibility and particle density are as $4.58 \cdot 10^{-10} Pa^{-1}$, $1000 kg \cdot m^{-3}$, $2.46 \cdot 10^{-10} Pa^{-1}$ and $1050 kg \cdot m^{-3}$, respectively

2.2.2 Secondary acoustic radiation force

The secondary acoustic radiation force, F_{SRF} , on a particle is less prominent and is created by the acoustic waves scattering as a result of the surrounding particles (Fig. 2.2(c)). This force is also known as Bjerknes force and becomes relevant if numerous particles are close to each other. It is defined as

$$F_{SRF} = 4\pi a_p^6 \left[\frac{(\rho_p - \rho_m)^2 (3\cos^2\theta - 1)}{6\rho_m d^4} v^2(x) - \frac{\omega^2 \rho_m (\beta_p - \beta_m)^2}{9d_p^2} p^2(x) \right], \quad (2.8)$$

where a_p is the radius of the particle, θ is the angle between the direction of the acoustic wave propagation and the central line that connects the particles, v is the acoustic particle velocity and p is the acoustic pressure. The particles are attracted to each other if F_{SRF} is negative and repulsive if F_{SRF} is positive. Note that the particle attraction depends on both the pressure and velocity and the particle repulsion on the velocity.

2.2.3 Acoustic streaming

Acoustic streaming was first theoretically described by Rayleigh in 1884 and is defined as a steady fluid flow produced by the viscous attenuation of an acoustic wave. This is a drag force on the particles created by the acoustic streaming, where the streaming velocity is at a rate proportional to the square of its frequency. Two common types of acoustic streaming are possible: Eckart and Rayleigh streaming [7]. Eckart streaming is created by the dissipation of acoustic energy in the fluid bulk. During acoustic wave propagation, the wave will attenuate due to the acoustic energy absorption by the fluid. This streaming is usually present in traveling SAWs

as a result of inadequate reflection or alignment. This acoustic energy loss leads to a net force in the direction of acoustic propagation.

Rayleigh streaming occurs due to the acoustic attenuation close to the boundary layers creating a steady flow. It is characterized by the vortex-antivortex for each half wavelength in the acoustic wave direction with a vortex size of $\frac{\lambda}{4}$ (Fig. 2.4). This streaming is especially distinct if

$$\lambda \gg h \gg \delta_v \quad \text{with} \quad \delta_v = \sqrt{\frac{2\nu}{\omega}}, \quad (2.9)$$

where λ is the wavelength, h is the characteristic chamber length, δ_v is the viscous penetration depth, ν is the kinematic viscosity and ω is the angular frequency.

Acoustic streaming is often used as acoustic trapping devices. In microfluidic devices for particle alignment and sorting, this mechanism plays a vital role for nano and sub-micron particles sorting. The particle diameter is therefore important to determine which forces, radiation force or acoustic streaming, play a dominant role. If particles are larger than the critical size, radiation force plays a dominant role and if they are smaller than the critical size, acoustic streaming is dominant.

The viscous drag force as a result of Rayleigh streaming F_R plays a significant role in the lateral direction compared to the axial direction. F_{PRF} generally dominates over F_R in the axial direction, however this is not the case for the lateral direction where the F_{PRF} and F_R are comparable. Note that the volume and the diameter of a particle is proportional to F_{PRF} and F_R , respectively. Furthermore, F_{SRF} plays a role in the formation of the vortices.

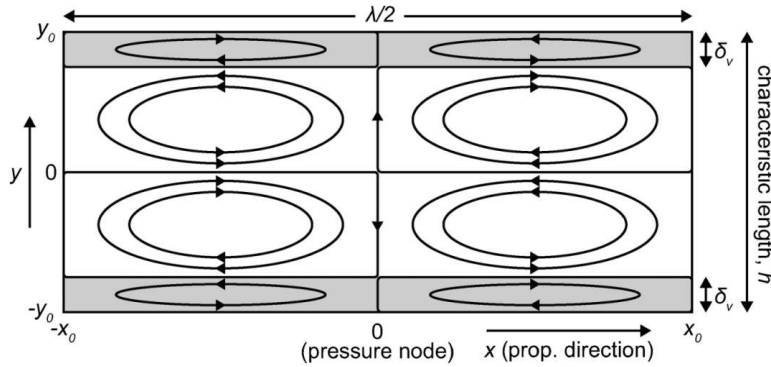


Figure 2.4: Schematic overview of the Rayleigh streaming with an inner streaming (gray) in the viscous boundary layer (δ_v) and the outer streaming (white) present in a channel with standing waves that propagates in the x direction of $\frac{\lambda}{2}$ with the pressure node at $x = 0$ [7].

2.3 ACOUSTIC RESONATOR

In an acoustic-based microfluidic device, different acoustophoretic systems are possible depending on the materials. The main types are the layered resonator, the transversal resonator, and the surface acoustic wave (SAW) resonator [8].

The layered resonator requires specific layers thickness such that the resonator has a high Q-value. The Q-value, also known as the quality factor, describes the ratio between the initial energy stored in the resonator to the energy loss during an oscillation. The main reflection of this resonator takes place between the transducer and the reflector layer that is backed by air.

The transversal resonator works on the principle of reflection between the microchannel walls, thus materials with a high characteristic acoustic impedance are of importance (e.g., silicon or glass). The high Q-value of these materials make the

transversal resonator less sensitive to various thicknesses and matched layers due to the resonance of the whole bulk.

The SAW resonator depends on the SAWs that propagate into the microfluidic channel. In this case, the material requires a similar characteristic acoustic impedance to the medium in such a way that no interfering resonance takes place. Therefore, the resonator type determines the geometry and the material used to create a resonator. The transversal resonator depends to a greater extent on the materials used than the matching layers, which make them more accessible for different designs.

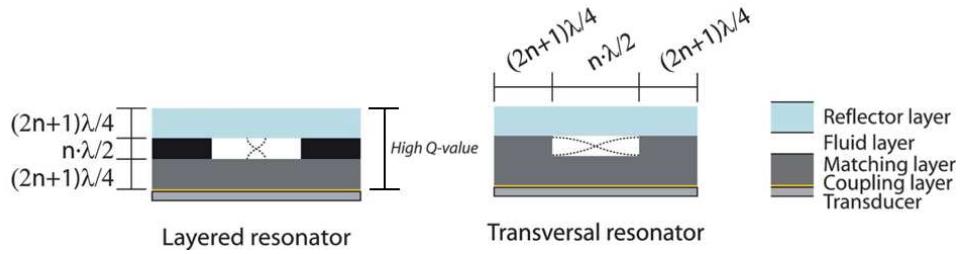


Figure 2.5: Acoustic resonators: (a) layered resonator and (b) transversal resonator [8].

To calculate the reflection and transmission, the characteristic acoustic impedances of the materials are important, which is given as

$$Z = \rho c, \quad (2.10)$$

where the ρ and c correspond to the density and speed of sound of the material, respectively. For normal incidence, the pressure reflection coefficient R_p and transmission coefficient T_p are

$$R_p = \frac{Z_2 - Z_1}{Z_1 + Z_2}, \quad (2.11)$$

$$T_p = 1 - R_p, \quad (2.12)$$

where Z_1 and Z_2 are the acoustic impedances of the first and second medium, respectively. To optimize the acoustic resonator, it is necessary to match the acoustic impedance of these layers, and this decreases the risk of acoustic losses due to reflection and enhances the transmission in the medium.

A BAW-based microfluidic device is identical to a transversal or layered resonator depending on the assembly [28]. By exciting the microfluidic device with the characteristic frequency of the acoustic source, standing waves across the width of the microchannel are formed. This generates a pressure node in the center of the microchannel and anti-pressure nodes at the side walls when a half wavelength is applied. Thus, the width of the microchannel, w_c , is designed with the following equation in mind

$$w_c = \frac{\lambda_m}{2} \quad \text{and} \quad \lambda_m = \frac{v_m}{f}, \quad (2.13)$$

where λ_m corresponds to the wavelength in the medium, which depends on the speed of sound of the medium, v_m and the frequency f , applied by the acoustic source. The most prevalent location of the acoustic source to create a transversal resonator is underneath the microchannel [13; 29; 23]. However, this is not necessary for generating a standing wave in the microchannel. Transversal resonators work in general if the acoustic energy is transferred to the resonator, which in turn develops standing waves. Fornell *et al.* and Gautam *et al.* described the presence of standing waves while exciting the transducer at the side of the microchannel [30; 24]. Nevertheless, it is still important to keep in mind that different positions of an acoustic source can generate different resonance modes.

2.4 GENERAL OVERVIEW OF ACOUSTIC-BASED DEVICES

In the last few decades, acoustic waves have been used to sort particles in microfluidic devices. This is the result of the continuous growing possibilities in microfabrication. Two main acoustic mechanisms are possible to sort particles in microfluidic devices, namely the BAW or SAW mechanism. To give an overview and to make a comparison between research done on previous acoustic sorting devices, Table A.1 summarizes the different acoustic sorting devices based on their method, material, resonance frequency, throughput, and sorting rate.

2.4.1 Surface acoustic wave devices

In SAW microfluidic devices, interdigitated transducers (IDT) generally play a key role in the formation of acoustic waves in microfluidic channels. IDT use metal electrodes patterned on piezoelectric material and are often operated with frequencies of megahertz to gigahertz. These acoustic waves result in the generation of Rayleigh SAWs that are leaked into the microfluidic channel. Snell's law describes the relationship between the speed of sound in the substrate (v_L) and the liquid (v_L) and the angle of the acoustic waves leaking into the fluid (θ_R), defined as $\sin(\theta_R) = \frac{v_L}{v_S}$. These traveling waves can also form standing waves by interference and form pressure nodes and anti-pressure nodes. The particles are moved to one of the nodes depending on the density and compressibility of the particles. Thus, allowing for the possibilities for particle manipulation.

SAW devices are usually made of IDTs patterned on a lithium niobate ($LiNbO_3$) substrate and bonded to a PDMS channel. $LiNbO_3$ is a piezoelectric material that allows for effective electro-mechanical coupling with low BAW and high SAW generation. IDTs are categorized in standard IDTs [9], adjusted IDTs [12; 22] and focused IDTs [10]. The adjusted IDTs have a tapered-finger design with a changing pitch of these fingers from one end to the other. This allows for the variation of resonant frequency over the lateral location along the transducer. The geometry of the focused IDTs depends on the radius of the inner IDT finger, the degree of the arc and the focal point (Fig. 2.7). The width and the spacing between the IDT fingers determine the SAW wavelength. In general, the particles are first hydrodynamically aligned with the use of two sheath flows or a spiral microchannel and afterwards exposed to an acoustic field to sort the particles.

Standing SAW

Standing SAW (SSAW) devices have been extensively used for particle manipulation. The standing waves created by two counter propagating acoustic waves form pressure and anti-pressure nodes as mentioned previously. When particles are exposed to this acoustic field, the primary acoustic radiation force will play a role in the displacement of the particles' location. The nodes created in the microfluidic channel depend on the width of the microchannel and the acoustic wavelength in the fluid. Furthermore, the efficiency of particle sorting in a continuous flow depends on the flow rate that greatly influences the migration time of particles to one of the nodes. It is therefore important to consider these parameters for an optimal particle sorting event. The SSAW devices can be divided in standard SSAW [9; 10] and tilted SAW devices [11].

Shi *et al.* developed two standard IDTs to create SSAWs in a microchannel (Fig. 2.6) [9]. A schematic overview of their device is given in Figure 2.6. The device consists of a hydrodynamic focusing area and an acoustic sorting area. The channel is made of PDMS and bonded on a $LiNbO_3$ substrate with a patterned IDT. For a flow speed of 2.5 mm/s, sorting of up to 13,000 particles were seen in one minute.

Ren *et al.* showed by stimulating focused IDTs a successful polystyrene particle sorting of 10 μm diameter with a throughput of 3300 events/s (Fig. 2.7)[10]. An

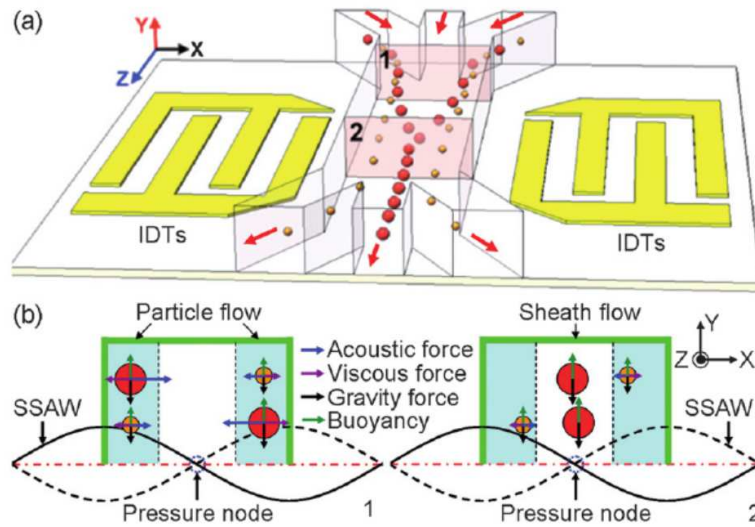


Figure 2.6: (a) Schematic overview of particle sorting using IDTs, where particles propagate from the sidewall to the center. (b) Forces that play a role in particle alignment given at two different locations: (1) particles enters the acoustic field and (2) repositioning of the particles [9].

input power of 31.6 mW (15 dBm) showed sorting of one particle in an actuation time of 72 μ s. Besides the polystyrene particles, an experiment with HeLa cells (mammalian cell model) was performed in an identical setting. Here, cell sorting was possible when a higher input power of 63.1 mW and a longer pulse width of 144 μ s were applied.

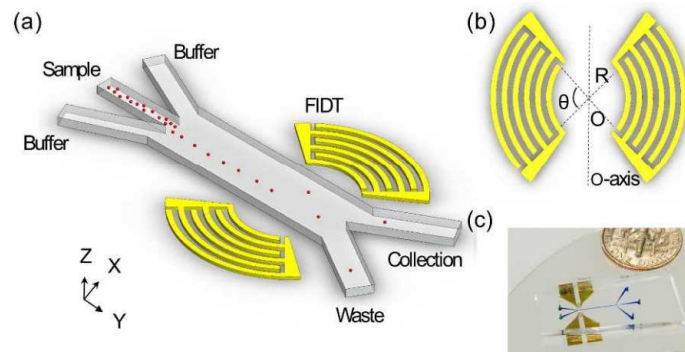


Figure 2.7: (a) Schematic overview of focused IDTs device for standing SAW sorting. (b) Geometry of the focused IDTs where θ is the degree of the arc, R is the radius of the inner IDT finger and O is the focal point. The focused IDTs are positioned symmetrically around the O -axis. (c) Image of the sorting device compared to a coin [10].

Liu *et al.* developed a tilted SAW sorting device with the possibility of sorting different particles sizes at the same time (Fig. 2.8) [11]. Two IDTs are positioned with an angle and parallel from each other. By tilting the IDTs, SSAWs are created with an angle. This allows for particle sorting in the area where the IDTs play a role (shown in Fig. 2.8 as a box around the channel). 1, 5 and 10 μ m particles were properly sorted based on their size due to the acoustic forces that play a role on the particles. The experiment showed for a velocity of 4 mm/s, sorting rates between 90 to 97% for particles with a diameter of 1 to 5 μ m.

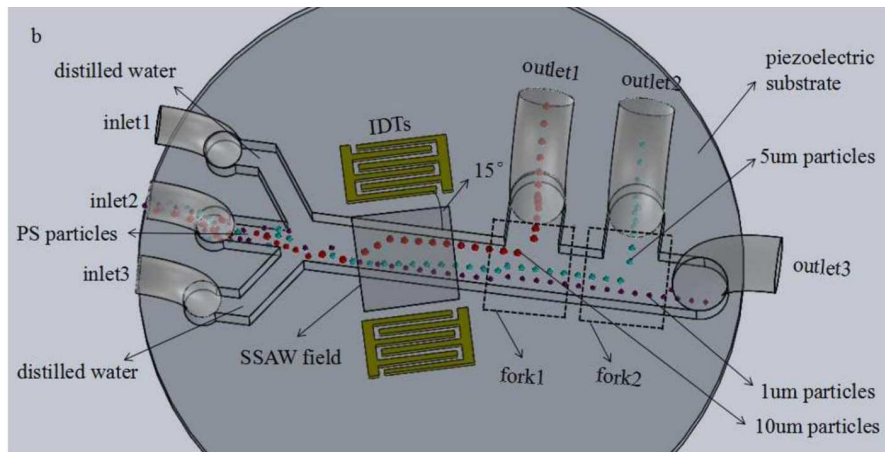


Figure 2.8: The method of the tilted SAW sorting device for three different particle sizes [11].

Traveling SAW

Several researchers have developed traveling SAW sorting devices, which are made up of a single IDT that generates traveling SAWs (TSAWs) [12; 22; 31]. The main difference between SSAW and TSAW is that no boundary limit is applied on the particle translation for the TSAW. This in contrast to the SSAW that is confined to the channel geometry. Thus, TSAW allows for constant particle migration following the direction of the acoustic waves without a limit to the total translation. Both Mutafooulos *et al.* and Franke *et al.* applied the same IDT patterning design to create traveling waves.

Mutafooulos *et al.* made a spiral microchannel and an adjusted IDT that applies a traveling SAW to focus and sort cells (Fig. 2.9) [12]. Hydrodynamic focusing with the use of a spiral microchannel and two sheath flows were performed to focus and space the cells to improve the accuracy of the sorting. For 2,000 events/second, a sorting purity of 90% was achieved due to the TSAW pulse of 25 μ s.

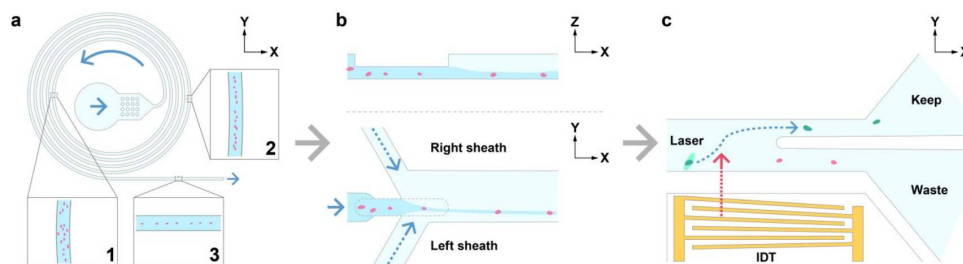


Figure 2.9: Schematic overview of the traveling SAW device: (a) Spiral microchannel for hydrodynamic focusing of the cells in the center, (b) further alignment of the main flow is performed by two sheath flow and it allows for spacing between the cells and (c) fluorescent-labeled cells are detected by a microscope and acoustically pushed into the sorting outlet [12].

Franke *et al.* developed a traveling SAW device based on one IDT to create standing waves in the microchannel [22]. The sorting mechanism is based on two inlet flows that hydrodynamically focus the main flow in the center due to the lower resistance compared to the side flows. Then, the TSAW will move the focused flow into the sorting channel. Sorting of different cells has been realized with this method, including HaCaT cells, fibroblasts, and melanoma cells. However, each cell did show different sorting efficiencies: a sorting efficiency of 100% was achieved if the sorting rates were 0.2, 1 and 2 kHz for melanoma cells, HaCaT cells and fibroblast, respectively.

2.4.2 Bulk acoustic wave devices

BAW microfluidic devices are acoustic resonators that generally consist of an acoustic transducer and a microchannel with hard walls. These two components are connected by an acoustic impedance matching layer. Microchannels are usually made of silicon, steel, or glass. The high acoustic impedance of these materials allows for the walls of the microchannel to behave as a reflector due to the mismatch between the fluid and the walls. For a high acoustic impedance, it is also important to have high density and speed of sound of materials (see overview Table 2.1). Furthermore, a high Q-factor of the materials is important to decrease the energy loss of the acoustic wave. When the microchannel is designed such that the width or depth is equal to $\frac{n}{2\lambda}$ with $n = 1, 2, \dots$ and $\lambda =$ wavelength, the microchannel will behave as an acoustic resonator. Acoustic waves propagating in the microfluidic channel create opposing waves due to the hard walls (reflector) to form standing waves that can be used to manipulate particles.

Material	Density (kg/m^3)	Speed of sound (m/s)	
		Longitudinal	Shear
Silicon	2330	8433	5843
Aluminum	2700	6420	3040
Stainless-steel	7820	5790	3100
Glass (pyrex)	2210	5640	3280

Table 2.1: Overview of the speed of sound in different materials.

Different BAW sorting devices have been developed over the past few years [13; 23; 24]. Chen *et al.* made a BAW sorting device for removing the red and white blood cells from blood [13]. The device consists of a stainless-steel substrate for the microchannel and a customized 1-3 composite transducer glued with epoxy to the bottom of the substrate (Fig. 2.10). At a throughput of 5 ml/min, their experiment showed that 88.4% of the red/white blood cells are removed from the blood. Furthermore, 86.2% of the platelets are recovered.

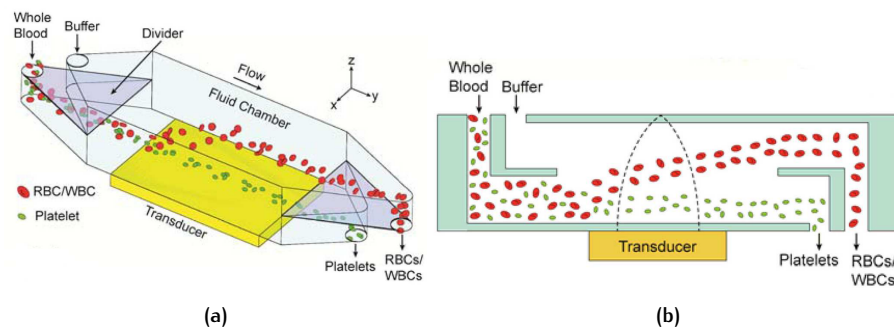


Figure 2.10: (a) Schematic overview of the microfluidic device. (b) Working mechanism to sort blood cells from the platelets [13].

Nilsson *et al.* introduced as one of the first researchers silicon as a resonator chamber [23]. A simple microchannel with one inlet and three outlets was fabricated and sealed with a glass lid. The PZT transducer was positioned at the backside of the channel to create standing waves. The device demonstrated sorting ability for blood samples with an efficiency of up to 90% for a flow velocity < 0.2 mL/min. Fornell *et al.* developed an identical device, however in this case the transducer was glued on topside of the device [24]. They demonstrated a successful separation of particles with positive and negative acoustic contrast factor. The particles with positive acoustic contrast factor move to the pressure node and the particles with the negative contrast factor move to the anti-pressure node.

2.5 CAPACITIVE MICROMACHINED ULTRASOUND TRANSDUCERS

As mentioned previously, the SAW and BAW microfluidic devices are divided into two different mechanisms, where the whole substrate deforms for BAW and the surface of the substrate deforms for SAW. The frequency for SAW-based devices depends on the spacing between the interdigitated finger structures on the surface of the piezoelectric substrate. This in contrast to BAW-based devices, where the thickness of the PZT material determines the frequency. However, both methods use specific frequencies that limits the use for different applications. An interesting alternative is the Capacitive Micromachined Ultrasound Transducer (CMUT). CMUTs are broadband transducers that consists of a flexible top and fixed bottom plate separated by a vacuum gap [4]. CMUTs can be operated as an ultrasound receiver or transmitter, as seen in Figure 2.11.

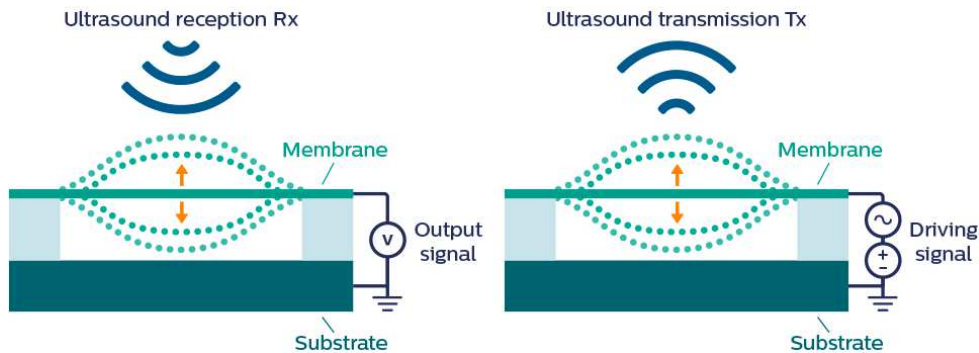


Figure 2.11: The working principle of a CMUT: on the left side the CMUT operates as an ultrasound receiver and the other side the CMUT operates as an ultrasound source [4].

For an acoustic sorting device, the CMUT needs to act as the acoustic source. Thus, the CMUT needs to be operated in collapse mode that allows for high efficiency in transmission and receiving modes. An alternating voltage and a bias voltage is applied to generate electrostatic forces, which in turn produce oscillation of the membrane to send ultrasound. The bias voltage pulls the membrane into collapse, while the RF voltage vibrates the membrane. Figure 2.12 depicts the CMUT in collapse with its parameters and the material layers [14].

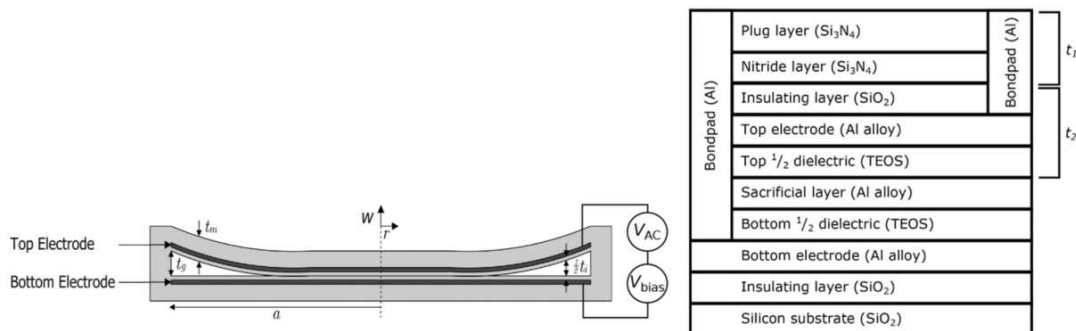


Figure 2.12: The left image illustrates a schematic overview of a CMUT in collapse. The right image outlines the layers of a fabricated CMUT [14].

The energy transformation between the electrical and mechanical domain in transmitter CMUTs is commonly evaluated using the equivalent circuit shown in Figure 2.13 [15]. This model is based on a two-port network consisting of an electrical (current and voltage) and mechanical (velocity and force) port. For a CMUT in

transmitter mode, regardless of the polarity of the bias voltage applied on both electrodes of the CMUT, the membrane will deflect towards the bottom. This is the case if a voltage exceeding the pull-in voltage is applied. One of the most crucial elements is the transformer ratio (n_c) that represents the electromechanical conversion between the two domains.

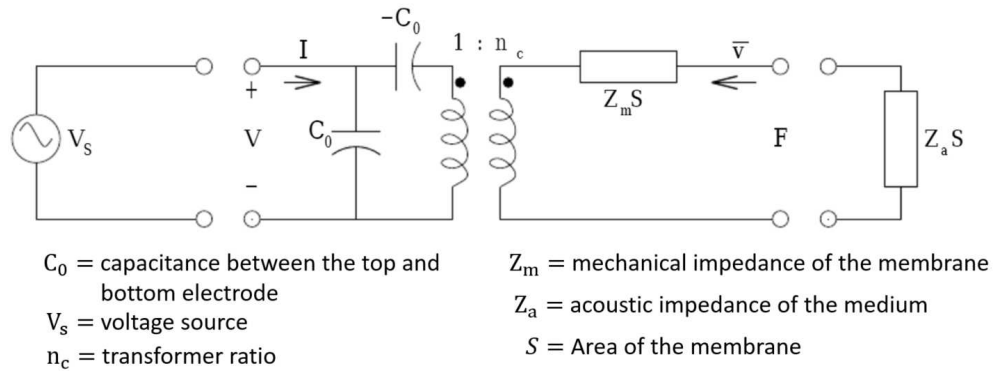


Figure 2.13: Equivalent circuit of a transmitter CMUT. The model consists of an electrical, mechanical and acoustic part [15].

One of the advantages of CMUTs compared to other transducers is the low mechanical impedance compared to fluids over a large frequency range that is related to the thin vibrating membrane [32; 33]. This in turn allows for a broadbanded bandwidth use in immersion applications. Therefore, CMUTs have been used in a variety of medical fields related to *in vivo* medical imaging. In addition, CMUTs use standard IC microfabrication processes that allow for low-cost batch production, and the possibility for complex designs and integration with electronic circuits.

3 | ACOUSTIC SIDEWALL PRESSURE OF THE CMUT

The following chapter investigates the presence and behavior of acoustic pressure at the side of a CMUT chip. Figure 3.1a gives an overview of a hypothesized scenario where ultrasound propagates through silicon by exciting the CMUTs. The CMUTs were operated in collapse mode by applying a bias voltage to pull the top membrane towards the bottom, forming a contact area between the membrane and the silicon substrate (Fig. 3.1b). The alternating voltage between the two electrodes generates an electrostatic force, which causes the membrane to vibrate, resulting in acoustic waves. The contact area allows the acoustic wave to couple into the silicon and radiate away from the CMUT, where a part of it will couple into the water at the sidewall of the CMUT.

The first section looks into whether acoustic pressure can be generated at the sidewall of a CMUT chip and how CMUT operating conditions affect this signal. The second section investigates whether acoustic pressure can be amplified by means of phase alignment. Finally, by taking into consideration the crystal orientation of the silicon die, we investigate whether the surface acoustic wave or the bulk acoustic wave is playing the dominant role in generating the acoustic pressure. The focus will lie on two types of CMUTs: CMUT chips with 64 elements (CM5) and CMUT chips with 96 elements (CM12). Each row, which consists of several CMUT drums, is referred to as an element (Fig. 3.2a).

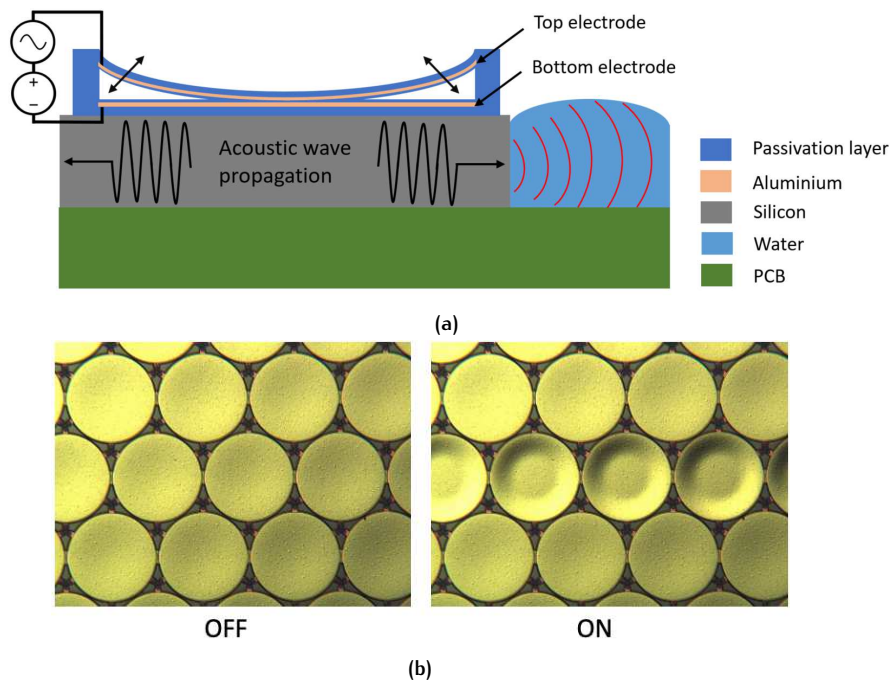


Figure 3.1: (a) A schematic overview of the hypothesized acoustic wave generation in silicon-water as a result of the AC voltage on a CMUT in collapsed state. (b) Several CMUT drums operated in collapse mode.

3.1 EXCITATION OF A SINGLE ELEMENT

The experimental setup included the following components: CMUT chips (CM5 and CM12), a signal generator, a DC voltage source, an RF power amplifier, a transmitting circuit, a fiber optic hydrophone (FP103-322t, Precision Acoustics, UK) with a tip of $10\ \mu\text{m}$ diameter, water, an x-y-z positioning system, and a custom holder for the CMUTs. Each CM5 element contains 33 drums with a diameter of $355\ \mu\text{m}$ and a die thickness of $720\ \mu\text{m}$. Each CM12 element contains 42 drums with a diameter of $120\ \mu\text{m}$ and a die thickness of $675\ \mu\text{m}$. Figure 3.2 depicts an overview of the experimental setup for a CM5, which is similar to the setup for a CM12.

To the side of the die, as shown in Figure 3.2a, water droplets were added. This is the area where the hydrophone was positioned with its tip immersed inside water. The hydrophone was mounted on a translational stage to manipulate it through the water in a controlled manner. The distance between the hydrophone and the sidewall of the silicon was approximately 0.9 mm. For pressure profile measurements the hydrophone was scanned across the cross section of the sidewall. The CMUT was attached to a custom holder and was driven with different waveforms generated by a signal generator and amplified by an RF power amplifier.

LabView was used to control the movement of the positioning system, to trigger the function generator and to record the signal from the hydrophone readout unit. The hydrophone was moved in plane perpendicular to the sidewall of the CMUT.

Finally the recorded voltage signal was converted to pressure by correcting the result with the sensitivity of the hydrophone. This offline analysis was done on MATLAB with a custom made script.

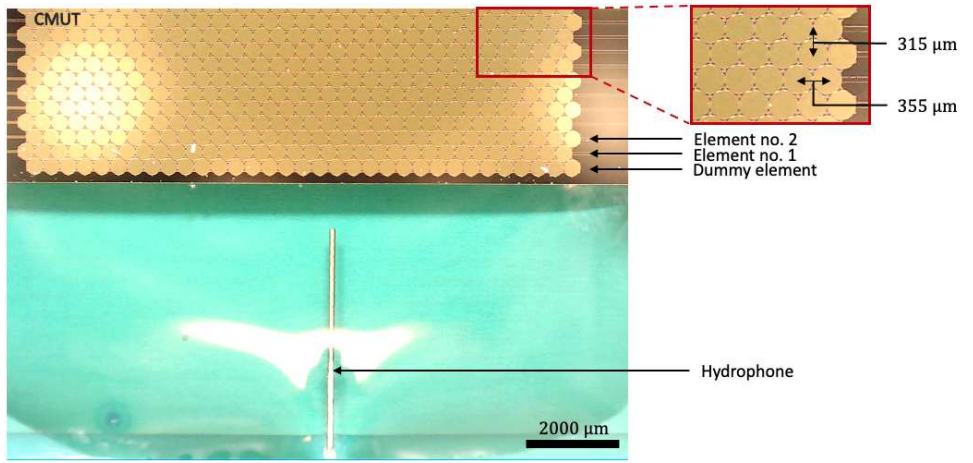
3.1.1 Results

The pressure measurements were performed for one sine wave and compared between different excited CMUT elements. The area closest to the respective excited elements was filled with water.

CM5

The operating conditions for the CMUT with 64 elements were 30 V RF and bias voltages ranging from 120 to 150 V for the CMUT elements 2, 3 and 4 counted from the side facing the hydrophone. To determine the influence of different frequencies on the peak-to-peak pressure, acoustic pressures for one sine wave with frequencies ranging from 1.9 to 4.6 MHz were measured. Figure 3.3 illustrates a transient pressure signal received at the hydrophone when CMUT element 2 was excited at 4.4 MHz. An interesting phenomenon in all the pressure figures is that the hydrophone receives multiple pulses rather than a single sine wave (ringing behavior). This is either due to the underdamped nature of the CMUT membrane vibrating in air or some resonance behaviour of the acoustic signal within the silicon.

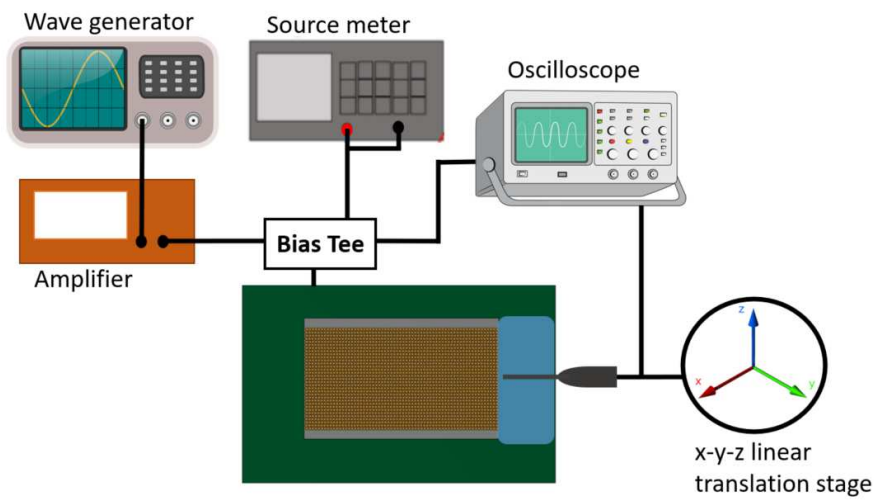
To determine if the pressure output at the sidewall of a CMUT die is homogeneous, a pressure profile experiment was performed. A single element was excited at a frequency of 3 MHz, a bias voltage of 150 V and V_{rf} of 30 V. Figure 3.4 represents the acoustic pressure distribution at the sidewall of a CM5 in the z-y plane. The acoustic pressure ranged from 21.3 to 45.1 kPa, with the maximum pressure measured around the lower area and a small area at the top of the sidewall. The asymmetric pressure field distribution indicates that the CMUT radiation is not equally distributed across the horizontal and vertical axes of the measurement window. This suggests that certain areas have more efficient pressure distribution than others. However, when compared to the Z-axis, the differences on the Y-axis were relatively minor. Regardless of these differences, this experiment demonstrates that the sidewall generates acoustic pressure, which is essential for further experiments.



(a)



(b)



(c)

Figure 3.2: Experimental setup for transmitting and receiving ultrasound based on Tx CMUT chips (CM5) and a hydrophone. (a) Top view of the acoustic pressure measurement. The optical hydrophone was partly immersed in water at the sidewall of the CMUT. The diameter of a single drum and the pitch between two drums are $355 \mu\text{m}$ and $315 \mu\text{m}$, respectively. (b) Pressure measurement setup. (c) Schematic of the experimental setup.

For the following experiments, the hydrophone was therefore aligned to the center of the CMUT die.

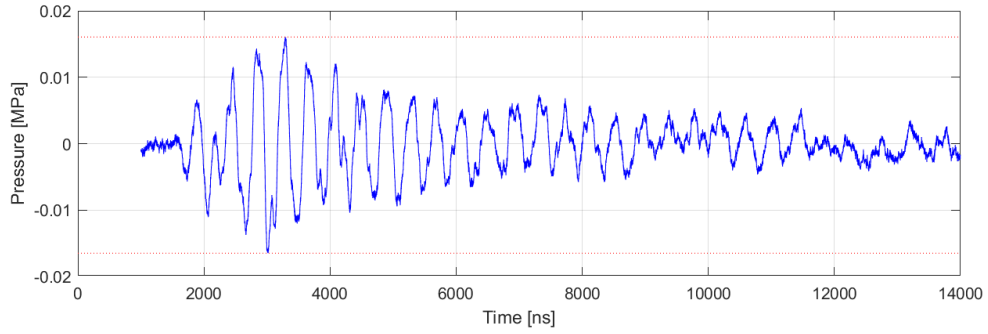


Figure 3.3: The transient output pressure from element 2 with a driving condition of 150 V bias voltage, 4.4 MHz acoustic frequency and 1 pulse of sine wave.

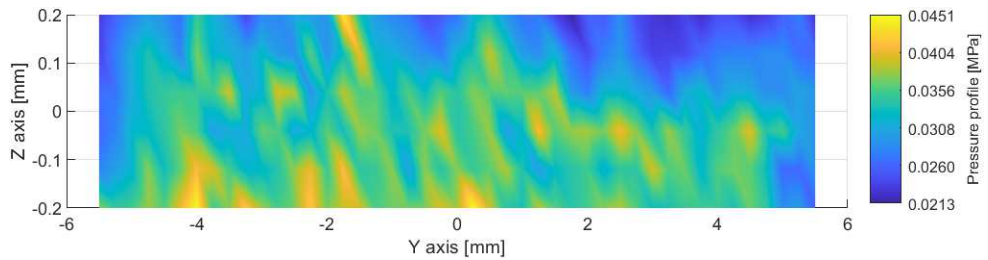


Figure 3.4: Pressure profile of the CM5' sidewall taken from the center point of the die, where the 0.2 mm represents the top and -0.2 mm represents the bottom in the Z-direction. The corresponding parameters are 1 sine wave, frequency of 3 MHz, bias voltage of 150 V and V_{rf} of 30 V.

The peak-to-peak pressures of elements 2, 3, and 4 were measured using two CMUT samples. The result of two CMUT samples were averaged and is plotted in Figure 3.5. In this figure peak-to-peak pressure is shown as a function of frequency for the different CMUT elements. For all figures, the pressure increases as the frequency increases and different bias voltages show an increase in pressure as the frequency increases. The bias voltage values, on the other hand, behave differently depending on the excited element. If we observe element 2 more carefully a pattern can be seen for frequencies lower than 3.6 MHz: the lower the bias voltage, the higher the pressure. When the frequency exceeds 3.6 MHz, the higher the bias voltage, the higher the pressure. This phenomenon compared to elements 3 and 4 is not observed, where an increase in bias voltage generally leads to an increase in the pressure. One possible explanation for the fluctuating pressure behavior of element 2 is that as the transducers get closer to the sidewall, different acoustic behaviors, such as more acoustic modes, come into play. Furthermore, when comparing the pressure profiles for each element, an unusual behavior is observed. The pressure is higher in the elements farther away from the sidewall than in the elements closer to the sidewall. This is in contrast to the expected decay of the acoustic signal over distance due to scattering in the silicon. One possible explanation is that the CMUT closer to the edged had fabrication related damages which could reduce its performance. To summarize, increasing the bias voltage and frequency results in an increase in pressure. An average pressure of 32 kPa is obtained for elements 3 and 4 at a frequency of 4 MHz and a bias voltage of -150 V.

CM12

For the CMUT chip with 96 elements, the operating conditions were 20 V_{rf} and bias driving voltages ranging from -150 to -100 for CMUT elements 96, 94, and 92.

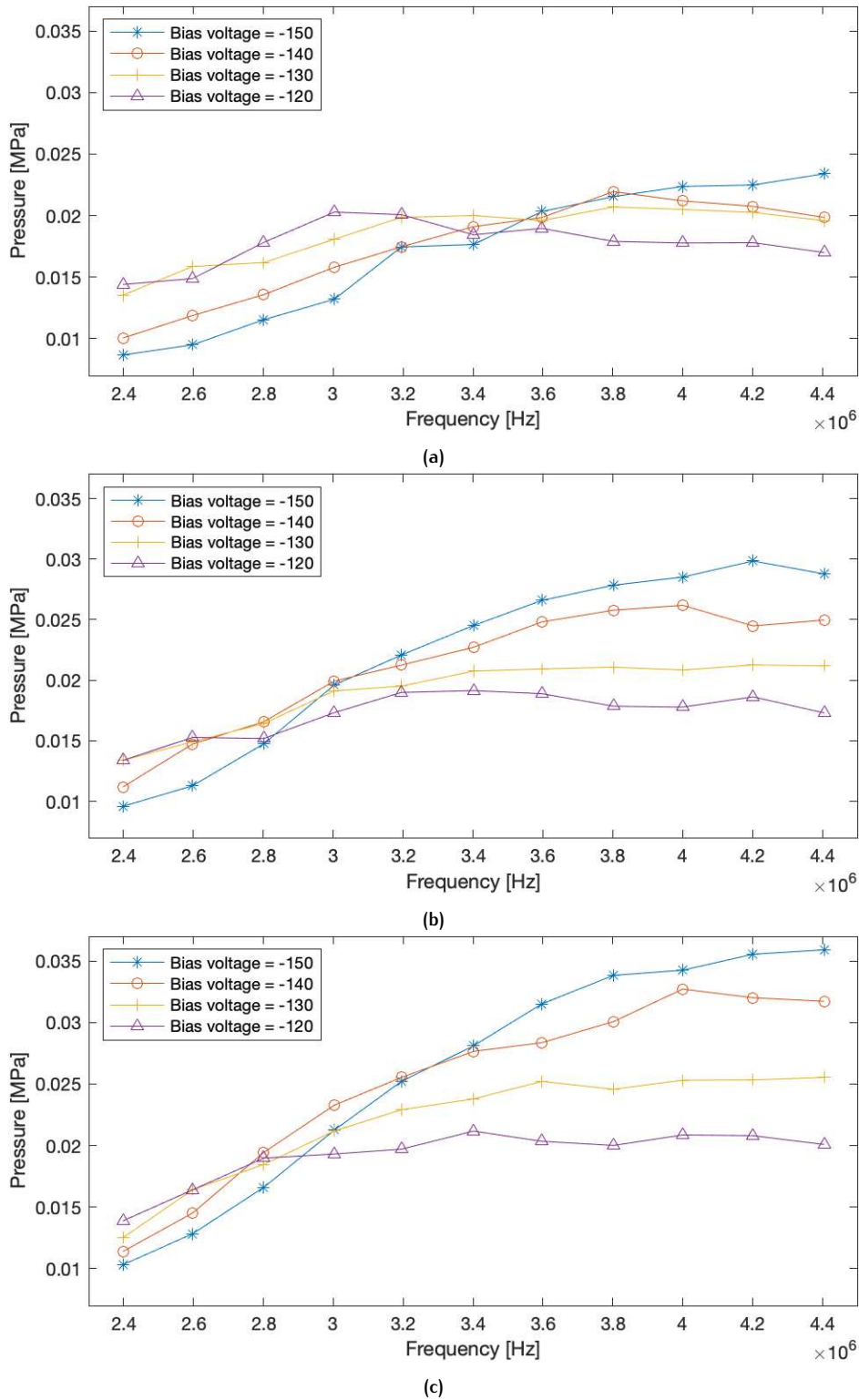


Figure 3.5: Measured acoustic pressure of a single excited CM5 element: (a) Element 2, (b) element 3 and (c) element 4.

To determine the influence of different frequencies on the peak-to-peak pressure, acoustic pressures were measured for one sine-wave with frequencies ranging from 7 to 15 MHz. Appendix B.1 shows the peak-to-peak pressures for various excited CMUT elements in relation to frequencies and bias voltages. One of the figures is shown in Figure 3.6, which represents element 94. Figures B.1c, B.1b and B.1a show a similar pressure behavior, with bias voltages of -150 and -140 V producing the

highest pressure profiles when compared to other bias voltages. The maximum pressure was measured around 23 kPa. Figure B.1a, on the other hand, depicts a slightly different pressure pattern as a function of frequency.

For elements 92 and 94, the pressure values for bias voltages ranging from -150 to -130 V increase gradually, whereas all bias voltages for element 96 show a rapid increase at first and then a gradual decrease. Furthermore, for bias voltages ranging from -120 to -100 V, the pressure patterns for element 92 are nearly constant, whereas element 94 shows a gradual decrease. The element closest to the hydrophone, element 96, produces the overall highest-pressure profile.

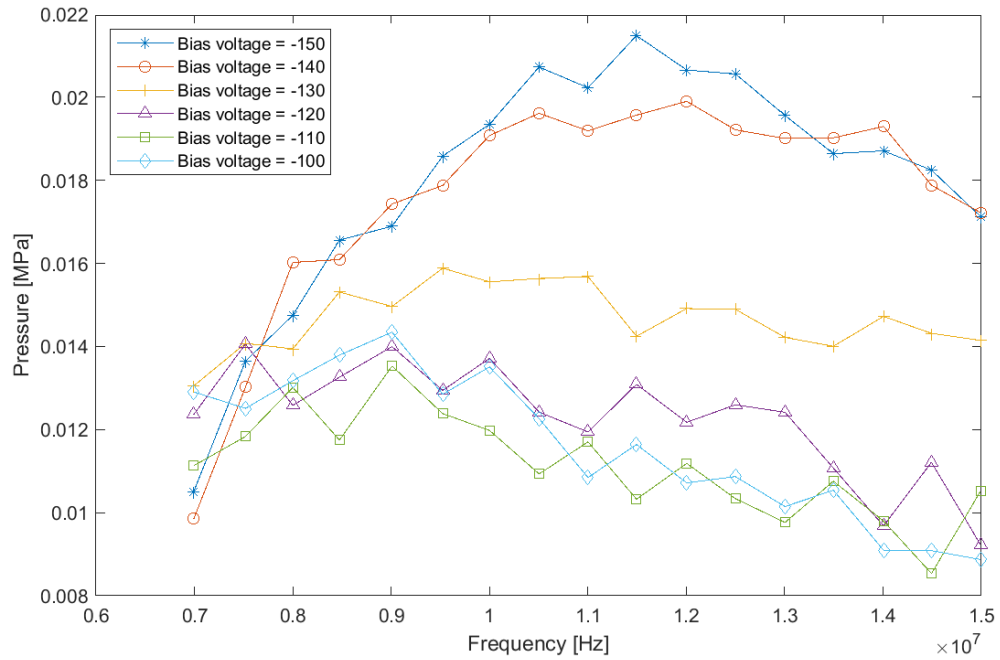


Figure 3.6: Measured acoustic pressure of a single excited CM12 element: element 94.

3.2 EXCITATION OF MULTIPLE ELEMENTS

CMUTs, as illustrated in Figure 3.2, have multiple elements that allow for the excitation of different elements at the same time or with a phase delay. This gives the possibility of using a phase delay approach to amplify the acoustic pressure. The main objective of this experiment is therefore to investigate the acoustic pressure amplification and how this pressure can be maximized, which plays a significant role in acoustic propagation. For this experiment, the focus will lie on the CM5 CMUT transducers. The experimental setup for multiple element excitation of a CM5 is similar to that for single element excitation (Fig. 3.2c). However, in this case, the signal generator and RF power amplifier were replaced with a WUP board and its software (Fig. 3.7). A WUP is an in-house-built ultrasound driver system based on the HV7351 pulser chip (Microchip Technology, USA). This enables 32 element excitation, and the trigger can be provided either internally or externally. Furthermore, it allows the use of phase delay approach, in which each element is excited with an increasing time delay of Δt .

With the proper time delay, the acoustic wave generated from each element that propagates through the silicon will add in phase. This allows for phase alignment, which leads to amplification of acoustic waves and thus more acoustic energy that

can propagate and couple into water. The condition for phase alignment is given by

$$\Delta t = \frac{\text{pitch}}{v_{\text{medium}}}, \quad (3.1)$$

where Δt is the time delay with a minimum value of 5 ns, v_{medium} is the sound velocity in the medium and the pitch is the distance between one element to the next.

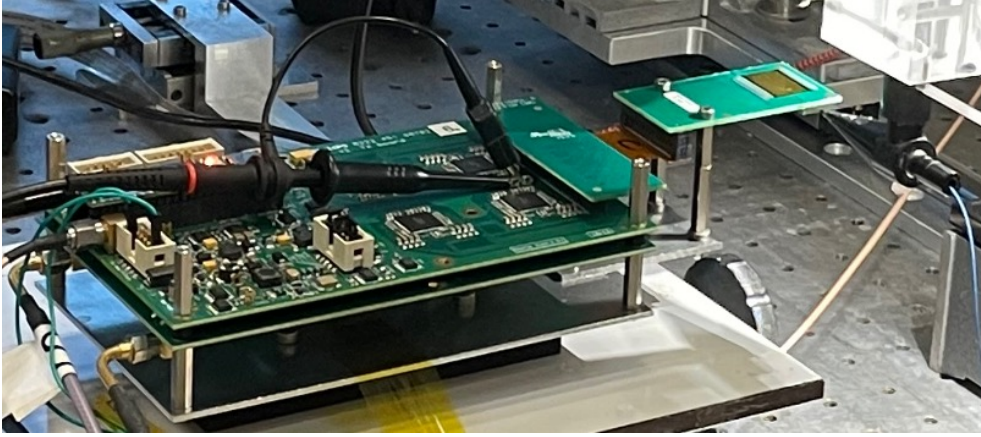


Figure 3.7: Experimental setup for multiple element excitation, where a CM5 is mounted on a WUP board.

For the implementation of a phase delay approach, two methods were investigated:

- Phase delay based on time delay, Δt ;
- Phase delay based on velocity, v_{medium} .

For a phase delay approach based on the time delay, the minimum amount of time delay of 5 ns is taken that linearly increases per element. With an increasing time delay, the elements are excited from element 32 to element 1. Figure 3.8 shows this phase delay technique applied to a CMUT. In this case, velocities for lower time delays show an increased step size compared to higher time delays. For a phase delay approach based on velocity, a constant step size was taken.

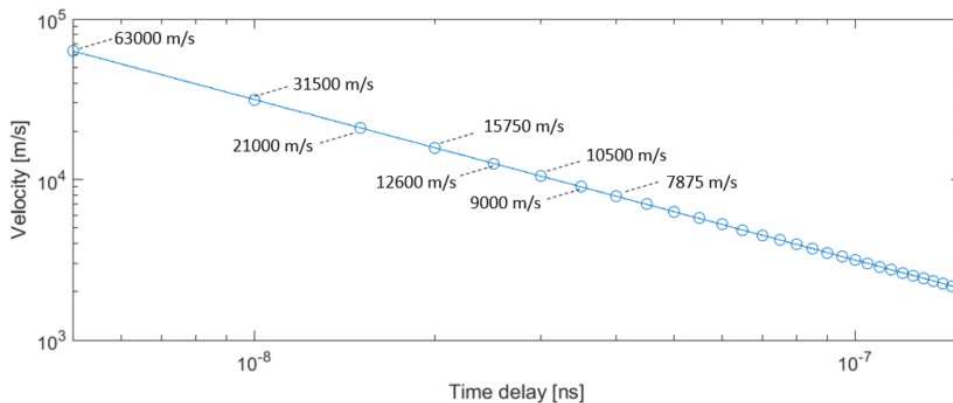


Figure 3.8: The relationship between the acoustic velocity and the time delay between each elements.

When applying a phase delay technique on a CMUT, it is hypothesized that the highest acoustic pressure can be produced if the time delay matches the sound

velocity in silicon. To determine the phase delay with the highest pressure in silicon, different Δt and v_{medium} were applied on 32 elements (Fig. 3.9) until maximum pressure was obtained.

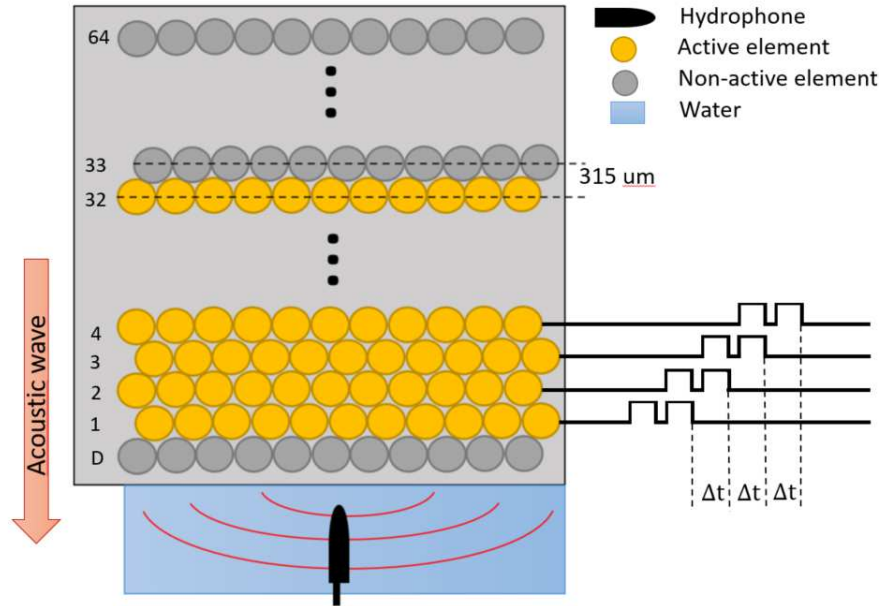


Figure 3.9: Schematic overview of multiple elements excitation with a beam steering technique.

3.2.1 Results

To understand the behavior of the acoustic pressure as a function of the distance from the sidewall in silicon, eight elements were excited simultaneously with an interval of $315 \mu\text{m}$. Elements 1 to 32 was taken into account. A linear decay in the pressure output is visible in Figure 3.10. A slope of $-1.66 \cdot 10^{-5} \text{ MPa}/\mu\text{m}$ is present for the excitation of element 9 and higher. This indicates that attenuation exists in silicon. Attenuation can be caused by a variety of mechanisms, including material inhomogeneity, which can cause scattering loss, and thermal lattice vibration, which can cause coherent wave scattering loss [34].

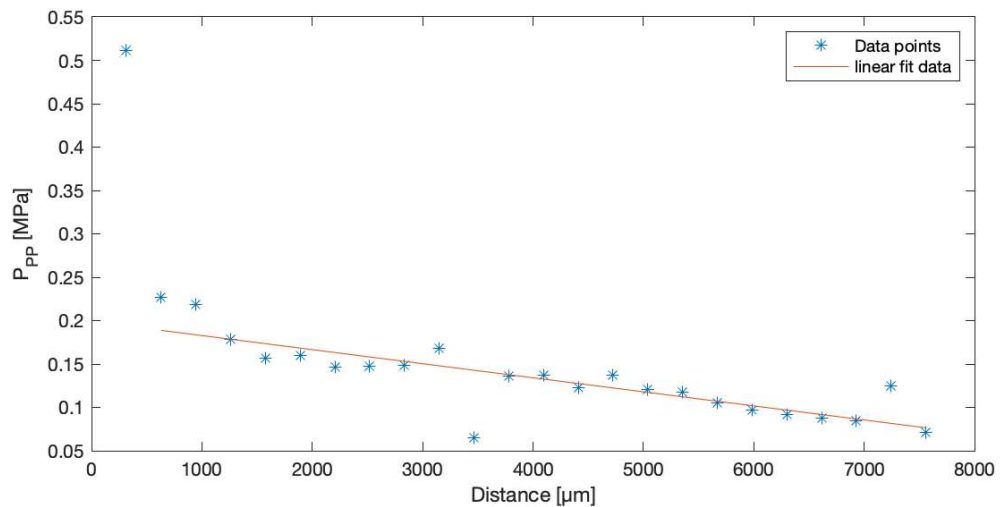


Figure 3.10: Attenuation profile in silicon.

The operating conditions for the phase delay approach based on time delay were a unipolar square wave with 15 V amplitude, a bias voltage of 150 V, 15 cycles, and a pulse repetition frequency (PRF) of 1 kHz. A frequency sweep from 2 to 5 MHz shows that the optimum frequency for producing the maximum pressure is at 4.5 MHz. This can be explained due to the CM5 resonance at 3.7 and 4.5 MHz. The acoustic pressure was measured for a time delay ranging from 5 ns to 140 ns. Figure 3.11 shows the peak-to-peak pressure for each element as a function of time delay. Acoustic pressure effectively aligns where pressure peaks are present at time delays of 40 ns and 65 ns. Based on equation (3.1), this corresponds to a velocity of 7875 and 4846 m/s within silicon, respectively. Thus, various acoustic modes contribute to the generation of large amounts of acoustic pressure. Furthermore, the maximum pressure of 0.9 MPa was generated near the velocity of 7875 m/s.

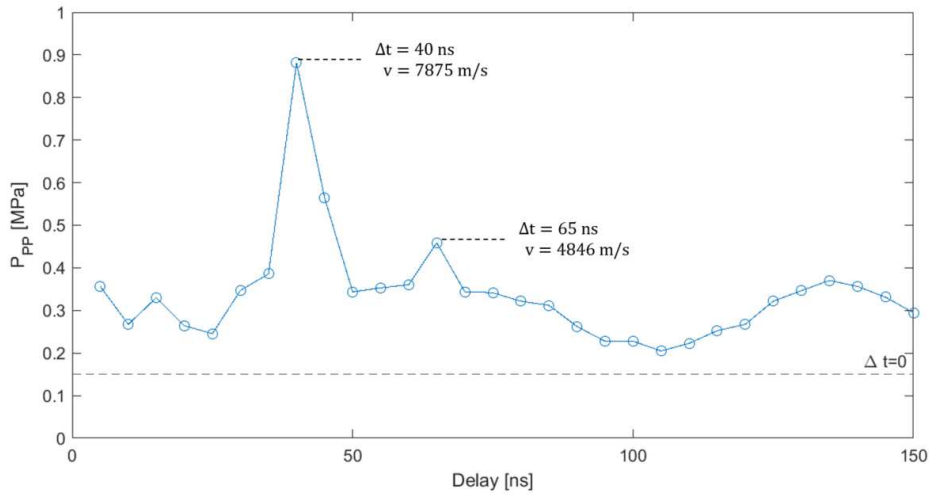


Figure 3.11: Peak-to-peak pressure with respect to the time delay. The dotted line represents the pressure measured when no beam steering was applied ($\Delta t = 0$ ns).

The operating conditions for the phase delay approach based on velocity were similar to the time delay method. However, cycle rates of 2 and 15 were applied to investigate the effect of cycle rate on the behavior of the pressure output in phase delay. Figure 3.12 shows the peak-to-peak pressure for each element as a function of velocity. In both figures, two velocities with a significant increase in pressure are present, namely a mean velocity of 6750 m/s and 8190 m/s. This suggests that the increase in cycle rate does not affect a certain velocity range. However, for 15 cycles a prominent third peak is present for a velocity of 9000 m/s. This indicates that the combination of an increase in cycle rate at a certain velocity, leads to an amplification of acoustic pressure. The maximum pressure for each cycles was measured around the mean velocity of 6750 m/s: 0.235 MPa for 2 cycles and 0.73 MPa for 15 cycles.

Both phase delay approaches show a clear increase in pressure if a certain time delay/velocity was chosen. The time delay approach suggest that a significant increase of pressure is present around 7875 m/s. However, this method is not that accurate in regards to the velocities around this value due to its limited step size. The velocity approach implements a certain velocity step size that can cover this limitation. As seen in the result for the velocity approach, clear increase of pressures are present for two different velocities with an interval of 6000 m/s to 9000 m/s. While, the time delay approach shows one velocity.

According to Song *et al.*, the velocities in $\langle 110 \rangle$ -direction single-crystalline silicon wafer correspond to a longitudinal velocity of 9138 m/s and a transversal velocity of 4675 m/s [35]. As seen in figure 3.11, the pressure peak at a velocity of 4846 m/s is close to the transversal velocity. Furthermore, current results suggest that additional velocities play a significant role in acoustic wave propagation. This

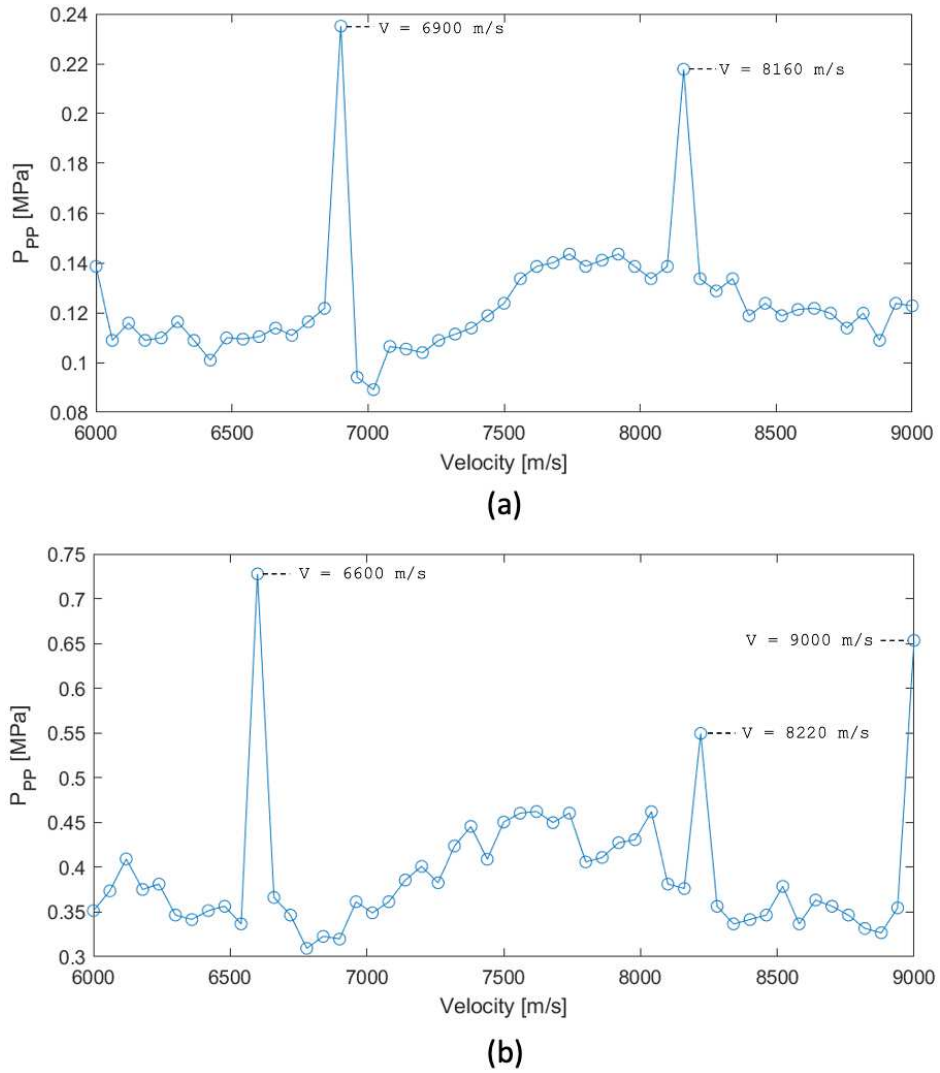


Figure 3.12: Peak-to-peak pressure with respect to the velocity: (a) 2 cycles and (b) 15 cycles.

indicates that different acoustic modes should be taken into account. Moreover, the output pressure of the hydrophone was relatively insensitive to the location of the hydrophone. This suggests that the acoustic signal is propagated from the entire sidewall, which indicates a BAW-based sorting device. The phase delay approach showed a significant pressure increase compared to a single element excitation of almost up to 1 MPa.

3.3 PARTICLE ALIGNMENT

The performance of a CMUT-based sorting device using ultrasound waves emitted from the sidewall of the device was evaluated by applying polystyrene particles with a $10 \mu\text{m}$ diameter diluted in deionized (DI) water at the sidewall of the CMUT. A CM5 was used as an acoustic source due to its size and ease of operation. The device was excited at a frequency of 4.5 MHz, based on the CM5 result mentioned in the previous section.

A similar setup as in Figure 3.2 with phase alignment was utilized. However, instead of plain DI water and a hydrophone, droplets of $10 \mu\text{m}$ latex particles (BCR-167) diluted in DI water were applied at the sidewall of a CM5. Figure 3.13 gives an overview of the experimental setup for the investigation of particle alignment at

the sidewall of a CM5. The device is made up of a CM5 chip and a silicon piece next to the die. By gluing a piece of glass to the PCB, which serves as the reflector, an open channel is formed. Standing waves will form between the silicon die and the reflector.

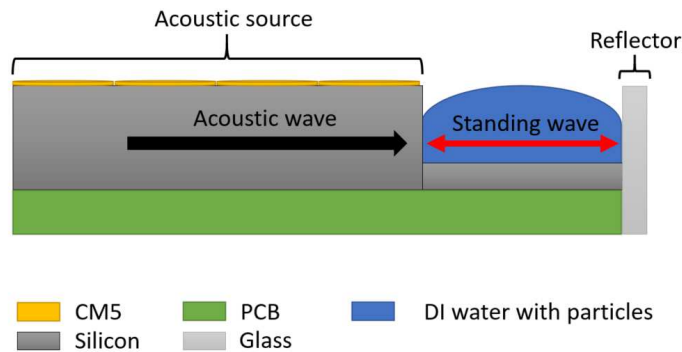


Figure 3.13: Schematic overview of a BAW-based particle alignment setup.

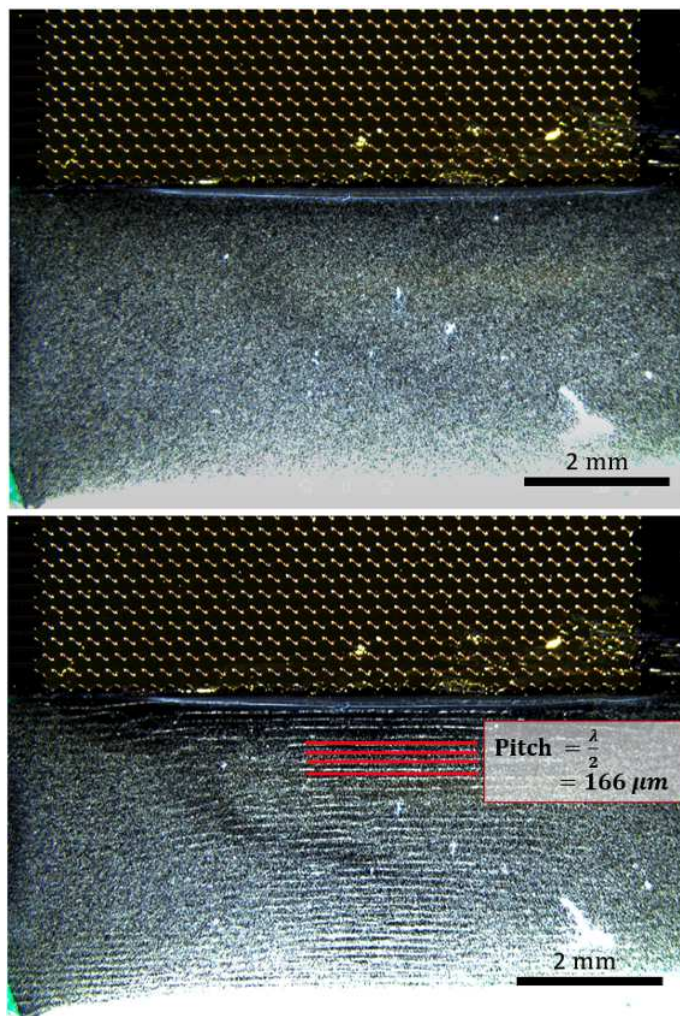


Figure 3.14: Sorting performance of BAW particle alignment between the sidewall of a CM5 and a reflector using a large amount of $10\ \mu\text{m}$ diameter polystyrene particles. The top image shows the situation when the transducers were off with no particle alignment. The bottom image was when the transducers were on and particle aligned was visible. This alignment corresponds to half a wavelength in less than 5 seconds.

The transducer was subjected to $15 V_{rf}$, $-150 V_{bias}$, and a frequency of 4.5 MHz during the experiment. 15 Cycles at a repetition rate of 5 kHz and a time delay of 40 ns between each element was considered. Particle alignment is definitely possible in just a few seconds, as shown in Figure 3.14, even with a low duty cycle of 1.7%. Multiple stripes of particles are visible with a pitch between each node corresponding to half the wavelength for the frequency of 4.5 MHz ($\frac{1}{2}\lambda = \frac{1}{2} \frac{1500}{4.5 \cdot 10^6} = 167 \mu\text{m}$).

Another experiment was performed to evaluate if particles could align in a channel width of $375 \mu\text{m}$, as shown in Figure 3.15. The given width of the microchannel corresponds to a frequency of 2 MHz for half the wavelength ($f = 2 \cdot \frac{1500}{375 \cdot 10^{-6}} = 375 \mu\text{m}$). A single element closest to the sidewall was excited at $140 V_{bias}$, $40 V_{pp}$, and 10 cycles in $25 \mu\text{s}$. The system was driven at the frequency that should result in the best particle alignment. While sweeping the frequency, particle alignment at a frequency of 2.3 MHz was clearly visible (Fig. 3.15b). When the transducers were turned off, unfocusing of the particles was seen. The difference between the expected frequency and the actual frequency can be explained by the channel's assembly.

Both experiments show that particle alignment with a CMUT is possible. As a result, the proof-of-concept, a CMUT-based cell sorting device, has been strengthened.

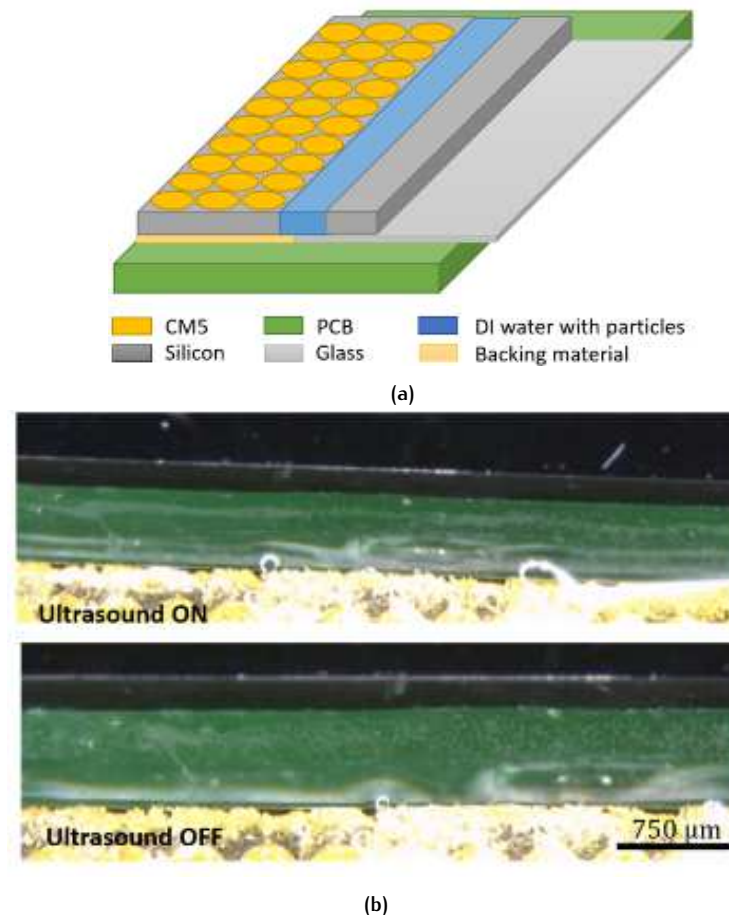


Figure 3.15: (a) Schematic overview of the device with a $375 \mu\text{m}$ microchannel at the sidewall of a CM5. (b) The top image shows a clear alignment of $10 \mu\text{m}$ polystyrene particles flowing through an open microchannel at a low speed, while the bottom image illustrates the situation after the transducers are turned off and unfocused particles are seen.

4

DESIGN AND SIMULATION

The first section of this chapter discusses the structures and designs used for the microfluidic devices. To understand the underlying mechanism of the acoustic field in BAW-based microfluidic sorting devices, modeling of the transducer and the microfluidic components is necessary. The following section investigates the acoustofluidic influence in the microfluidic device. This involves coupling of different physics, where the software program COMSOL 5.6 gives the possibility to simulate different geometries for multiple physics, including acoustic, solid mechanics and fluid physics.

4.1 DESIGN OF THE MICROFLUIDIC DEVICES

Due to the limited amount of time, the integration of the CMUTs on top of the microfluidic devices was not possible. Therefore, two different acoustic-microfluidic device interfaces will be considered. The transducers will be externally connected either to the sidewall or the bottom of the device, which is explained in the next chapter. Figure 4.1 and Table 4.1 give an overview of the design and structures used for the two different microfluidic devices based on the wavelengths of the CM5 and CM12 CMUT devices.

The microfluidic devices have a dimension of $19.25 \times 9.15 \text{ mm}^2$, which should contain a microchannel, in- and outlet ports (I/O ports), and several vacuum gap structures. The width of 19.25 mm for the microfluidic device is chosen such that if the membrane of the microchannel breaks during the processing, a glass plate with the I/O ports can be glued on top of the device. The I/O ports of the device are therefore fixed with a diameter of $400 \mu\text{m}$, corresponding to the diameter of the I/O ports of the glass plate. The length of the device is determined by the area available on the mask used for fabrication. The width of the main channel is dependent on the relevant wavelengths of the CM5 and CM12 devices used in the experiments.

The channel width of the CM5-based device only uses one size, namely $375 \mu\text{m}$, which corresponds to the wavelength (λ) of $\lambda/2$ and 1λ for 2 and 4 MHz, respectively. This in contrast to the CM12-based device, where two different widths are used for the frequency of 8 MHz: $187.5 \mu\text{m}$ for $\lambda/2$ and $93.85 \mu\text{m}$ for 1λ . Along the microchannel, three different vacuum structures are designed to amplify or propagate and couple the acoustic wave more efficiently into the silicon and the microfluidic channel. Here it is assumed that a horn structure can amplify the acoustic wave.

4.2 VELOCITY PROFILE IN THE MICROCHANNEL

In most microfluidic flows, the Reynolds number is small due to the small dimensions resulting in a laminar flow. The Reynolds number is given as

$$Re = \frac{\rho v D_h}{\mu} = \frac{v L}{\eta}, \quad (4.1)$$

where ρ , v , μ and, η are the density, velocity, and the dynamic and kinematic viscosity of the medium, respectively. D_h is the hydraulic diameter of the microchannel.

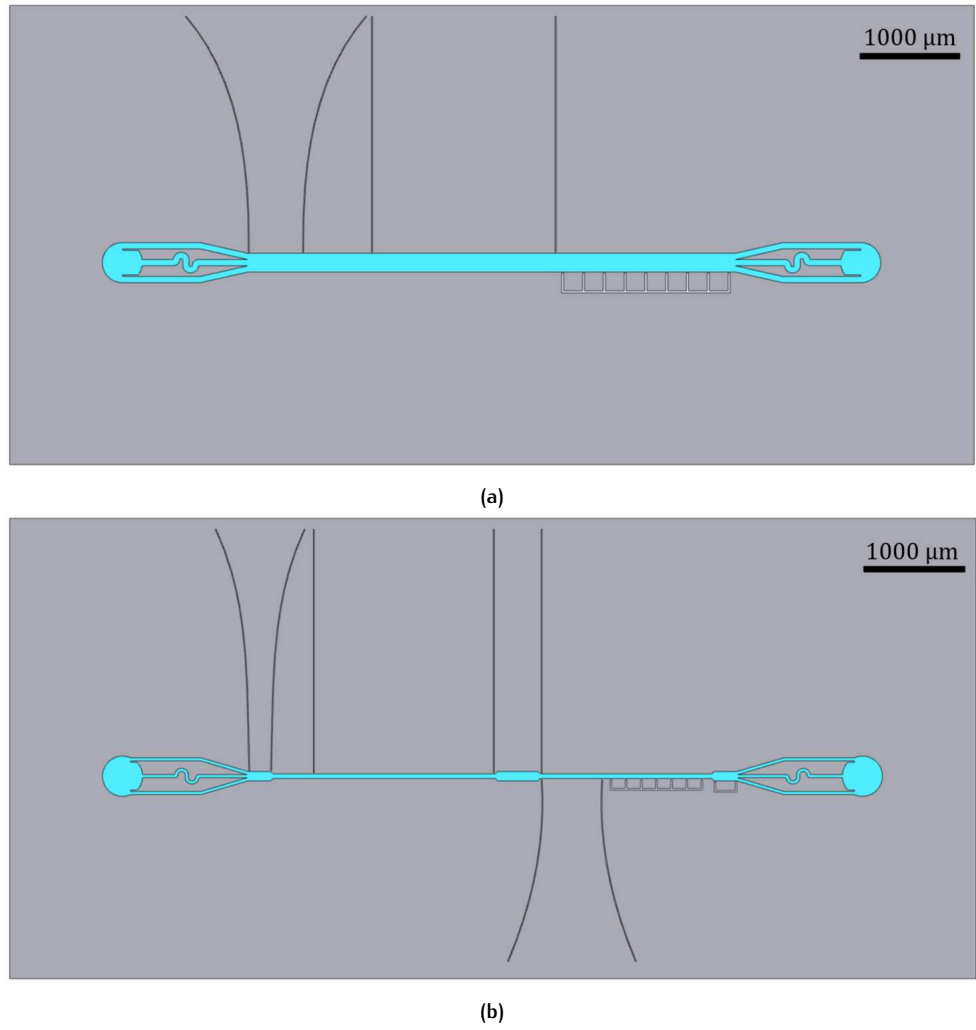


Figure 4.1: Microfluidic designs for (a) CM5-based microchannels and (b) CM12-based microchannels.

In a rectangular microchannel, D_h is also given as $D_h = \frac{2ab}{a+b}$, where a and b are the width and the height of the microchannel, respectively. Table 4.1 gives the overview of the width, height, and Reynolds number for each design. The Reynolds numbers for both designs indicate that a laminar flow pattern can be assumed. The velocity field in a fluid flow is described with the Navier-Stokes equation (external forces are neglected), given by

$$\rho \left(\frac{\delta \mathbf{u}}{\delta t} \right) = -\rho (\mathbf{u} \cdot \nabla) \mathbf{u} - \eta \nabla^2 \mathbf{u} - \nabla P, \quad (4.2)$$

where ρ , \mathbf{u} and η are the density, velocity, and dynamic viscosity of the medium and P is the pressure field. The fluid flow is assumed to be steady, viscous, and incompressible, also known as a Poiseuille flow. Therefore, equation 4.2 reduces to

$$\nabla P = \eta \nabla^2 \mathbf{u}, \quad (4.3)$$

By solving this equation, the mean linear velocity can be determined, which can be re-written as the Hagen-Poiseuille equation. This equation is equivalent to Ohm's Law, where the volumetric flow rate (\mathbf{Q}) is related to the pressure drop (P):

$$\Delta P = \frac{dP}{dx} = R_h \mathbf{Q}, \quad (4.4)$$

where $\frac{dP}{dx}$ is the pressure gradient and R_h is the hydraulic resistance. R_h depends on the geometry of the microchannel and the dynamic viscosity of the medium, where

	Microfluidic device based on CM ₅	Microfluidic device based on CM ₁₂
Microchannel		
Diameter of the I/O ports	400 μm	400 μm
Height	40 μm	40 μm
In- and outlets width	125 μm	62.5 μm
Main channel width	375 μm corresponding to $\frac{1}{2}$ and 1λ , resp. for 2 and 4 MHz	187.5 and 93.75 μm corresponding to $\frac{1}{2}$ and 1λ for 8 MHz, resp.
Reynolds number	0.081	0.074 and 0.063 for 187.5 μm and 93.75 μm , resp.
Vacuum structure		
Ratio horn structure	3.4	4.2 and 2.1 resp, at channel width area of 187.5 and 93.75 μm
Size trenches	355 x 375 μm^2	167 x 272 μm^2 167 x 390 μm^2
Width straight wall	17 μm	17 μm

Table 4.1: Overview of the structures used in the microfluidic device with parameters for each microchannel with $\rho_{water} = 997 \text{kg/m}^3$, $v = 1 \text{mm/s}$ and $\mu = 0.89 \text{mPa} \cdot \text{s}$.

the R_h of a rectangular cross-section depends on the width and the height of the microchannel:

$$R_1 \approx \frac{12\eta L}{wh^3 - 0.63h^4} \quad \text{for} \quad w > h, \quad (4.5)$$

$$R_2 \approx \frac{12\eta L}{hw^3 - 0.63w^4} \quad \text{for} \quad h > w, \quad (4.6)$$

where h , L and w are the height, length, and the width of the microchannel. From these equations, it is clear that the length of the in- and outlets influences the volumetric flow rate.

The ports at both ends of the microchannel act as the I/O ports, where the velocity profile of the three outlets needs to be considered. Since only one port is used at each side, an equal flow distribution over the in- and outlets is preferred for further analysis with an acoustic field. It is therefore important to analyse the behavior of the fluid flow in the microchannel. A fluid flow simulation is made for two different scenarios:

1. Three straight I/O channels at both sides
2. Three I/O channels with two straight channels and a sine channel at both sides.

4.2.1 Model

In order to obtain a quantitative indication of the flow behavior in the different microchannels with a rectangular cross-section, stationary 3D numerical models were developed using the Multiphysics software COMSOL 5.6. The Navier-Stokes equations for incompressible fluids and the continuity equation were used to model the fluid flow, given as

$$\rho(\mathbf{u} \cdot \nabla)\mathbf{u} = \nabla \cdot [-p\mathbf{I} + \mathbf{K}] + \mathbf{F}, \quad (4.7)$$

$$\rho \nabla \cdot \mathbf{u} = 0, \quad (4.8)$$

where \mathbf{u} is the velocity vector, p is pressure, I is the identity matrix, \mathbf{K} is the viscous force and \mathbf{F} is the volume force vector. Each microchannel included a main channel and three in- and outlets at both sides. The boundary conditions were a velocity inflow of 1 mm/s, no-slip at the wall and a pressure outlet of zero Pa.

4.2.2 Results

Several numerical simulations have been conducted and the results are presented to show the effect of the two scenarios on the fluid flow characteristics. The developing process of the velocity magnitudes for a CM5-based microchannel with $z=20 \mu\text{m}$ and scenarios 1 and 2 are depicted in Figure 4.2. The velocity increase can be observed in the in- and outlets of each scenario. It is particularly visible that the outlet velocity maximum in scenario 1 is present in the middle outlet. This in contrast to scenario 2, where the outlet velocity maxima are equally divided over the three outlets. A more precise velocity profile at the intersection of the three outlets for each scenario is given in Figure 4.3, where a 3D flow profile is presented. The CM12-based microchannel exhibits the same phenomena (Fig. C.1 and C.2). This can be explained from the difference in length of the outlets for both scenarios. It is clearly visible that an identical length for each outlet plays a significant role in the equal distribution of the velocity profile around these areas. Therefore, scenario 2 is considered for further investigation.

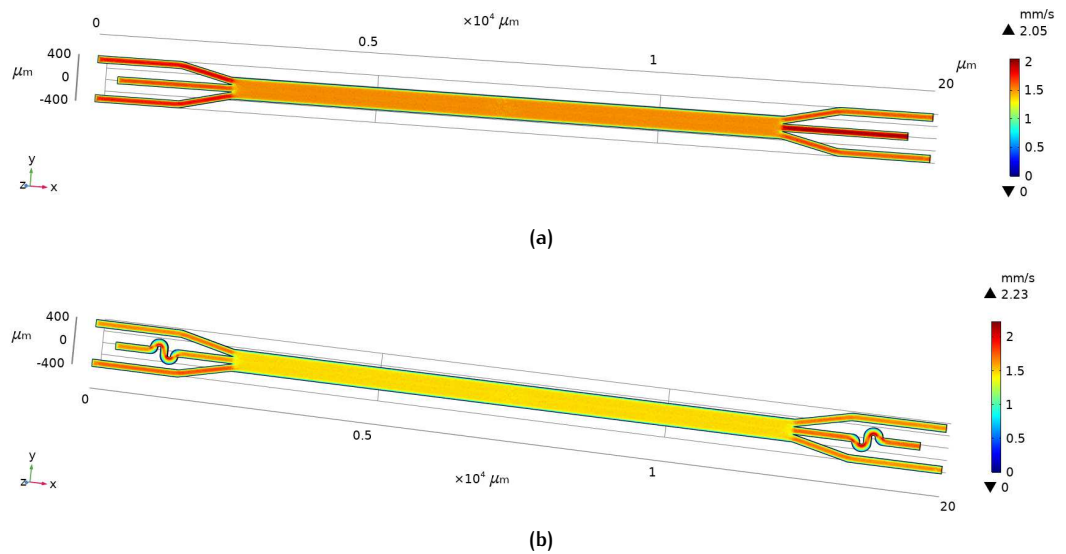


Figure 4.2: Simulated cross sectional velocity profile of the fluid flow in the CM5-based microchannel at $z=20 \mu\text{m}$ and inlet velocity of 1 mm/s: (a) scenario 1 and (b) scenario 2.

4.3 SIMULATIONS OF ACOUSTIC PARTICLE TRACING

To investigate if the sidewall pressures given in the previous chapter creates enough pressure in the microchannel to align particles, modeling of the acoustofluidic behavior of particles in the microchannel is necessary. The software program COMSOL 5.6 gives the possibility to simulate different geometries for acoustic, fluid and particle physics.

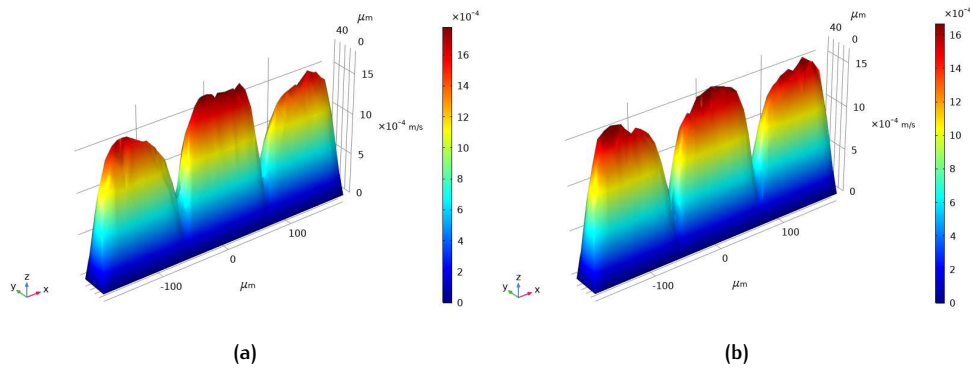


Figure 4.3: 3D flow profile taken at the intersection of the three outlets in a rectangular microchannel under condition of an inlet velocity of 1 mm/s: (a) scenario 1 and (b) scenario 2.

4.3.1 Model

A silicon chip containing a microchannel filled with a solution of particles was considered. The acoustic cavity is formed by the acoustic hard silicon walls and the acoustic soft water inside the microchannel. This indicates that the geometry and materials of the microchannel determines its acoustic resonances for specific frequencies. Therefore, an acoustic boundary area and hard walls are considered for this simulation.

Based on the concept of the previously mentioned BAW microfluidic device, geometric models illustrated in Figure 4.4 were established, consisting of a single inlet and three outlets. For the CM12-based microchannel, the length of the first and second main channel are $2000 \mu\text{m}$ and $450 \mu\text{m}$, respectively. The width of the microchannel is based on the resonance frequency of 8 MHz with the focus on one and two pressure nodes. This corresponds to a width of $93.75 \mu\text{m}$ and $187.5 \mu\text{m}$ (Fig. 4.4a). For a CM5-based microchannel, the length of the main channel is $4000 \mu\text{m}$ with three outlets (Fig. 4.4b).

A laminar flow, pressure acoustic and particle tracing physics were applied to investigate particle behavior under an acoustofluidic field. An average velocity flow of 1 mm/s with a fully developed flow condition was applied at the inlet. The acoustic source is shown in Figure 4.4 and the influence of pressure and velocity variation was investigated. The initial velocity of the particles corresponds to the inlet flow, where three particles are released at a random location and at a specific interval. The acoustic radiation force and the drag force acting on the particles in solution are calculated once the pressure and the flow rates are known. Figure 4.5 illustrates the numerical simulation steps necessary to calculate the particle trajectory. The relevant parameters are the density, speed of sound, and the compressibility (Table 4.2).

Materials	Density [kg/m^3]	Speed of sound [m/s]	Compressibility [Pa^{-1}]
Water	998	1500	$6.77 \cdot 10^{-7}$
Polystyrene particle	1055	2400 (Pressure-wave)	$2.37 \cdot 10^{-10}$
		1150 (shear-wave)	

Table 4.2: Material properties used to model top-view of microfluidic device.

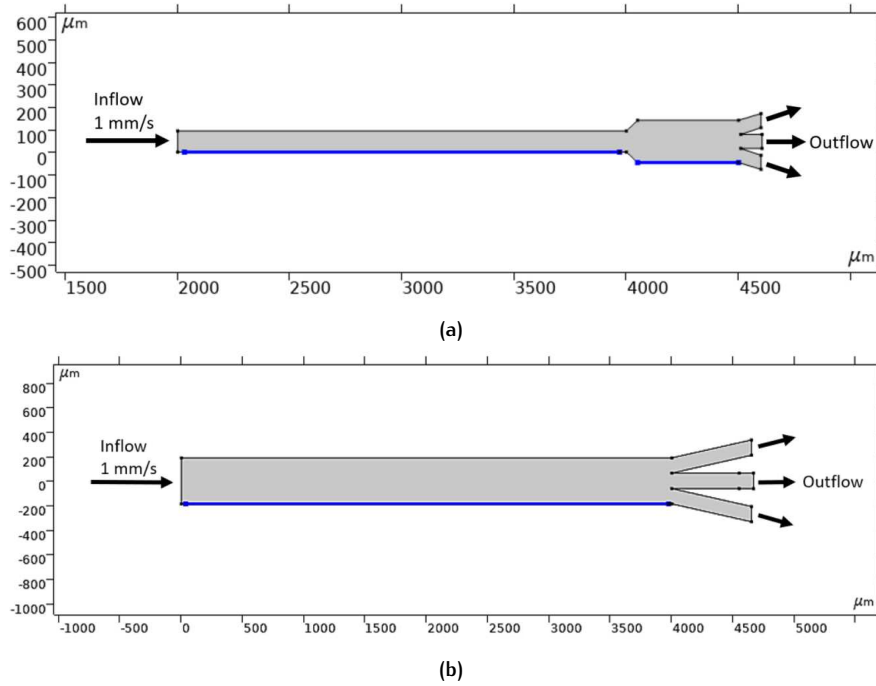


Figure 4.4: The acoustic boundary sources are shown as the blue selected walls for (a) CM12-based microchannel and (b) CM5-based microchannel.

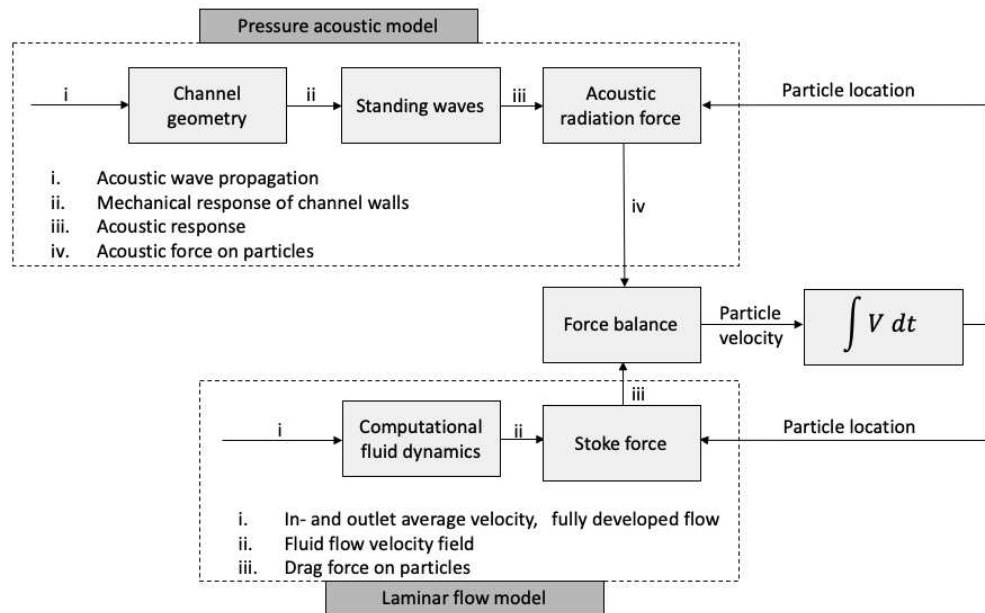


Figure 4.5: Numerical simulation steps necessary for particle simulation.

4.3.2 Results

It is important to find the relevant conditions between the dominant parameters that affect the particle trajectory such that the particles sort efficiently. To evaluate the performance of the acoustophoresis process, the performance of the previously mentioned designs was assessed in a 2D model. Particles of 10 μm diameter are released from the inlet side with a random distribution along the cross section of the inlet. The particles are released with an interval time of 0.5 seconds for a CM12-based and CM5-based microchannel at 0.1 seconds for 16 seconds. The sorting efficiency was determined for a simulation time of 20 seconds.

Figures 4.6a and C.3a show the velocity distribution of the fluid flow along the length of the microchannel. The low Reynolds number indicates that the flow is laminar and a parabolic pattern of the fluid flow along the width is present. Figures 4.6c and C.3b illustrate the acoustic pressure distribution inside the microchannel for the CM5-based and CM12-based devices, respectively. The acoustic pressure is generated at the wall of the channel next to the CMUT with at the opposite side the reflector that allows for the formation of standing waves. The inlet- and outlet ports act as open boundaries for outgoing waves. The frequencies were chosen such that one node and/or two nodes are formed in the microchannels. This allows for a suitable particle separation with regards to the microchannel design. Acoustic pressures of 60 kPa and 80 kPa are applied for the CM12-based and CM5-based designs, respectively.

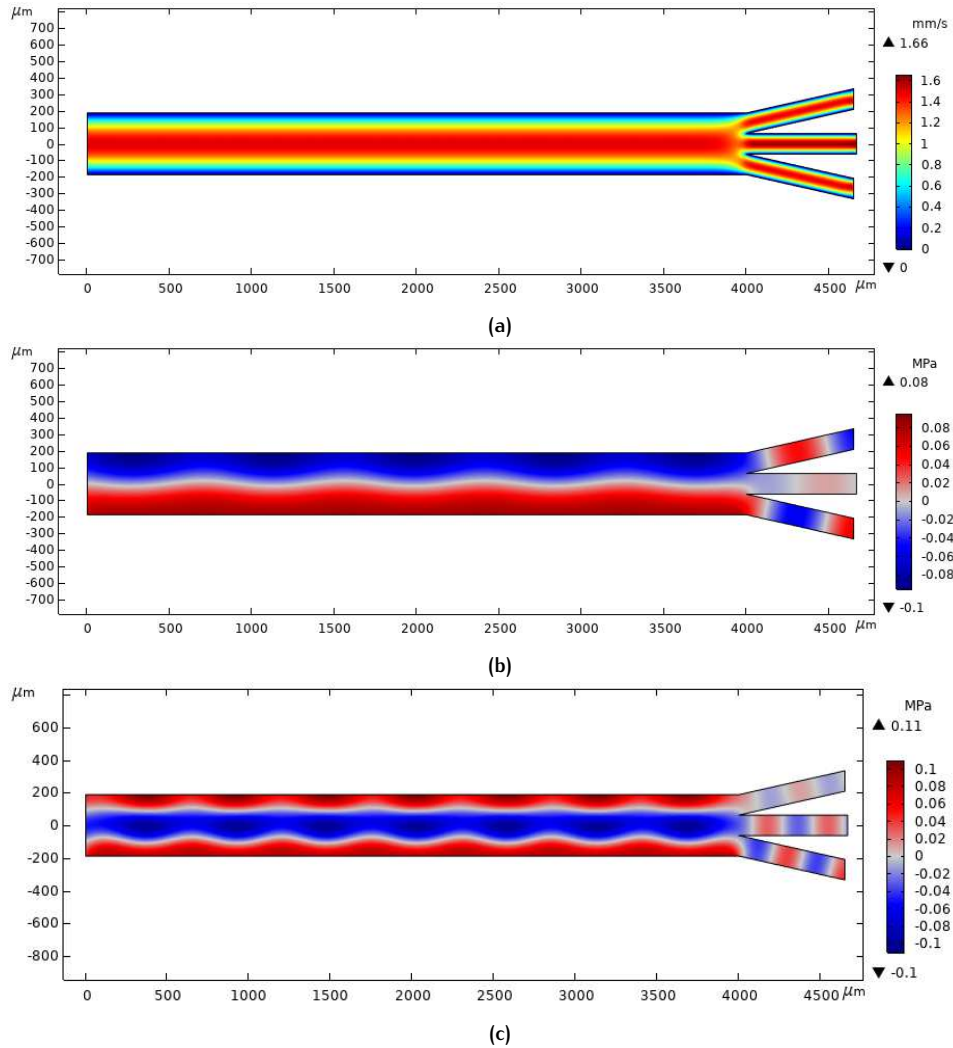


Figure 4.6: CM5-based microchannel design. (a) Velocity distribution of the fluid flow along the streamlines inside the microchannel. Wave plots (red positive, blue negative) of the acoustic pressure field at resonance in a water-filled microchannel with a pressure of 80 kPa and a frequency of (b) 2 MHz (c) 4 MHz.

The influences of pressure, frequency and velocity are given in Table 4.3. For a CM5-based device, minimum pressures of 60 kPa and 80 kPa are required for a sorting efficiency of 100 % for a velocity of 1 mm/s and frequencies of 4 MHz and 2 MHz, respectively. This indicates that for lower frequencies, more pressure is required. The main reason that can explain this phenomenon is the increased wavelength that particles need to pass until they reach the nodes. From this, a minimum pressure of 80 kPa is required for sorting at both frequencies. This in

contrast to the CM12-based device that only needs 60 kPa for a sorting efficiency of 100%. A velocity increase from 1 mm/s to 5 mm/s shows a stronger decrease in sorting efficiency for CM12-based device than for CM5-based device (100% to 88% and 100% to 34% for CM5-based and CM12 based devices, respectively). Thus, the relationship between the velocity and the sorting efficiency has a significant influence on the particle alignment.

Sorting efficiency [%]	Pressure over time for a velocity of 1 mm/s						Velocity over time	
	Frequency [MHz]	Pressure [kPa]					Pressure [kPa]	Velocity [mm/s]
Nr.		30	55	60	75	80	1	5
i	2	-	46	67	93	100	-	-
	4	85	98	100	-	-	80	100 88
ii	8 MHz	59	-	100	-	-	60	100 34

Table 4.3: Overview of sorting efficiencies depending on frequency and flow rate: i and ii represent the CM5-based and CM12-based devices, respectively.

Particle trajectories for a polystyrene particle (diameter $10 \mu\text{m}$) inside the microchannel are shown in Figures 4.7, C.4 and C.5. As mentioned in Figure 4.5, two forces play a key role in the behavior of particles in a microchannel, namely the drag force and the acoustic radiation force. For a fluid velocity of 1 mm/s and the CM5-based geometry, the minimum acoustic pressure for a particle sorting efficiency of 100% is 80 kPa (as seen in Fig. 4.7). This figure shows that around 3 seconds is needed for particle sorting over a distance of $4000 \mu\text{m}$ and a frequency of 2 MHz. Furthermore, for a frequency of 4 MHz, a sorting time of 3.5 seconds is required (Fig. C.4). A CM12-based device with a frequency of 8 MHz, pressure of 55 kPa and fluid velocity of 1 mm/s requires a time of around 2.2 seconds for particle alignment (Fig. C.5). The above-mentioned results indicate that particle sorting is possible in a few seconds' time for both designs.

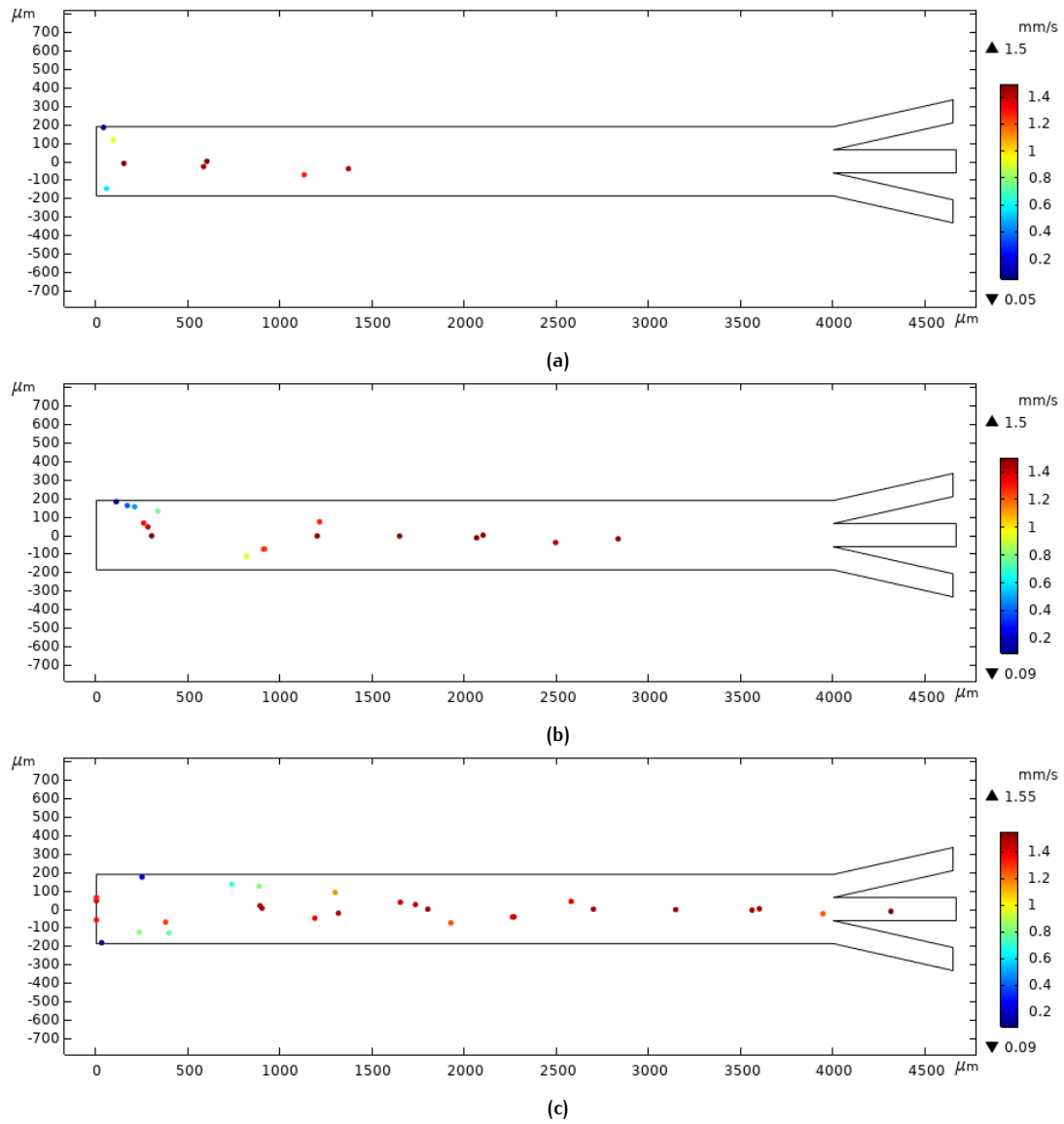


Figure 4.7: Particle trajectories inside the CM5-based microchannel for a pressure of 80 kPa and a frequency of 2 MHz at different times: (a) 1 s, (b) 2 s and (c) 3.1 s. A particle scale factor of 3 was applied to make the particle more visible.

5

FABRICATION AND ASSEMBLY

The fabrication and assembly methods used to create a functional BAW-based cell sorting system are discussed in this chapter. In the first section, the structures, including the microchannel designs, and fabrication are explained. Subsequently, the assembly of the experimental set-up and an overview of the overall BAW-based cell sorting system is provided.

5.1 THE FABRICATION OF THE MICROCHANNEL DEVICE

To create a microfluidic device where acoustic ultrasound can propagate into, microchannels were fabricated on either silicon or silicon on insulator (SOI) wafers. A process flowchart and a lithography mask were designed prior to fabrication.

5.1.1 Mask design

The dark-field photo-lithography mask is designed using the Cadence Design Systems software and ordered to create the structures presented in the previous chapter. A stepper machine uses the mask to expose the pattern on a wafer. Two designs were printed on a single reticle to reduce fabrication costs and time. For the fabrication of a successful microchannel, a small trench size needs to be considered such that the silicon can be etched while the oxide layer remains. Each microchannel is made of small squares of $1 \times 1 \mu\text{m}^2$ with a pitch of $1.5 \mu\text{m}$ (Fig. 5.1a). A close up of the port with the inlets or outlets can be seen in Figure 5.1b. However, since the width of the main channel is quite big (187.5 and $375 \mu\text{m}$), fabrication steps were performed twice to ensure that the oxide membrane for both designs remained intact. A mask design of the complete microfluidic devices is shown in appendix D.1.

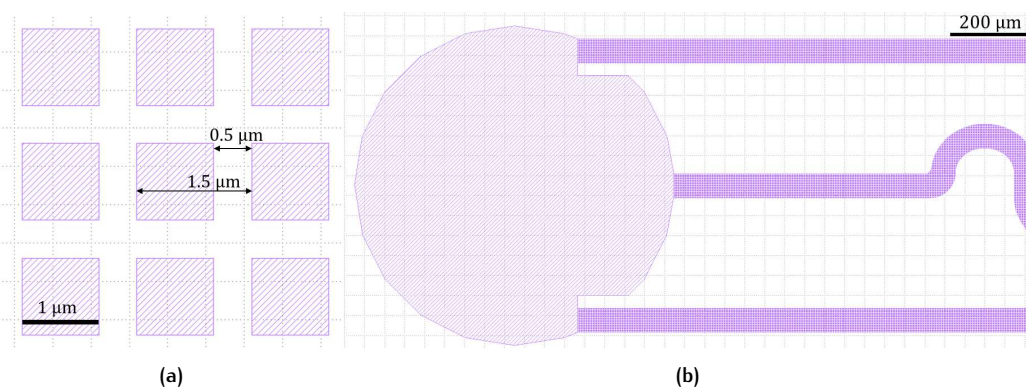


Figure 5.1: Section of the mask design used to fabricate the microfluidic designs: (a) enlarged section of the squares used to define the microchannel (b) section of a port with the inlets or outlets.

Step	Process	Description
1	SiO_2 PECVD	Deposition of a 500 nm oxide layer
2	Lithography	- Photoresist coating - Align mask for the microchannel designs - Exposure and development to UV light
3	SiO_2 dry etch	Oxide dry etching of the exposed area
4	Si DRIE	Si etching until the BOX layer of the SOI wafer and photo resist strip
5	SiO_2 PECVD	Seal holes in the oxide membrane by depositing a 3000 nm SiO_2 layer

Table 5.1: Summary of the fabrication processing steps performed on the front side of the wafers.

5.1.2 Fabrication process

The microfluidic devices are fabricated in the cleanroom of Philips MEMS Micro Devices in Eindhoven. Two fabrication processes for both designs were performed to determine whether the membrane would remain intact during fabrication (Fig. 5.2 and Table 5.1). To accomplish this, dummy silicon wafers were used to create the prototypes in order to evaluate if the membranes of the microchannels were properly fabricated. When the prototypes are well fabricated, SOI wafers will be used to fabricate the structures.

For the fabrication, the F2R process flow was used to create the embedded microchannels on the wafer. The procedure begins with an 8-inch silicon or SOI wafer. The SOI wafer is made of two layers of silicon separated by a buried silicon oxide (SiO_2) layer, also known as the BOX layer. The plasma-enhanced chemical vapor deposition (PECVD) method is used to deposit a 500 nm thick SiO_2 layer on the front side of the wafer. This is followed by a lithography step, where a positive photoresist layer is deposited on the front side of the wafer and the mask is positioned on top of this layer. After that, the top layer is exposed to UV light, which allows for patterning of the photoresist layer. During the SiO_2 dry etch, the exposed area will be patterned with SiO_2 etching until the silicon layer is reached. After the patterns are formed in the SiO_2 layer, silicon is etched with a deep reactive ion etch (DRIE) until the BOX layer is reached. To etch the microchannels, a variant of the DRIE method known as the Bosch process is used. Two different repeated cycles of etching, 18 and 22 cycles, were performed to examine the formation of scallops if present. Finally, a second SiO_2 layer was deposited to seal the holes in the oxide membrane. The entire flowchart is given in Appendix D.2.

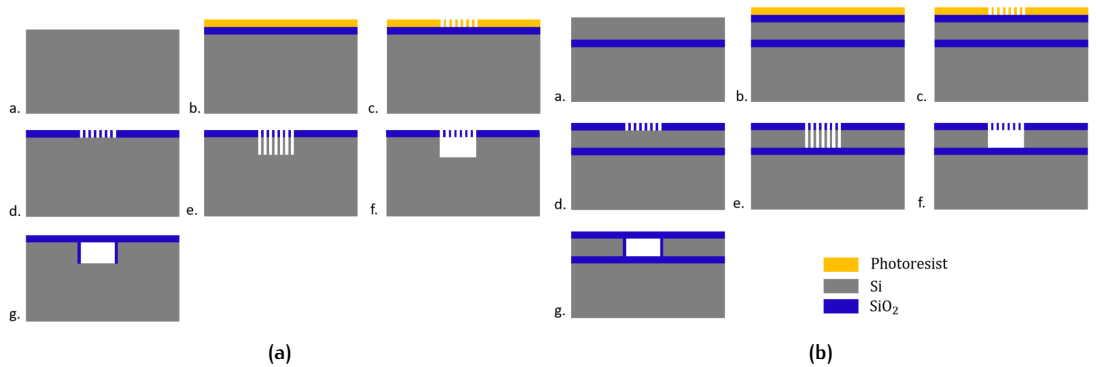


Figure 5.2: Fabrication process of the microfluidic channels (cross-section view): (a) silicon wafer and (b) SOI wafer.

5.1.3 Fabrication results

Experimental outcomes are presented based on DRIE etching. In total three dummy wafers and two process wafers SOI were processed.

Silicon wafers

The first fabrication process consists of the dummy wafer fabrication, where it is important to determine if the flowchart for both designs can be used for the SOI wafers. SEM top-view images of the microchannel were taken to inspect if the oxide membrane remained intact after 22 cycles of Si DRIE.

As shown in Figure 5.3, for a channel width of $187.5\ \mu\text{m}$ the oxide membrane remains intact (Fig. 5.3c). The oxide membrane, on the other hand, showed broken areas for a channel width of $375\ \mu\text{m}$ (Fig. 5.3d). This suggests that a large channel width ($\geq 375\ \mu\text{m}$) makes the SiO_2 membrane more prone to damage. As a result, the CM5-based microfluidic design is inapplicable for further processes in the flowchart, and only this silicon wafer will be used for further experiments to reduce the possibility of particle formation in the cleanroom. For the CM12-based microfluidic design, the membrane remained intact. Further steps in the process were taken to investigate the formation of embedded microchannels.

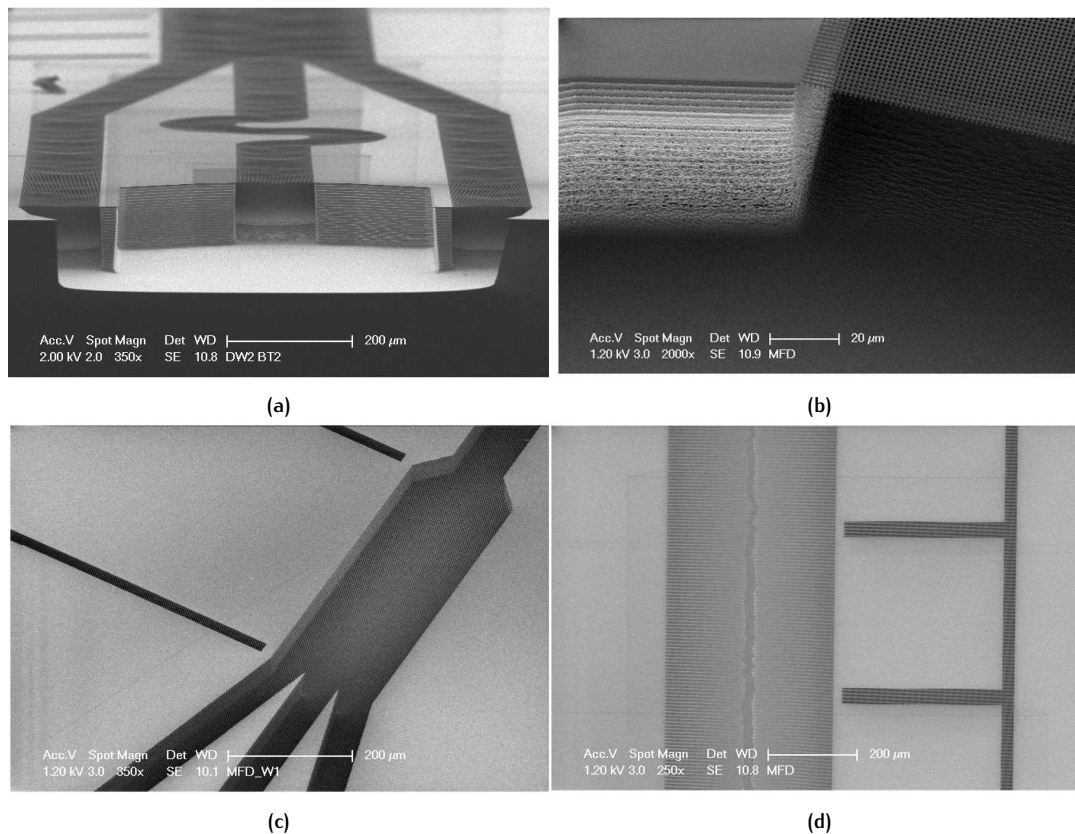


Figure 5.3: Results after the Si dry etch as SEM cross-sections and top-views of main channels: (a) cross-section at the port of the CM5-based microfluidic design, (b) cross-section at the in- or outlet with the visible square holes in the membrane used to define the microchannel, (c) top-view of the $187.5\ \mu\text{m}$ microchannel with an intact membrane and (d) top-view of the $375\ \mu\text{m}$ microchannel with a damaged membrane.

A Si DRIE cycle number of 22 was used to investigate if proper embedded microchannels with straight walls were formed. Figure 5.4a shows the cross-section of the developed microchannel with a depth of $67.5\ \mu\text{m}$. Relative straight walls are present with a slight undercut effect of $3\ \mu\text{m}$. This step shows that suitable mi-

crochannels with a depth of more than $40\mu\text{m}$ can be fabricated. A cycle number of 22 is therefore more than enough to form microchannels with a depth of $40\mu\text{m}$.

After the Si DRIE, the trenches were closed by depositing a second SiO_2 layer of $3\mu\text{m}$. This step allows for the sealing of the holes in the oxide membrane. Figure 5.4b depicts a perfectly closed membrane of the CM5-based microfluidic design. The trenches are nicely covered, which indicates that $3\mu\text{m}$ SiO_2 layer is sufficient to close the holes in the oxide mask layer. Therefore, the current recipe can be used for microchannel fabrication with a maximum width of $187.5\mu\text{m}$.

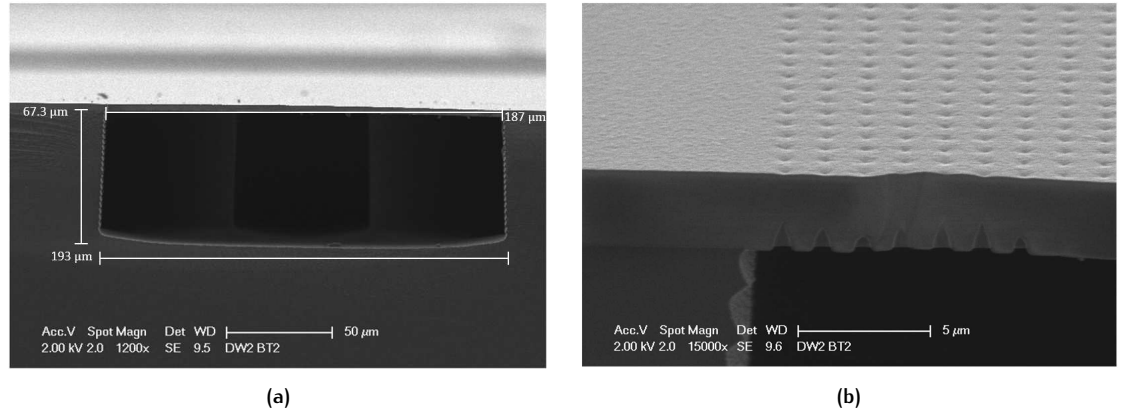


Figure 5.4: (a) SEM cross-section of a microchannel. (b) SEM cross-section of $3\mu\text{m}\text{Si}_2$ PECVD sealing of the membrane .

SOI wafers

Based on the previous results, the CM12-based microchannel design and a DRIE cycle number of 22 were enough to form properly embedded microchannels on the silicon dummy wafers. Thus, two SOI wafers were used for the fabrication of embedded microchannels with either 18 or 22 DRIE cycles. The two different DRIE cycle numbers were taken to validate if proper embedded microchannels are formed for SOI wafer and if significant scallop formations are present. The SOI wafer consists of a $40\mu\text{m}$ thick device layer on a 500nm thick BOX layer with a $380\mu\text{m}$ thick handle layer.

Cross-sections of both DRIE cycle numbers of 18 and 22 were taken after the final SiO_2 PECVD deposition was performed (Fig. 5.5). Both experiments showed nicely formed microchannels landing on the BOX layer with intact membranes. However, overetching is present on both wafers, which gives the notching effect near the BOX layer. This effect is present when the high-density plasma etching reaches an insulator material (e.g., SiO_2). The charging of the BOX-plasma etching interface result in ion deflection to the sidewalls, which enhances the etching at the insulator-silicon interface [36]. Since the overetching is quite small both devices can be used. For the following experiments, 18 DRIE cycles were used.

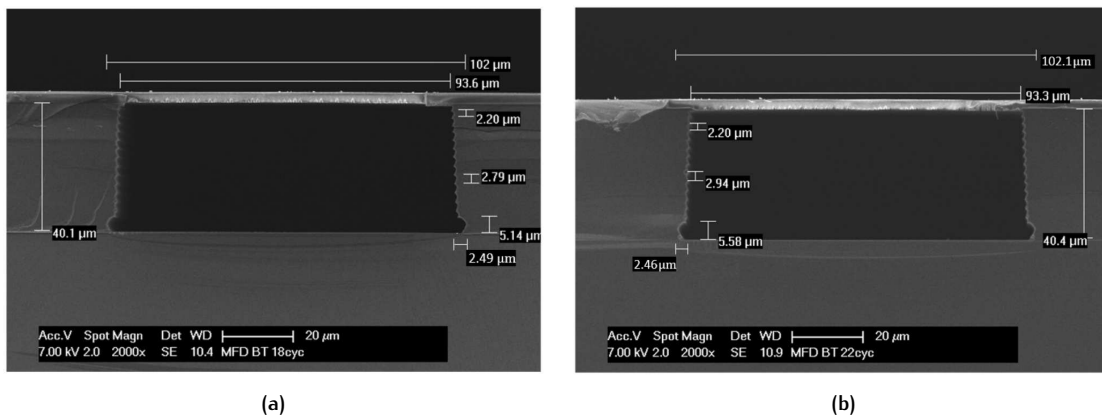


Figure 5.5: SEM cross-section for DRIE cycle numbers of (a) 18 and (b) 22.

5.2 EXPERIMENTAL SETUP

In this section, the assembly of the microfluidic devices and materials used to achieve a working device are discussed.

Microfluidic devices

Two different chips were used to build a microfluidic device, namely the silicon chips with a CM5-based microchannel and the SOI chips with a CM12-based microchannel.

As seen in Figure 5.6, the microfluidic devices consist of a chip and a tubing system. However, the silicon chips with defects in the membrane required an additional step of closing the membrane. Therefore, a glass plate with inlet and outlet ports were used for the CM5-based microfluidic chips (Fig. D.2). First, the SiO_2 top layer was stripped of this wafer and a glass plate of $19.25 \times 10.25 \mu m^2$ was glued on top of the silicon chip using Dymax 203-CTH-F adhesive that cures in seconds when exposed to UV light. The low viscosity of the glue gives a capillary effect between the silicon chip and the glass plate, which in turn allows for a very thin layer of glue that acts as the interface. To connect the syringe pumps with the microfluidic chips, stainless steel tips (0.61 mm inner diameter) were positioned in the ports of the glass plate, and glued with a high viscosity glue, the Dymax 203A-CTH-VT adhesive.

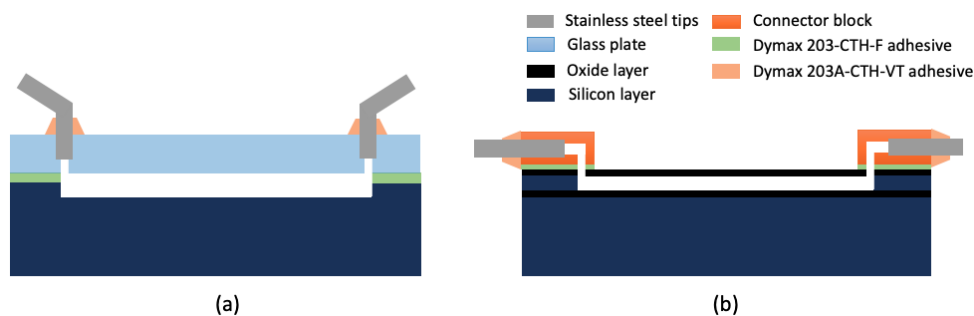


Figure 5.6: Cross-section of the microfluidic setup: (a) CM5-based microfluidic device and (b) CM12-based microfluidic device.

The membrane on the SOI chip remained intact, so that only a connector block was necessary to connect the chip to the tubing system (D.2c). A CAD design was made of the connector block and laser cut on polymethyl methacrylate (PMMA) to match the right geometry of the microfluidic device. The connector blocks and the tubing system were glued with the same technique as the silicon chips.

The acoustic sources used to create standing waves in the microfluidic channels were Capacitive Micromachines Ultrasound Transducers (CMUTs). CMUTs are made using a standard IC fabrication-based process that consists of multiple layers. The frequency range of the CMUT can be tuned by selecting the proper size of the drums. In this work, two CMUTs were selected for their frequency, namely a CM5 for a frequency of 2 and 4 MHz and a CM12 for a frequency of 8 MHz (Fig. 5.7). The CM5 has 64 elements, where each element contains 33 drums with a diameter of $355\ \mu\text{m}$ and a die thickness of $720\ \mu\text{m}$. The CM12 consists of 64 elements. Each element contains 42 drums with diameter of $120\ \mu\text{m}$. The silicon die thickness is $675\ \mu\text{m}$.

Figure 5.8 gives an overview of the considered acoustic-microfluidic device interfaces: microfluidic device next to the CMUT devices and microfluidic device on top of the CMUT devices.

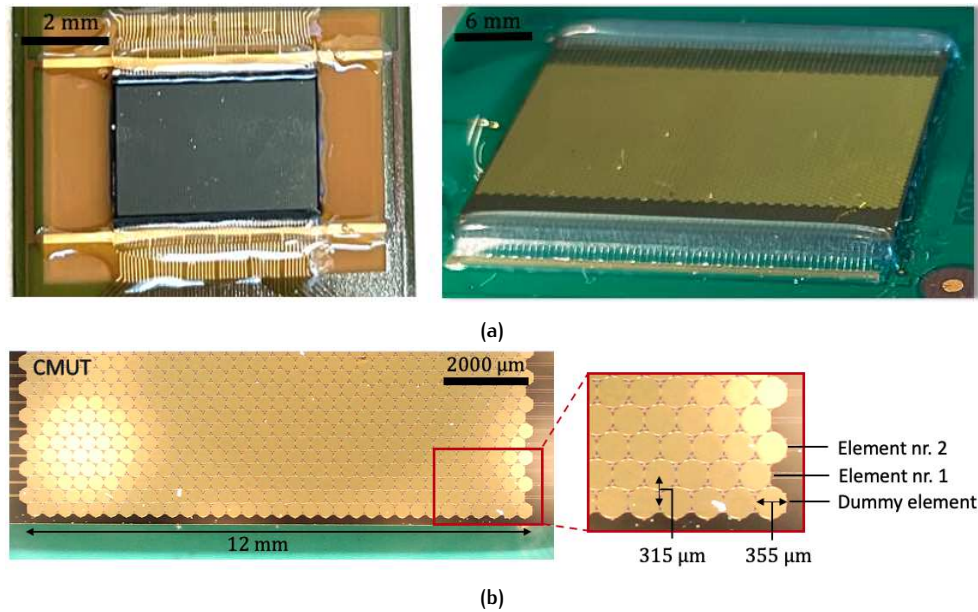


Figure 5.7: (a) Overview of the used CMUTs: CM5 (right) and CM12 (left). (b) Top view of CM5 CMUT devices. The diameter of a single drum and the pitch between two drums are $355\ \mu\text{m}$ and $315\ \mu\text{m}$, respectively.

System overview

The overview of the complete systems can be seen in Figure 5.9. The systems were built around a microscope, with the microfluidic device mounted on top of the platform. An encoded stereo microscope (Leica M205 C) with an external high-speed camera (iDS U3-3080CP) mounted on an objective is used in the optical setup. This enables the capturing of images and videos. The operational control of the microfluidic device is straightforward and requires a pressure source to pressurize the fluid in the microfluidic device. To actuate the fluid flows, one syringe pump (Harvard apparatus model 33) was connected to the inlet port and a tube was connected to the outlet port.

Two systems were built using the CMUTs' excitation method (Fig. 5.9a). The system with no phase excitation consists of a wave generator (Agilent 33250 A), an amplifier (EIN model 240L RF power amplifier), a source meter (Keithley 2400 source meter) and an oscilloscope (Agilent DS06032A) that are connected to a bias tee. The bias tee is connected to the CMUTs, which will excite the transducers, resulting in standing waves in the microfluidic channels. The system with phase excitation consists of a WUP board that is externally controlled by software. Two source meters were used to generate the bias voltage and the AC signal.

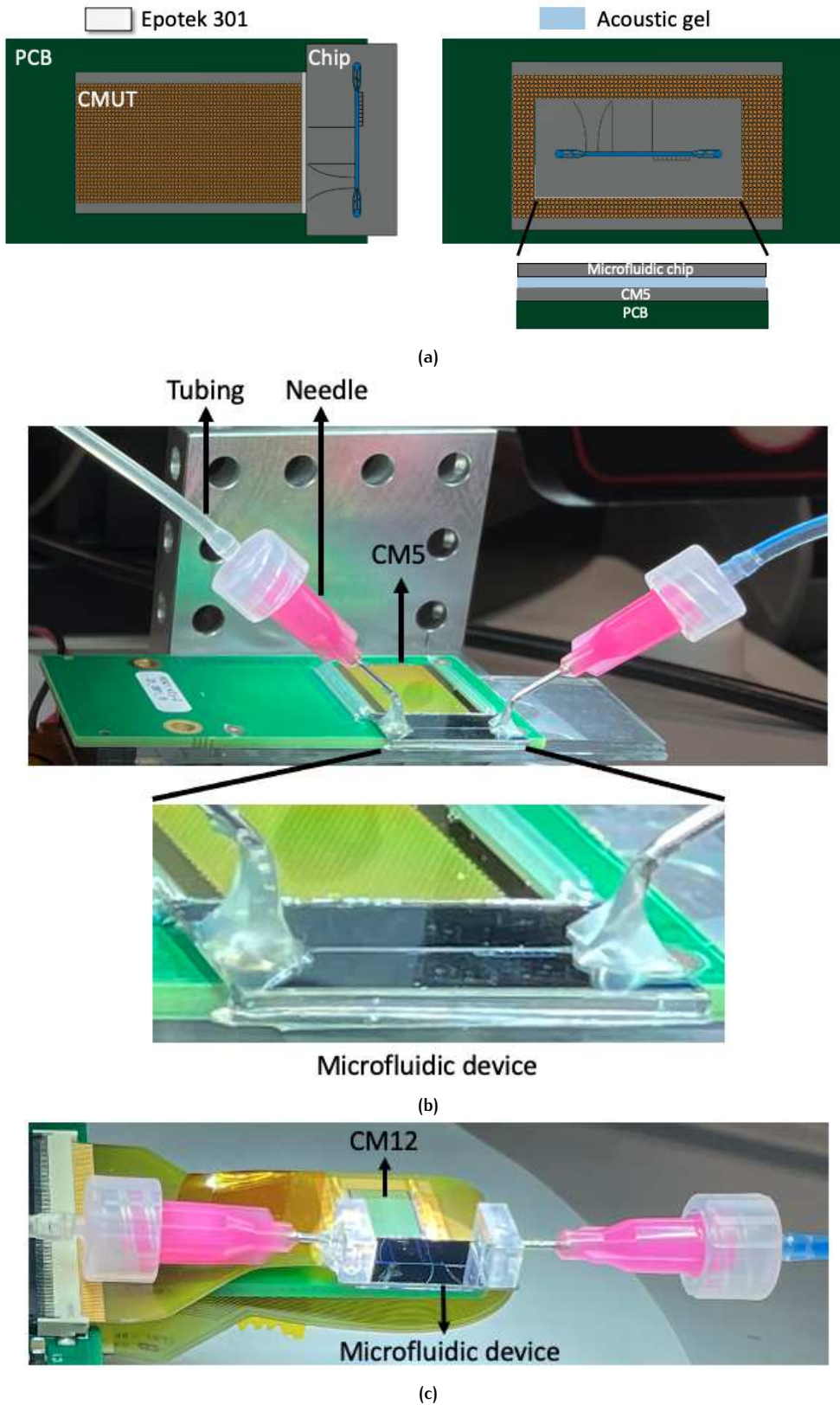


Figure 5.8: (a) Schematic overview of the different acoustic-microfluidic device interfaces: microfluidic device next to the CM5 CMUT devices (left) and microfluidic device on top of the CM5 CMUT devices (right). An acoustofluidic device made of microfluidic chips attached to CMUTs mounted on PCBs: (a) CM5-based microfluidic interface and (b) CM12-based microfluidic interface.

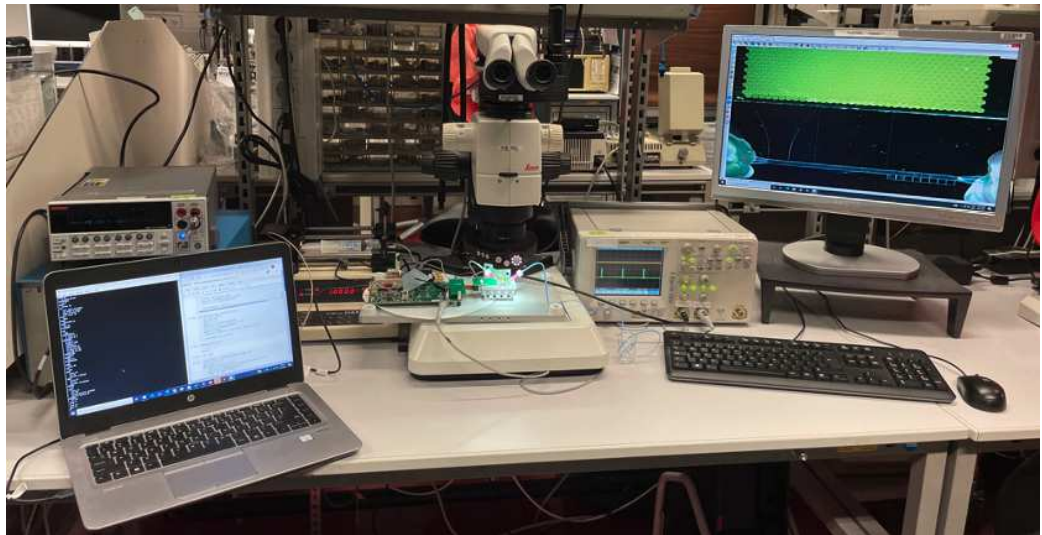
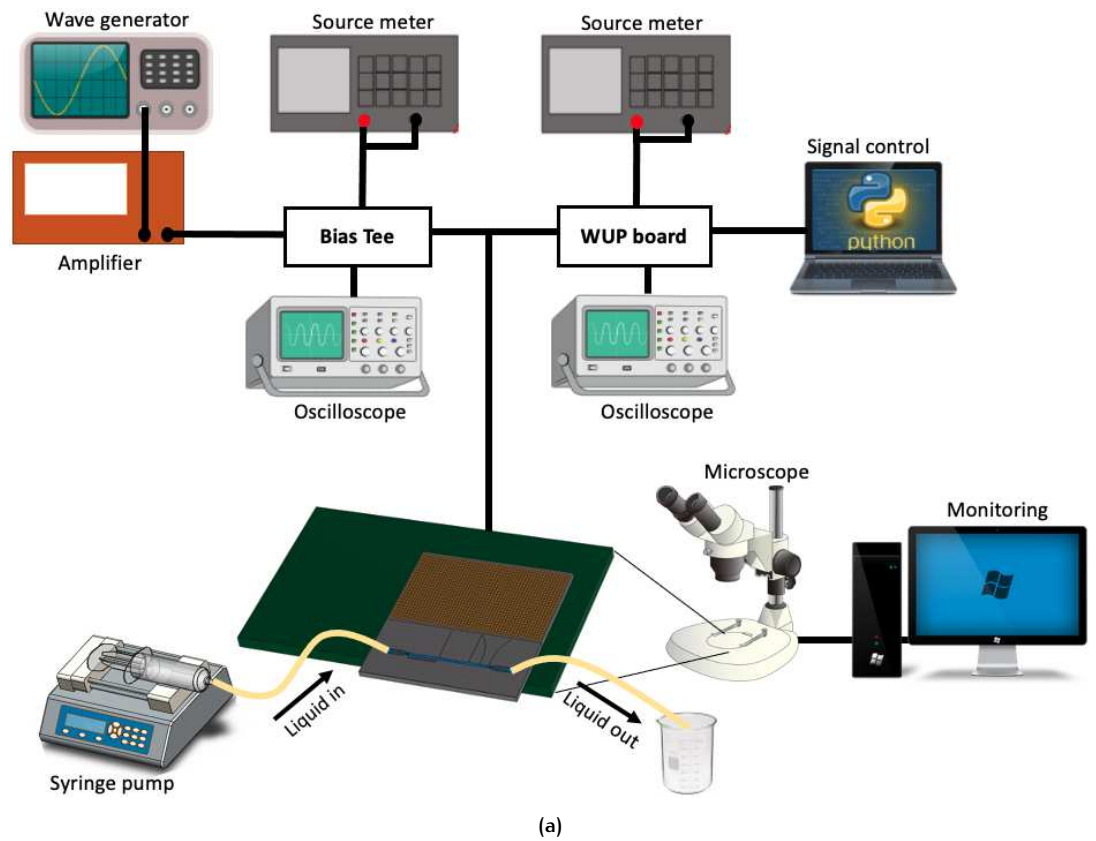


Figure 5.9: System overview for (a) CMUT excitation with no phase excitation (Bias Tee connection) and CMUT excitation with phase excitation (WUP board connection). (b) Experimental setup for phase excitation.

6 | RESULTS

The aim of this chapter is to investigate and discuss the influence of a CMUT-based sorting device on particle alignment in a microfluidic channel. The actuation modes and their associated acoustic-microfluidic interfaces are discussed in the first section. This is followed by an overview of particle alignment methods. Finally, the results of particle focusing experiments conducted using acoustic-microfluidic interfaces are presented.

6.1 ACTUATION

The actuation of the CMUTs for particle alignment in a microfluidic device is divided into two different interfaces, namely the sidewall and the top area of the CMUTs (Fig. 6.1). The main difference lies in the acoustic propagation, and the distance between the microfluidic channel and the CMUTs. The acoustic propagation for the sidewall and top interface is based on either acoustic propagation of the CMUTs through its die and into the sidewall of the microfluidic chip, or from the CMUTs directly into the microfluidic chip, respectively. Acoustic waves are formed during the excitation of the CMUTs, which creates a standing wave in plane with the silicon chip and orthogonal to the fluid flow, allowing for continuous particle alignment.

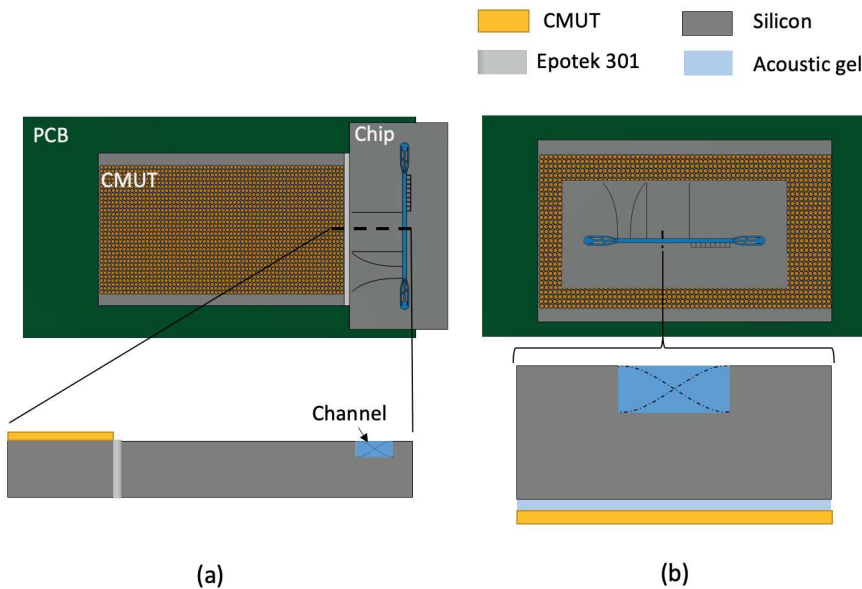


Figure 6.1: Cross-section overview of the assembled sorting device, showing the microchannel with the CMUTs either attached to (a) the sidewall or (b) on top of the transducers.

As shown in Figure 6.1, the contact area between the die of the CMUT and the microfluidic device is much larger for the top interface than the sidewall interface. A large contact area for the CMUT enables a good coupling of the acoustic energy into the silicon chip, which is an advantage of arranging the transducer in plane

with the microfluidic chip. While, the sidewall interface has a smaller contact area and an increased distance between the CMUT and the microchannel compared to the top interface. This can make it difficult to couple acoustic energy into the silicon of the microfluidic device for the sidewall interface. The degree of acoustic signal propagation is determined by the application of the matching layers (Epotek 301 and acoustic gel).

6.2 PARTICLE ALIGNMENT APPROACH

The experiments in Table 6.1 provide an overview of the CMUT excitation methods for each acoustic-microfluidic interface. The sidewall interface experiments were carried out using a phase delay amplification method. The experiments for the top interface, on the other hand, were carried out using an 8-element excitation method. To investigate the relationship between acoustic focusing and the microfluidic device, polystyrene particles with a diameter of $10\ \mu\text{m}$ were introduced into the microchannels. The actuation of the CMUTs causes the substrate to vibrate, resulting in standing waves with pressure nodes in the microfluidic channel. Due to the acoustic radiation force, particles will migrate to the nearest pressure node.

Acoustic-microfluidic interfaces	CMUT excitation method
I. Microfluidic device next to the CMUT (sidewall interface)	- Phase delay amplification
II. Microfluidic device on top of the CMUT (top interface)	- 8-element excitation

Table 6.1: Overview of the acoustic interface with their respective CMUT excitation method(s).

Both CM5 and CM12 CMUT chips were considered for particle alignment. However, both interfaces showed no evidence of particle alignment for the microfluidic devices and CM12 CMUT chips. The main reason for this seems to be that the acoustic propagation from the CMUT into the microfluidic device does not function properly. The prefabricated CM12 CMUT devices have thick adhesive layers at the side area of the die and on the PCB, as shown in Figure 5.7. The sidewall interface must be clean when assembling the microfluidic chip next to the CM12 CMUTs devices. However, no particle alignment was observed. This implies that the assembly was defective. The sidewall interface had a similar issue where the adhesive layers were very thick, resulting in the same problem.

As a result, the main focus of these experiments is on CM5 CMUT devices. The area of interest, the main channel of the microfluidic device, has an average depth of $60\ \mu\text{m}$ and a width of $375\ \mu\text{m}$. The locations I, II and III are taken into account for particle alignment analysis, as shown in Figure 6.2. Images captured during the experiments were processed in MATLAB using the image stacking procedure. To estimate the particle trajectory, the location of the particles were compared by analyzing images of particle sorting occurring within the channel.

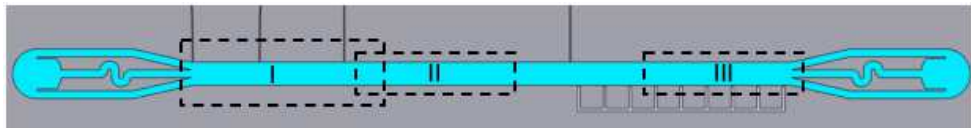


Figure 6.2: The chosen area of interest (I, II and II) in the microfluidic device for the particle alignment analysis.

6.3 ACOUSTIC-MICROFLUIDIC INTERFACES

6.3.1 Sidewall interface results

The operating conditions for the phase delay amplification were frequencies of 2 and 4 MHz, 20 V RF, a bias driving voltage of 150V, 15 cycles and a PRF of 15 kHz. When the microfluidic channel was operated at a flow rate of 1 $\mu\text{l}/\text{min}$ and in its fundamental resonance mode ($\lambda/2$), which corresponds to a frequency of 2 MHz, no particle alignment was observed. One possible explanation for the absence of this standing wave is that the acoustic forces for this mode were insufficient to produce particle alignment in the center of the channel. Another possibility is that phase alignment does not work properly in this device at a lower frequency due to the increased wavelength. The second harmonic mode (λ) for a frequency of 4 MHz, on the other hand, demonstrated clear particle focusing (Fig. 6.3). The particles are aligned at $3\lambda/4$ node, which correspond to a frequency of 4 MHz. However, particle alignment at the $\lambda/4$ node is barely visible due to the glue at the sidewall of this device. Within 3 seconds, particle alignment was achieved.

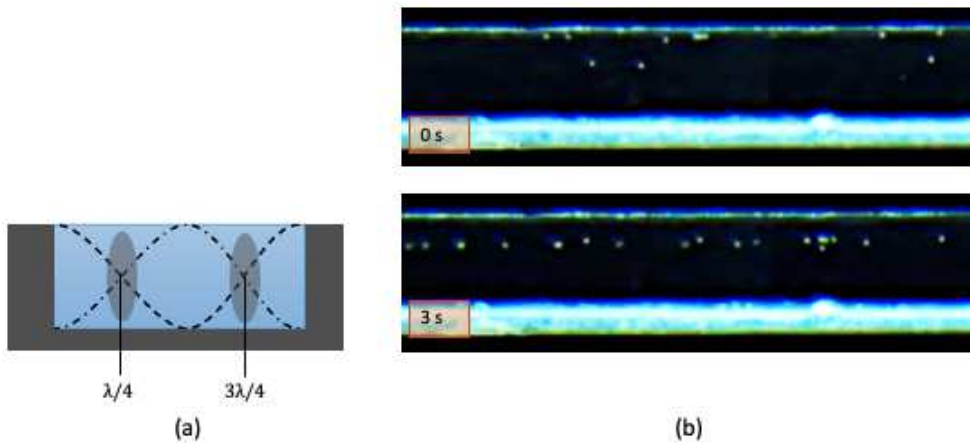


Figure 6.3: (a) A cross-sectional view of a standing wave in the microchannel with a wavelength of 1λ . Channel width: 350 μm . Channel depth: 60 μm . (b) Focusing of 10 μm particles after introducing a frequency of 4 MHz in 3 seconds.

Images of the particles were taken along the microchannel to quantify the particle focusing extent. As shown in figure 6.4, the area of interest II of the images were post-processed by filtering the background and averaging the gray value along the length of the channel section, resulting in an intensity profile in the channel width direction. The particle focusing band is represented by the gray value peak in this profile. Peaks are expected at 93.75 μm and 281.25 μm for a frequency of 4 MHz, corresponding to $\lambda/4$ and $3\lambda/4$ nodes, respectively. The particle focusing bands were analyzed and compared for a high and low particle concentrations.

Figure 6.4a shows a low particle concentration, with a peak at 276.3 μm and a particle focus bandwidth of 52.6 μm [256.6-309.2 μm]. This is within the sorting region for the top outlet of 250 to 375 μm . Furthermore, the peak corresponds to the second pressure node at $3\lambda/4$ with a deviation of 2%. In contrast to the high particle concentration shown in Figure 6.4b, two peaks corresponding to the two pressure nodes are visible at 89.6 μm and 302.2 μm . Each peak has a bandwidth of 134.4 μm [16.7-151.1 μm] and 117.5 μm [246.3-363.8 μm], which falls outside the sorting bandwidth region of 0 to 125 μm and 250 to 375 μm . As a result, both bandwidths are insufficient for proper particle alignment. A third peak is visible at 212.7 μm , where some particles are not properly aligned at a pressure node.

The focusing width increases significantly as particle concentration increases. A low particle concentration allows for proper particle alignment, whereas a high

particle concentration increases the bandwidth and limits the particle sorting ability. This demonstrates the importance of particle concentration in the efficiency of particle alignment. Another

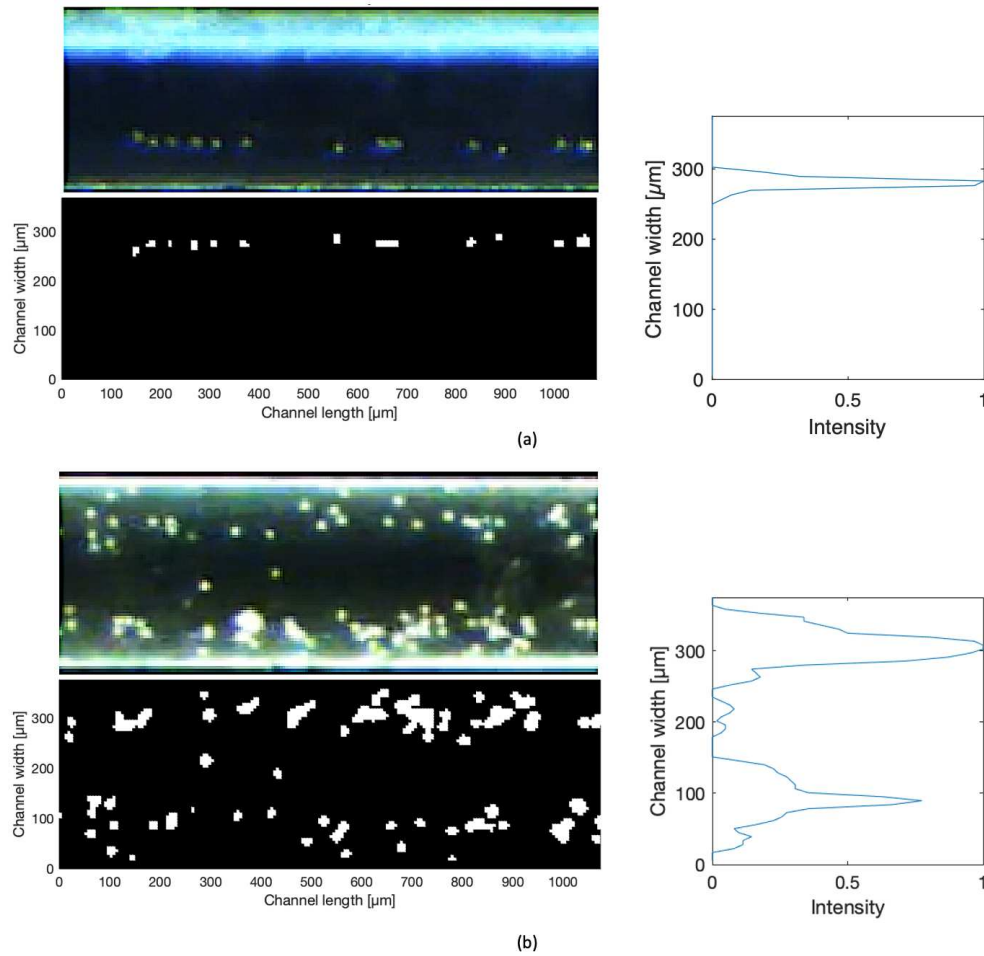


Figure 6.4: The particle focusing extent is characterized for (a) low particle concentration and (b) high particle concentration. The top image on the left represents the particle distribution at area II. The bottom image is a grayscale variant of the top image after a background filter has been applied. The average gray value profile in the channel width is represented by the curve on the right.

6.3.2 Top interface results

The microfluidic device was fixed on top of the CMUT devices to investigate the efficiency of acoustic focusing for the top interface. The following parameters were used to excite eight elements: a bias voltage of 150V, an RF voltage of 15V and 15 cycles.

As shown in Figure 6.5, particle focusing was observed in experiments with a flow rate of $1 \mu\text{l}/\text{min}$ and frequencies of 2 and 4 MHz, which corresponds to $\lambda/2$ and λ , respectively. Particles are properly aligned at each node corresponding to their specific frequency. This was accomplished in 6 and 3 seconds for 2 and 4 MHz, respectively. The decrease in particle alignment time for a higher frequency can be explained by equation (2.6), in which the higher operating frequency provides a higher particle focusing force, and the difference in distance to the pressure nodes for each frequency.

To investigate the particle focusing extent around the horn structure area and the straight walls area made in the microfluidic chip, a frequency change of 4 to 2 MHz

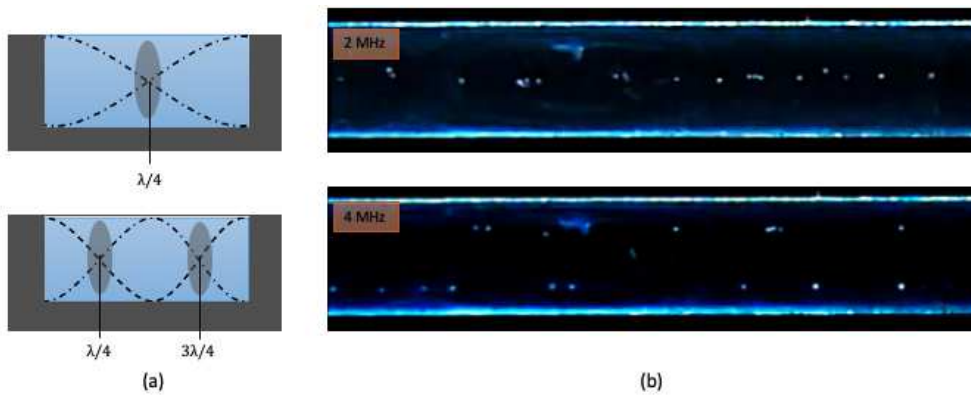


Figure 6.5: (a) Cross-sectional views of a standing wave in a microchannel with wavelengths of $\lambda/2$ and 1λ at area II. Channel width: $350 \mu\text{m}$. Channel depth: $60 \mu\text{m}$. (b) Focusing of $10 \mu\text{m}$ particles after introducing a frequencies of 2 and 4 MHz for the top and bottom image, respectively.

as a function of distance and time was performed at area I. As shown in Figure 6.6, the area around the horn structure shows particle focusing at 2 MHz within 4 seconds, whereas the other areas show an increase in time of up to 6 seconds. The particles at the horn structure area are aligned within a channel length of $225.6 \mu\text{m}$. While the areas next to the horn structure show an increase of 133.1 % in channel length ($300.3 \mu\text{m}$). As you move deeper into the area of straight walls, this increase decreases to 99.8 % ($225.0 \mu\text{m}$). The following results indicate the importance of structures created in a microfluidic chip for faster particle alignment over a shorter distance.

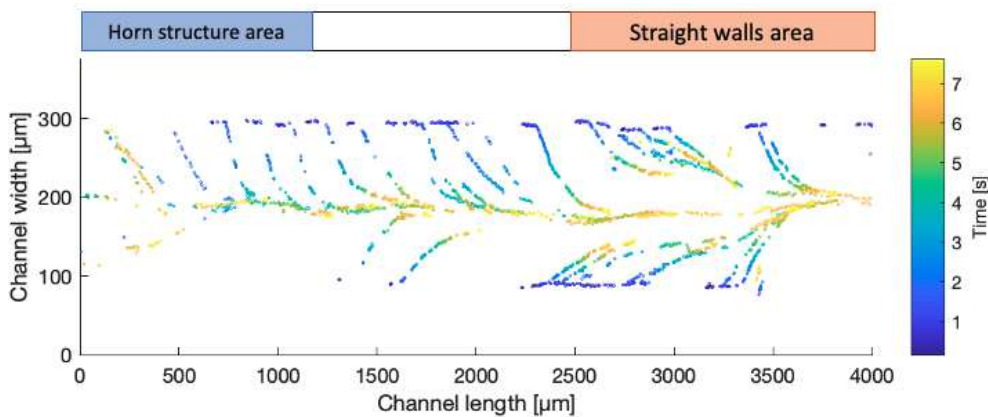


Figure 6.6: Particle trajectories at area I for a frequency change of 4 to 2 MHz.

The particle focusing extents were quantified for both frequencies (Fig. 6.7). The top image of Figure 6.7b shows the main gray value peak at $164.7 \mu\text{m}$ for 2 MHz, with a bandwidth of $42.0 \mu\text{m}$ [$136.7\text{-}178.7 \mu\text{m}$]. This falls within the sorting range of 125 to $250 \mu\text{m}$ at 2 MHz with a peak deviation of 12.2%. As shown in Figure 6.7a, the particles are properly aligned into the middle sorting outlet. The bottom image of Figure 6.7b shows two peaks for a frequency of 4 MHz. The peaks are observed at 91.8 and $287.0 \mu\text{m}$, which corresponds to the pressure nodes at $\lambda/4$ and $3\lambda/4$ with a deviation of 2.1% and 2.0%, respectively. The bandwidths for this frequency are $23.0 \mu\text{m}$ [$275.5\text{-}298.5 \mu\text{m}$] and $30.6 \mu\text{m}$ [$80.4\text{-}111.0 \mu\text{m}$]. This also falls within the sorting regions for this frequency.

These experiments show that at a frequency of 4 MHz, the particle focusing extent aligns more properly to its pressure nodes with smaller bandwidths than at

a frequency of 2 MHz. Nonetheless, the difference is within the sorting area, and proper particle alignment is still possible.

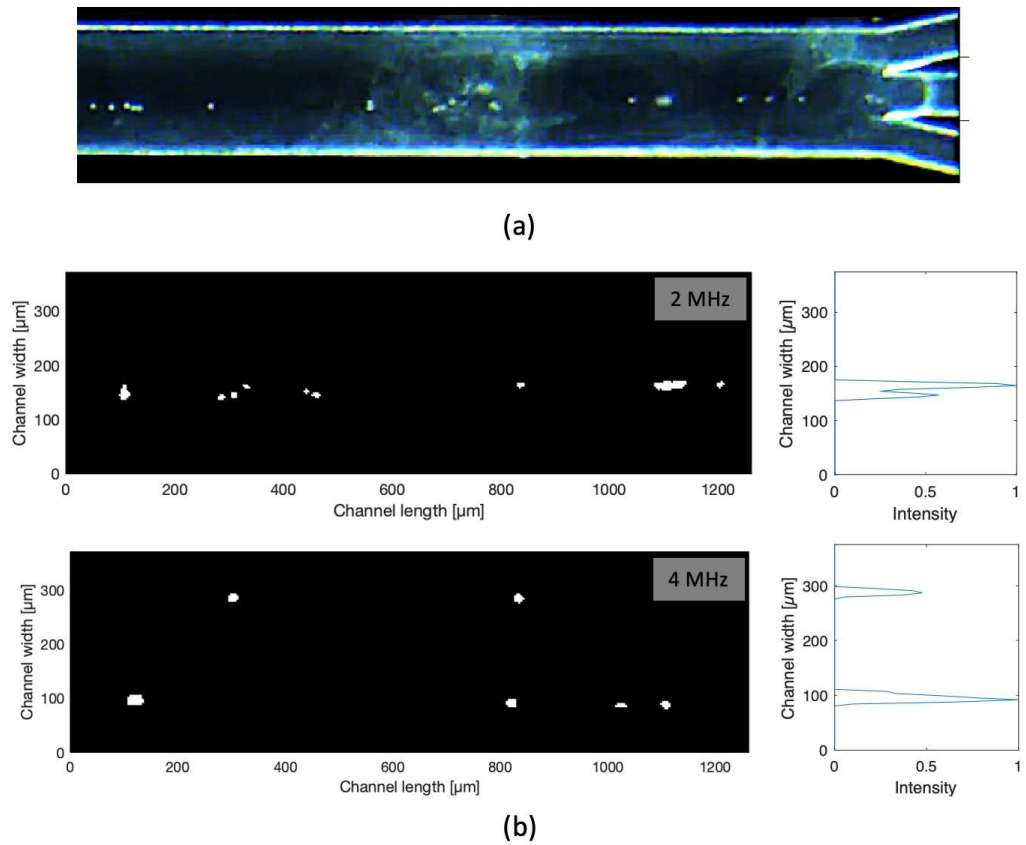


Figure 6.7: (a) Focusing of particles after introducing a frequency of 2 MHz at area III. (b) The top and bottom grayscale images show particle focusing extent characterized for frequencies of 2 and 4 MHz, respectively. Each average gray value profile in the channel width is shown on the right side.

6.4 CONCLUSION

Successful particle separation in a microchannel in the silicon chip using CMUTs was demonstrated. The ultrasonic excitation of the microfluidic channel, whose frequency depends on the channel width, enabled particle alignment. Particles separated as a result in either the center or the side outlets.

Both interface results indicate that CMUT-based acoustic focusing will be applicable as a particle sorting device. However, more research is required in this field to investigate the acoustic behavior of these interfaces and improve sorting efficiency.

7

CONCLUSIONS

In this thesis, a novel acoustic based microfluidic platform using CMUTs for particle separation was investigated. Two different acoustic-microfluidic device interfaces were considered, namely the sidewall and the top area of the CMUT. The advantages and disadvantages of each interface is summarized in Table 7.1.

Prior to the experiments, the presence of an acoustic sidewall pressure was investigated to determine if the sidewall interface is suitable for particle sorting. Based on the results of the experiments, it can be concluded that acoustic pressure exists at the sidewall of a collapse-mode CMUT. A phase alignment approach was used to increase the output pressure, which improved by 6.4 times compared to when no phase alignment was used.

Interfaces	Advantages	Disadvantages
I. Microfluidic device next to the CMUT (sidewall interface)	- Integration of CMUTs and the microfluidic channel in the F2R platform - Great design freedom	- Weak ultrasound coupling into the microfluidic channel
II. Microfluidic device on top of the CMUT (top interface)	- Strong ultrasound coupling into the microfluidic channel	- Either attach two separate devices or double-sided processing

Table 7.1: Comparison of different acoustic-microfluidic interfaces for particle alignment.

After confirming the presence of an acoustic pressure, simulations were made to determine the microfluidic design and whether particle alignment is possible. The integration of CMUTs and a microfluidic device on a single device was not possible due to time and capacity constraints. Thus, prefabricated CMUT devices were used for further investigation. While the microfluidic devices were created using the silicon processing-based F2R platform. Both parts were assembled into one of the two interfaces and investigated for the presence of particle alignment.

The results showed that polystyrene particles with a diameter of $10 \mu\text{m}$ were successfully aligned within a few seconds and separated with high efficiency. Multiple CMUT elements were simultaneously excited at the top interface device, demonstrating particle sorting at both wavelengths of $\lambda/2$ and λ , which corresponds to a frequency of 2 and 4 MHz, respectively. Furthermore, particle sorting is faster in the microfluidic channel next to structures integrated into the microfluidic device, such as the vacuum horn. By using a phase alignment approach, the sidewall interface device demonstrated only sorting at a wavelength of λ . This indicates that the phase alignment approach does not work properly for a frequency of 2 MHz. Nevertheless, the first demonstration of sheathless flow focusing and separation of particles were shown with CMUTs as an acoustic source.

This acoustic-based sorting method has a lot of potential as a component in lab-on-a-chip systems for biological applications. The ability to selectively excite different CMUT elements with the possibility of phase alignment, the broad bandwidth of the CMUTs, batch fabrication, and IC integration are the main advantages of the current device over existing acoustic sorting devices. In further research, it would be recommended to integrate these acoustic-microfluidic interfaces into a single device. One concept design is to fabricate the CMUT next to the microfluidic channel, while another is to fabricate the CMUT on the backside of the microfluidic device. This will improve the efficiency on several levels by decreasing the distance between the transducers and the microfluidic device and removing unnecessary layers.

Method	Transducer	Substrate	Resonance frequency	Flow rate	Sorting rate	Comments	Reference
SSAW	2 standard IDT	<i>LiNbO₃</i>	12.6	0.6-2 μ L/min	13,000 particles/min	- 80% sorting efficiency - Sheath flow focusing needed	[9]
	2 Focused IDTs	<i>LiNbO₃</i>	38.8	0.25 m/s	3,300 cells/s	- Sheath flow focusing needed - Fluorescence cell marking needed for single cell sorting	[10]
TSAW	1 adjusted IDT	<i>LiNbO₃</i>	162-164	1.5 ml/h	5,000 cells/s	- Inertial flow focusing (spiral channel) - Sheath flow focusing needed - Fluorescence cell marking needed for single cell sorting	[12]
	1 adjusted IDT	<i>LiNbO₃</i>	140-150	-	200-2000 cells/s	- 100% separation efficiency - Fluorescence cell marking needed for single cell sorting	[22]
	focused IDT	<i>LiNbO₃</i>	133.3	3.5 mm/s	-	100% separation efficiency - Sheath flow focusing needed	[31]
Tilted SSAW	2 IDT	<i>LiNbO₃</i>	19.4	2 μ L/min	10,000-20,000 cells/min	- Sheath flow focusing needed - 99% sorting efficiency for particles - 71% sorting efficiency for cancer cells	[37]
	2 IDT	<i>LiNbO₃</i>	19.98	4-5 mm/s	-	- Sheath flow focusing needed - 96.67, 89 and 96.77% (1, 5 and 10 μ m particle diameter, respectively)	[11]
BAW	PZT	Silicon	1- 2	<0.2 mL/min	-	- PZT glued backside chip with epoxy - No sheath flow focusing needed - 90% separation efficiency	[23]
	PZT	Silicon	2.03	20 μ L/min	-	- PZT glued backside chip with cyanoacrylate glue	[29]
	PZT	Silicon	1.83-1.85	2-3 μ L/min	-	- No sheath flow focusing needed PZT glued at the top next to the channel	[24]
	PZT	aluminum alloy 6061	3.13	100 μ L/min	-	100 % sorting efficiency PZT glued at top next to channel with epoxy	[30]
	1-3 composite transducer	Stainless steel	0.24	5 mL/min	-	- No sheath flow focusing needed - 98.2% sorting efficiency - PZT glued under channel with epoxy - 88.4% blood cells and 86.2% platelet sorting efficiency - Sheath flow focusing needed	[13]

Table A.1: Comparison of different acoustic particle separation devices.

B | ACOUSTIC MEASUREMENT DATA

This appendix shows the acoustic pressure distribution for CM₁₂ CMUT devices and the comparison between the output pressure as a function of the voltage of a CM₅ CMUT devices with and without a phase alignment approach.

B.1 CM₁₂

Measured acoustic pressure of a single excited CM₁₂ element: (a) Element 92, (b) element 94 and (c) element 96. Element 96 is the excited CMUT element that is the closest to the sidewall.

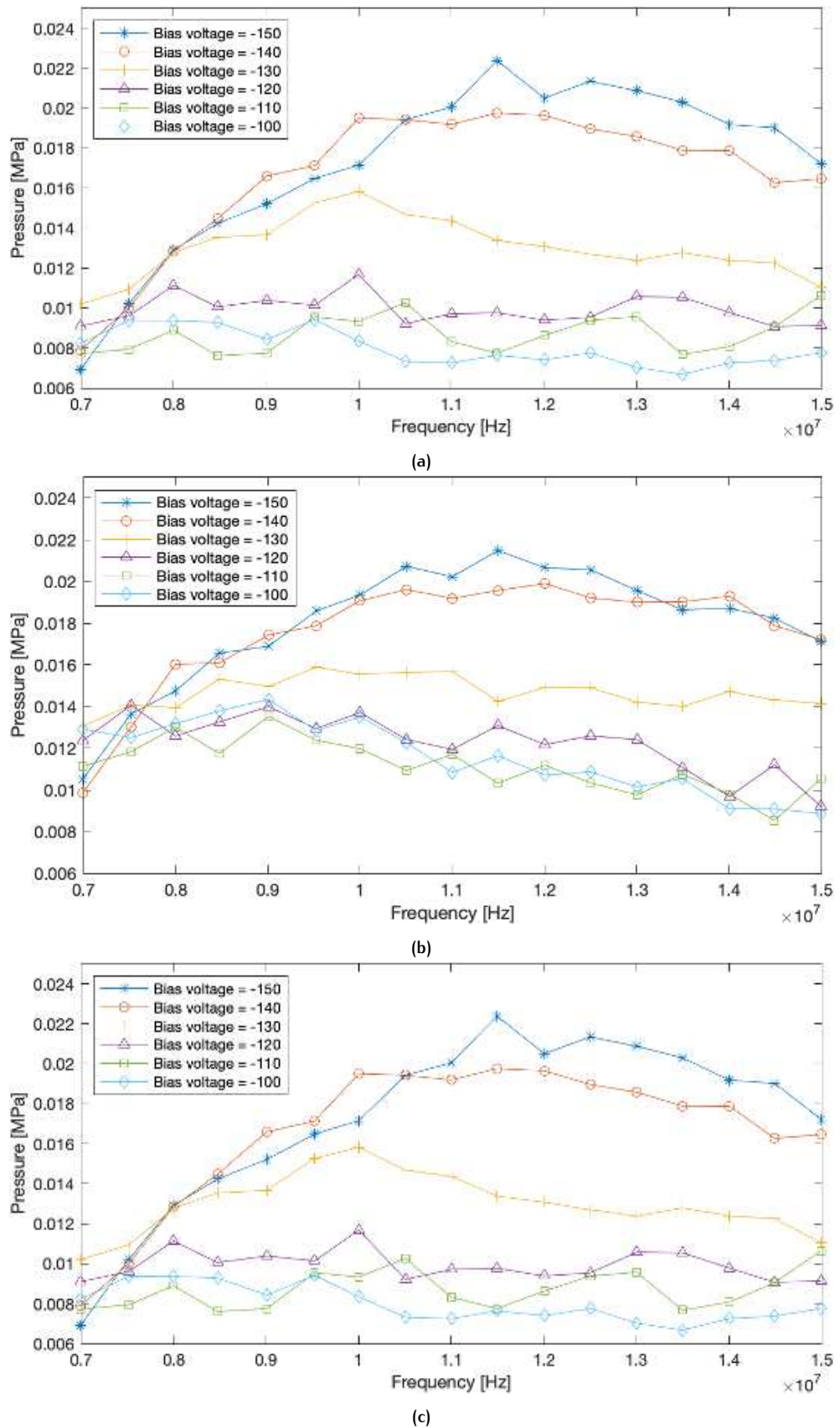


Figure B.1: Measured acoustic pressure of a single excited CM12 element: (a) Element 96, (b) element 94 and (c) element 92.

B.2 CM5 PHASE ALIGNMENT

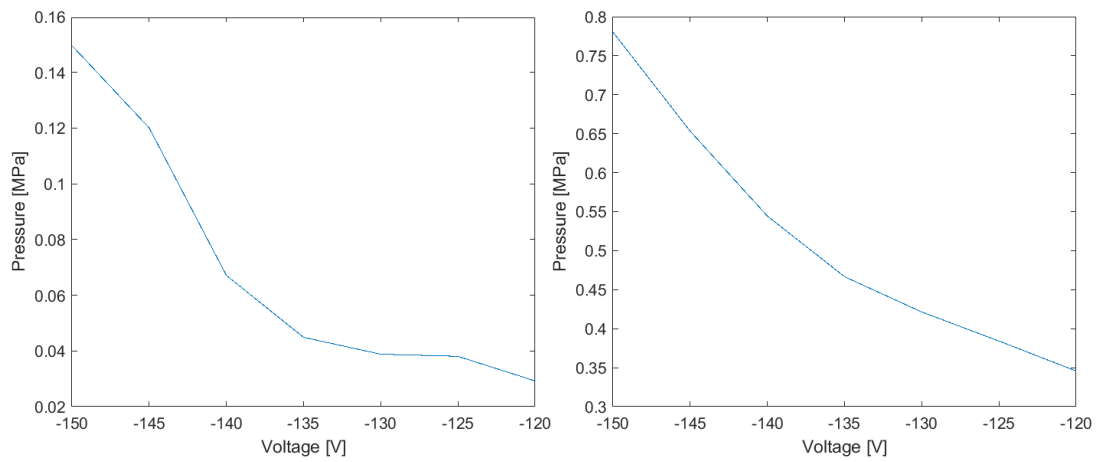


Figure B.2: Measured acoustic pressure of multiple elements excitation of a CM5: (a) reference and (b) phase alignment.

C | SIMULATION DATA

Results for the characterization of the fluid flow and acoustic behavior on particles in the given channel designs are presented as velocity profile, acoustic pressure distribution, and particle trajectory.

C.1 VELOCITY PROFILE FOR CM12-BASED MICROCHANNEL

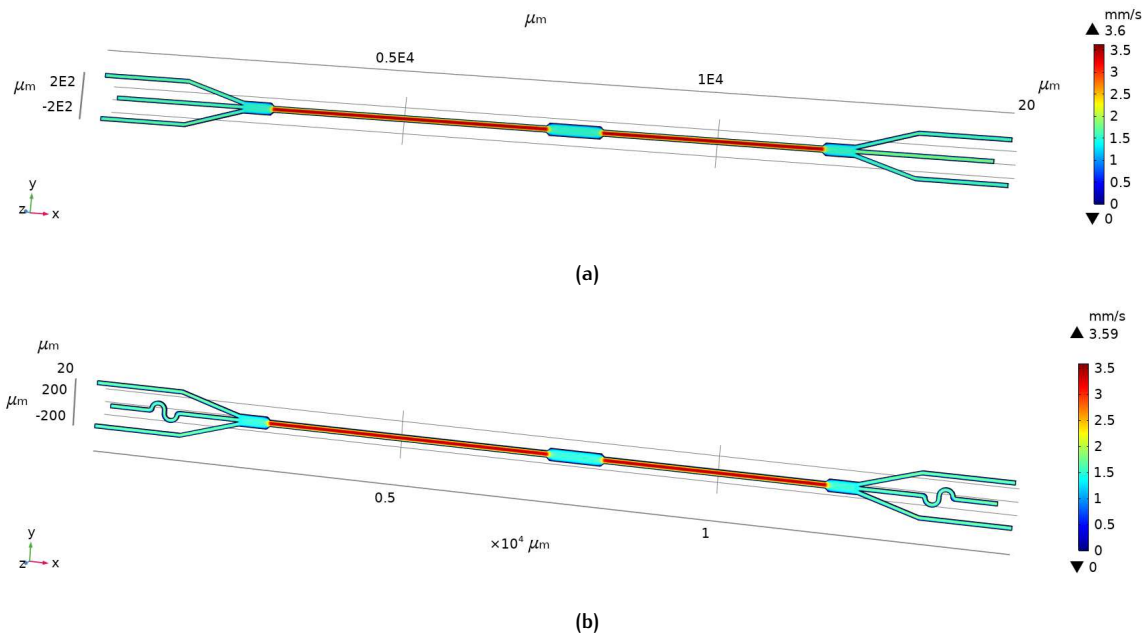


Figure C.1: Simulated cross sectional velocity profile of the fluid flow in the CM12-based microchannel at $z = 20 \mu\text{m}$ and inlet velocity of 1 mm/s .

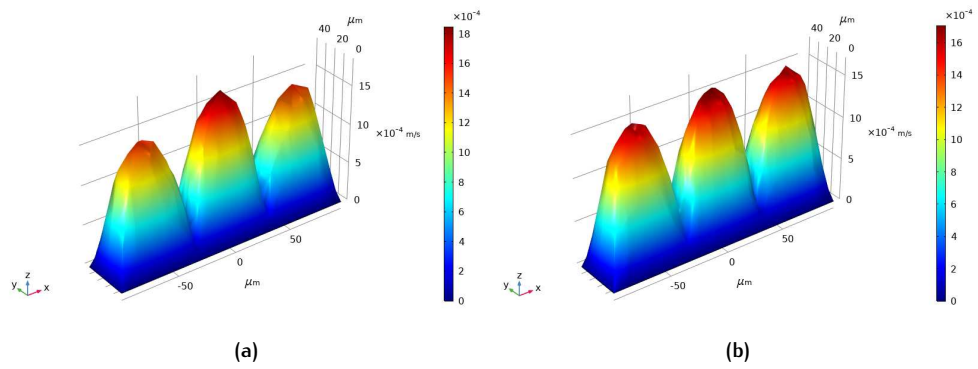


Figure C.2: 3D flow profile taken at the intersection of the three outlets in a CM5-based microchannel under condition of an inlet velocity of 1 mm/s: (a) scenario 1 and (b) scenario 2.

C.2 FLOW AND PRESSURE DISTRIBUTION IN CM12-BASED DEVICES

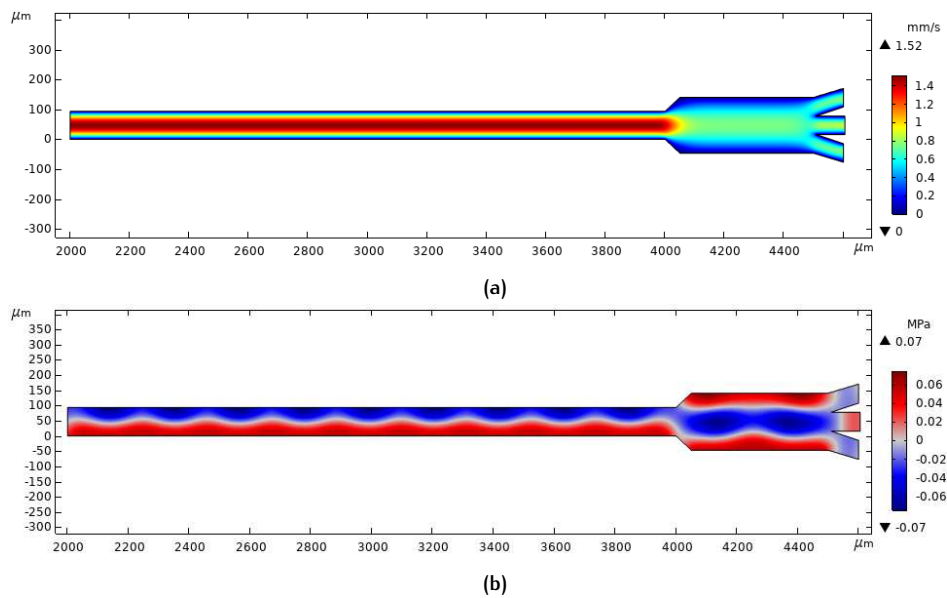


Figure C.3: CM12-based microchannel design. (a) Velocity distribution of the fluid flow along the streamlines inside the microchannel. (b) Wave plot (red positive, blue negative) of the acoustic pressure field at resonance in a water-filled microchannel with a frequency of 8 MHz and applied pressure of 60 kPa.

C.3 PARTICLE SORTING FOR CM5-BASED DEVICES

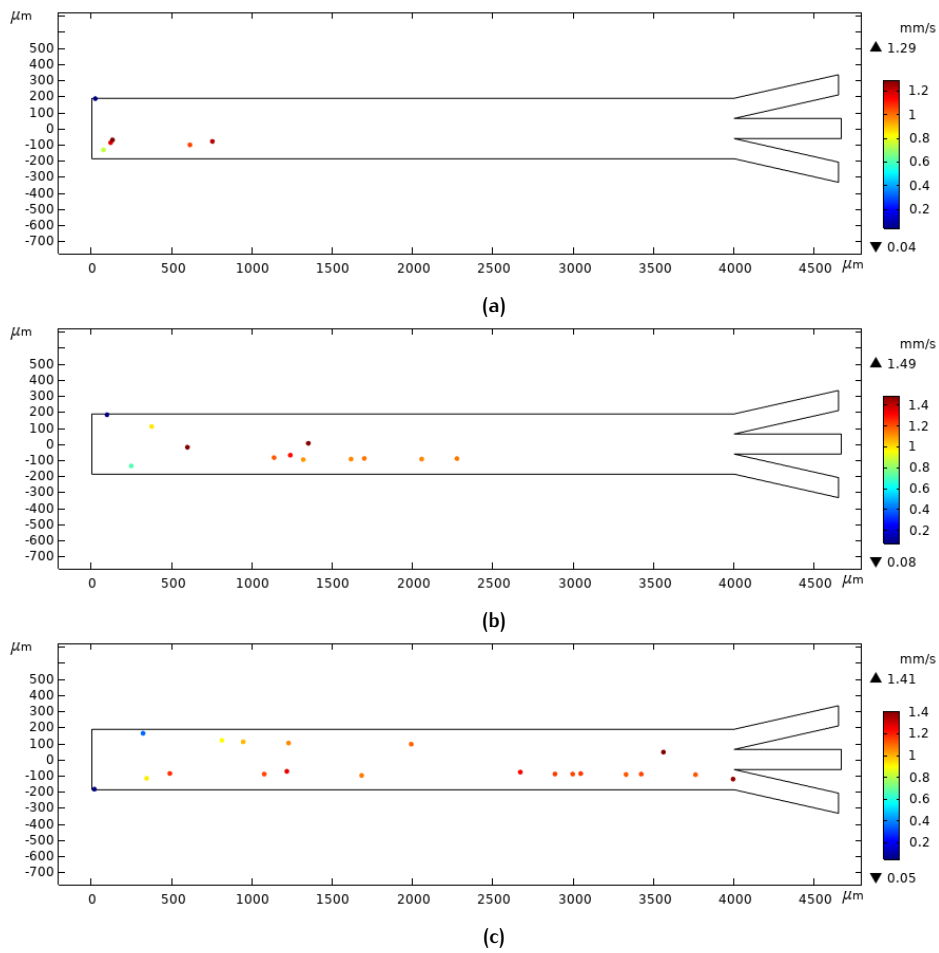


Figure C.4: Particle trajectories inside the CM5-based microchannel for a pressure of 80 kPa and 4 MHz at different times: (a) 0.7 s, (b) 2 s and (c) 3.5 s. A particle scale factor of 3 was applied to make the particle more visible.

C.4 PARTICLE SORTING FOR CM12-BASED DEVICES

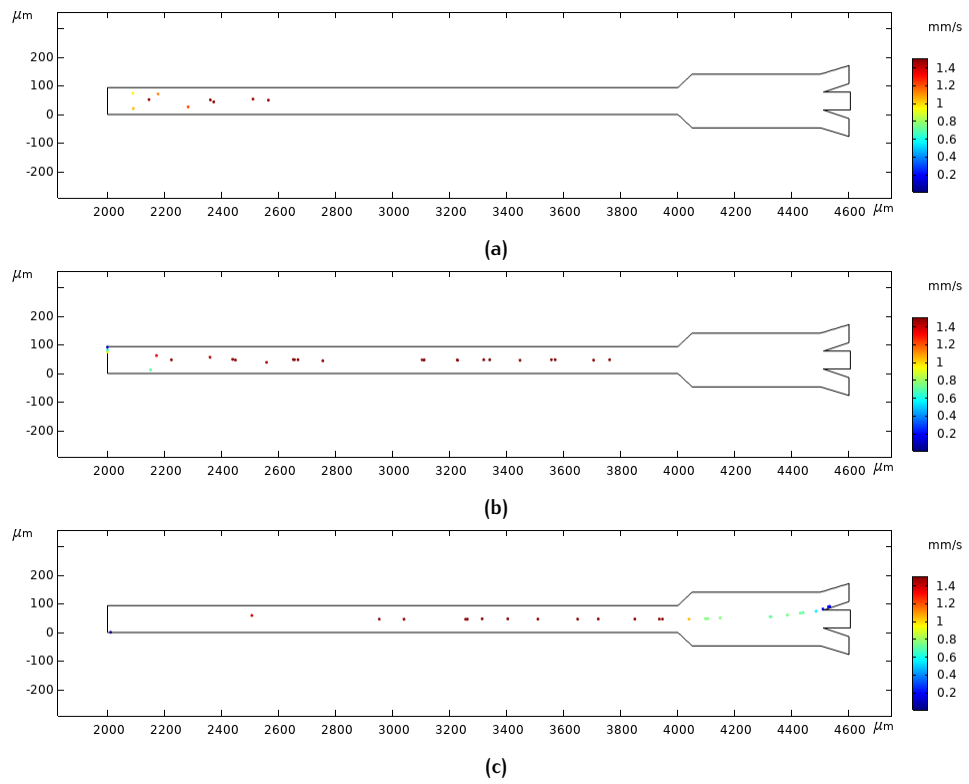
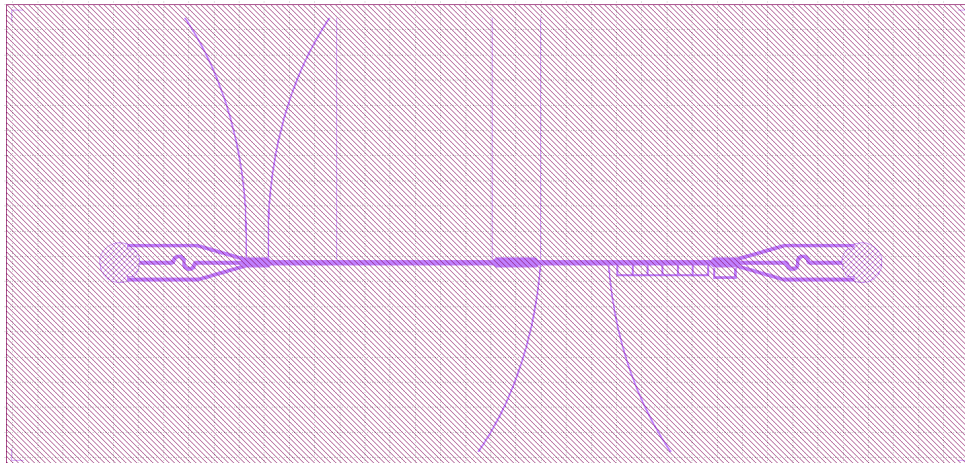


Figure C.5: Particle trajectories inside the microchannel for 55 kPa at different times: (a) 0.4 s, (b) 1 s and (c) 2.2 s

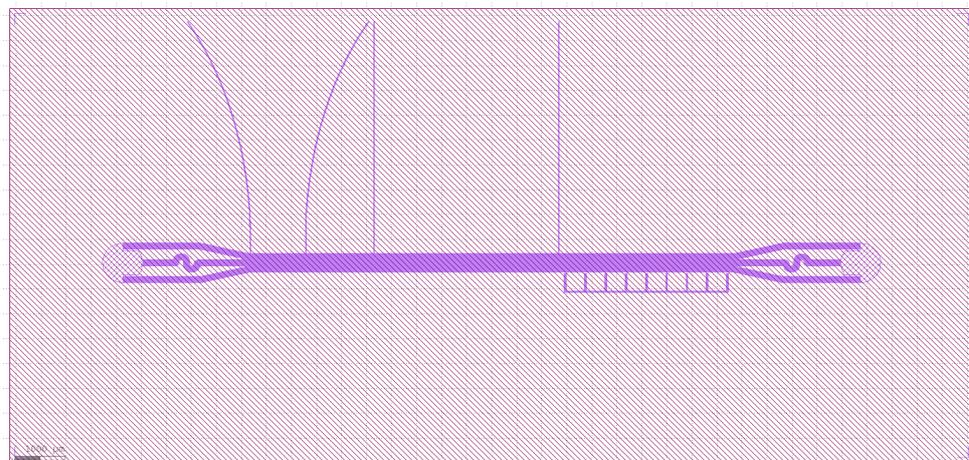
D | FABRICATION DATA

D.1 MASK DESIGN

This appendix shows the mask design that has been made to manufacture the microfluidic chips.



(a)



(b)

Figure D.1: Mask design of (a) CM12-based microfluidic chip and (b) CM5-based microfluidic chip.

D.2 FLOWCHART

Wafer step	Process	Instruction
1	Start technical stage	Wafer enters cleanroom
2	Logistic step	Contact batch owner
3	Logistics step	Laser marking
4	Thickness stress resistance (MEA) measurement	pre-measurement 200 mm silicon
5	Logistic step	Release batch for production
6	Wet-clean step	cleaning process using pre-furnace, non-metal
7	Wet-clean step	rinse and dry process using the SRD program
8	PECVD SiO_2	Deposition of 500 nm SiO_2
9	Thickness stress resistance (MEA) measurement	Thickness measurement of the silicon- SiO_2 using the NanoSpec
10	Thickness stress resistance (MEA) measurement	post-measurement
	Split wafers	
11	Lithography for CM5-based design	Coating and developing of HMDS on the surface of 1300 nm
12	Lithography for CM12-based design	Coating and developing of HMDS on the surface of 1300 nm
	Merge wafers	
13	Dry etch SiO_2	Dry etch process of SiO_2 with an exposure of 200 mm
14	Dry etch	Si dry etch process with a deep exposure of 200 mm
15	Inspection flow	Bright field
16	Dry strip	Strip $< 1.5 \mu m$ using a microwave
17	PEC SiO_2	3000 nm low stress PECVD at 400 °C
18	MEA and SEM	Investigation of the finalized wafers using MEA and scanning electron microscope (SEM)
19	Logistic step	Release batch for production
20	SEQ	Sequence of steps spanning multiple areas, including packaging of wafers to labeled single wafer boxes , deliver product wafers to costumer, and dispose or store dummy-wafers

Table D.1: Summary of processing steps performed on the frontside of all wafers.

D.3 COMPONENTS

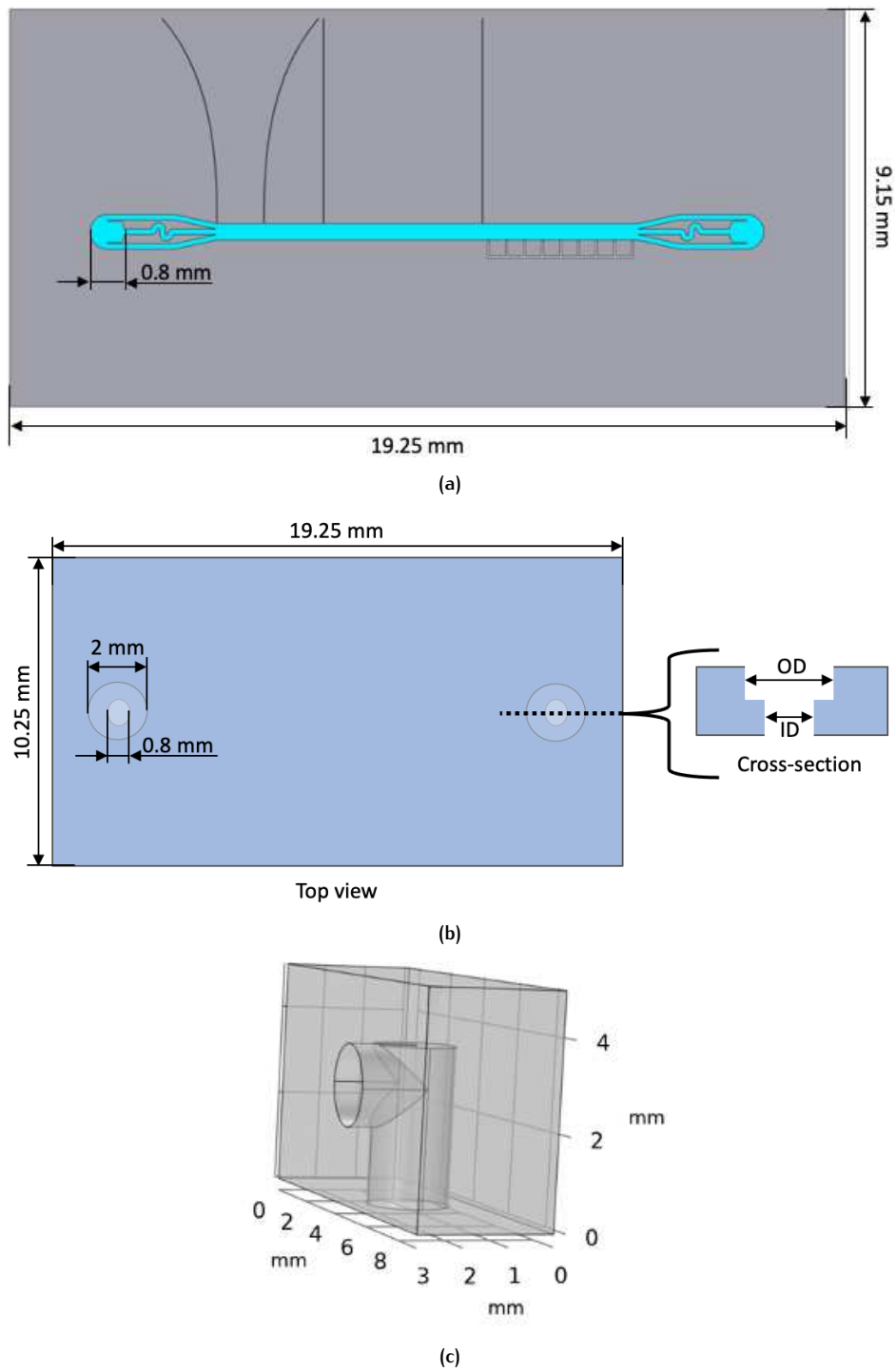


Figure D.2: Schematic overview of (a) the CM5-based microfluidic device, (b) the glass plate with a specific inner and outer diameter (ID and OD) and (c) the connector block.

BULK ACOUSTIC WAVE BASED MICROFLUIDIC PARTICLE SORTING WITH CAPACITIVE MICROMACHINED ULTRASONIC TRANSDUCERS

Shinnosuke Kawasaki¹, Jia-Jun Yeh¹, Marta Saccher¹, Jian Li¹, and Ronald Dekker²

¹Delft University of Technology, NETHERLANDS and

²Philips Research, NETHERLANDS

ABSTRACT

The main limitation of acoustic particle separation for microfluidic application is its low sorting efficiency. This is due to the weak coupling of surface acoustic waves (SAWs) into the microchannel. In this work, we demonstrate bulk acoustic wave (BAW) particle sorting using capacitive micromachined ultrasonic transducers (CMUTs) for the first time.

A collapsed mode CMUT was driven in air to generate acoustic pressure within the silicon substrate in the in-plane direction of the silicon die. This acoustic pressure was coupled into a water droplet, positioned at the side of the CMUT die, and measured with an optical hydrophone. By using a beam steering approach, the ultrasound generated from 32 CMUT elements were added in-phase to generate a maximum peak-to-peak pressure of 0.9 MPa. Using this pressure, 10 μm latex beads were sorted almost instantaneously.

KEYWORDS

CMUT, Microfluidic particle sorting, Acoustic particle sorting, bulk acoustic wave

INTRODUCTION

Acoustic particle sorting is a label-free, biocompatible method to sort particles within a microchannel. Such techniques are useful for manipulating micron-size cells or sub-micron size particles for clinical, biological, and chemical research. The two common methods to achieve acoustic particle sorting are either to use bulk acoustic wave (BAW) or surface acoustic wave (SAW). BAW-based sorting devices use a single lead zirconate titanate (PZT) element attached to a microfluidic device fabricated from a high acoustic impedance material, such as silicon or glass [1]. The width of the microfluidic channel is designed to be an integer multiple of half of the acoustic wavelength, which creates a standing wave within the acoustic channel to sort particles. SAW-based sorting devices use an interdigitated transducer (IDT) fabricated through deposition and patterning of a thin piezoelectric layer. Due to this photopatternable fabrication process, the acoustic actuation area can be well controlled, therefore SAW-based devices are often preferred when they are integrated with other functionalities. However, SAW-based devices have a low throughput because the acoustic signal is weakly coupled into the microfluidic channel either through the top or bottom surface. Therefore, there is a need for a BAW-based sorting device which can allow high throughput particle sorting, while maintaining high control over the acoustic actuation area.

Over the last decade, in the field of ultrasound imaging, there has been great improvement in MEMS based ultrasonic transducers (i.e., piezoelectric

micromachined ultrasonic transducers (PMUTs) and capacitive micromachined ultrasonic transducers (CMUTs)). These transducers are meant to couple ultrasound waves into the medium in contact with the transducers. However, during our preliminary investigations using CMUTs, it was noticed that acoustic energy can also couple into the silicon substrate and propagate laterally in-plane through the substrate. For ultrasound imaging, this would create an unwanted imaging artifact. On the other hand, for acoustic particle sorting, the in-plane ultrasound is another method to generate ultrasound within a microchannel on the same substrate. In addition, CMUTs are broadband devices which compared to PZT devices allow for an extra degree of freedom to manipulate particles within the microchannel. Furthermore, CMUT technology is highly compatible with silicon microfluidics; a growing field where silicon is used as the substrate to integrate complex functionalities such as cell manipulation, cancer detection, and DNA amplification [2], [3].

In this work, we propose a BAW-based particle sorting device using collapse-mode CMUTs. BAW generated in the in-plane direction of the silicon substrate will enable higher throughput particle sorting. CMUTs are fabricated through standard IC-based fabrication techniques and the acoustic actuation area can be well-controlled.

This paper is organized as follows. First, the concept of the device with CMUTs combined with a silicon embedded microchannel is explained. Then the sidewall acoustic pressure is measured from a CMUT die. Finally, the alignment of 10 μm particles is demonstrated.

DEVICE CONCEPT

The main components of a BAW-based microfluidic particle sorting device are the microfluidic channel and the CMUT. In this section, these two components will be explained.

CMUTs

A schematic cross-section of a CMUT is shown in Fig. 1a. A CMUT consists of a top and bottom circular membrane, each fabricated from an aluminum electrode which is passivated by a ceramic layer such as SiO_2 and Si_3N_4 [4]. At its non-biased state, the CMUT has a vacuum gap between its top and bottom membrane. The top membrane is brought into collapse-mode operation by applying a DC bias voltage beyond the pull-in voltage. Then an AC signal is superimposed to vibrate the donut-shaped region around the collapsed area. The ultrasound generated from this vibration couples into the substrate through the collapsed region. The ultrasound signal then propagates along the in-plane direction of the substrate.

Silicon embedded microchannels

To efficiently couple the ultrasound energy into a microfluidic channel, the channel must be fabricated on the same substrate, as shown in Fig. 1a. In our prior work, we developed techniques to fabricate silicon embedded microchannels with vertical walls through a standardized IC-based fabrication process [5]. In this work, these microchannels were not fabricated because the goal was to measure if sufficient sidewall acoustic pressure is generated. Yet CMUT technology and silicon embedded microchannels could be readily combined in future work.

Beam steering

Another benefit of using CMUTs is that the output pressure could be amplified by applying a beam steering approach. To explain this, in Fig. 1b several rows of CMUTs are aligned in parallel. Each row is referred to as a CMUT element and can be addressed with different driving voltages. Beam steering is achieved by incrementally delaying the same driving signal for each CMUT element with Δt , such that the ultrasound signal traveling through the substrate is added in phase. In this way, a higher output pressure can be achieved. The ultrasound waves will add in phase if the following equation is satisfied,

$$V = D/\Delta t \quad (1)$$

where D is the pitch between each element and V is the velocity of sound through the substrate. For silicon, V is dependent on the crystal orientation and the vibrational modes that are present. The CMUT devices used in this work have the $\langle 110 \rangle$ orientation perpendicular to the CMUT element, as shown in Fig. 1b. The vibrational mode is not clear and multiple vibrational modes could simultaneously exist. Therefore, in this work, Δt is swept to find the best beam steering condition.

RESULT

In this section, the results of acoustic pressure measurements from the side of a CMUT die are presented for a single element and 32 elements with and without beam steering. This is followed by a demonstration of 10 μm particle sorting.

Single element acoustic pressure measurement

Fig. 2a shows the experimental setup used for the acoustic sidewall pressure measurement of the CMUT. A zoomed picture of the CMUT device is shown inside the red box. The diameter of the CMUT membrane used in this

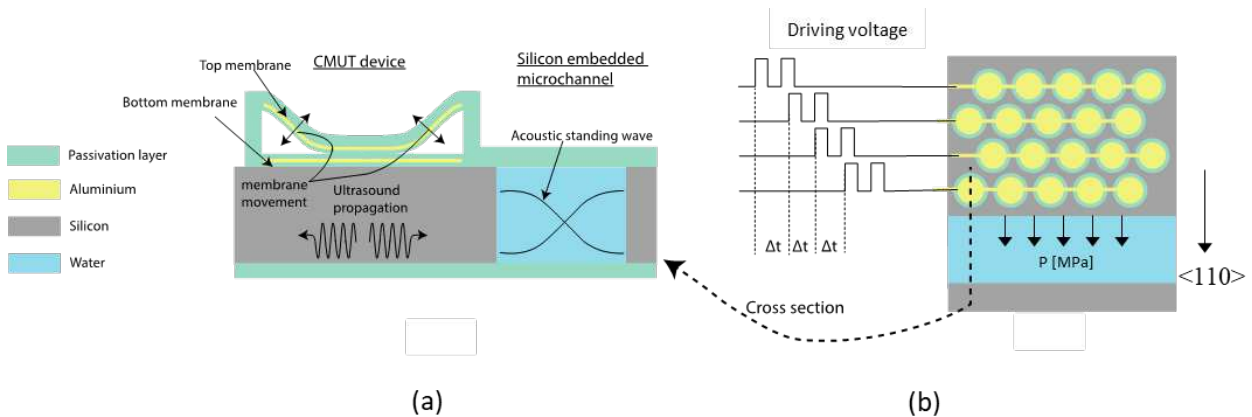


Figure 1: (a) The concept of combining ultrasound transducers with silicon embedded microchannels. (b) The concept of beam steering with a time delay of Δt and the $\langle 110 \rangle$ crystal orientation of the silicon substrate.

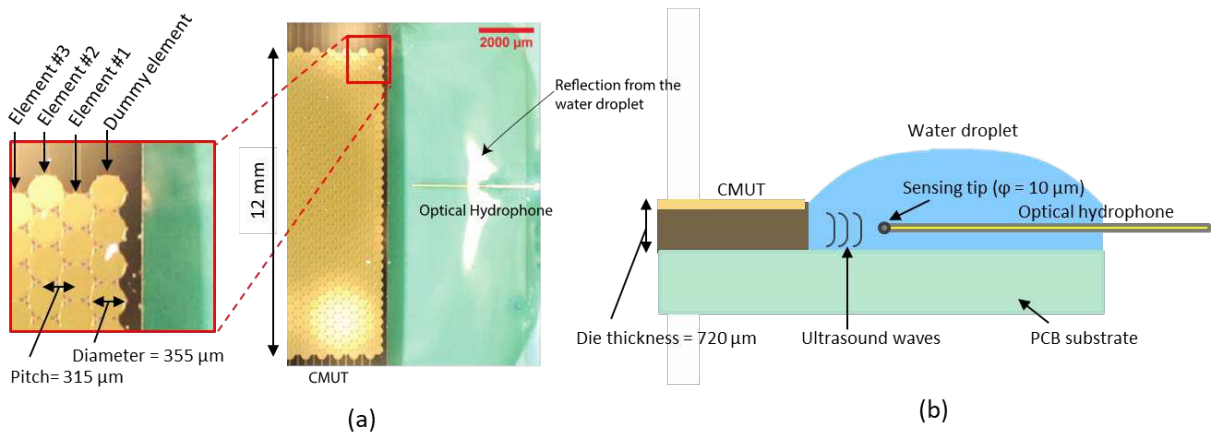


Figure 2: (a) Acoustic pressure measurement setup seen from above. An optical hydrophone is positioned at the side of the CMUT die and a zoomed in image of the CMUT devices are shown in the red box. (b) Side view of the acoustic pressure measurement setup. The drawing is not to scale.

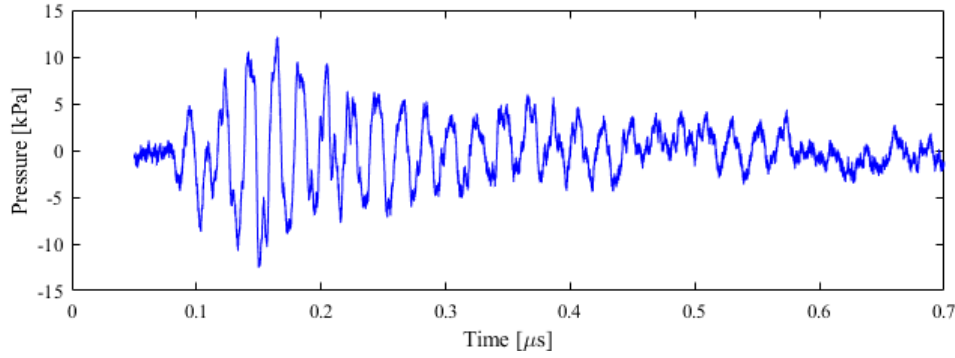


Figure 3: Transient waveform of the pressure from the side of the silicon die. Time = 0 μ s is when the ultrasound signal was transmitted.

work is 355 μ m. Each CMUT element has a length of 12 mm, with 33 CMUT devices in each element. These CMUT elements were positioned in a row with a pitch of 315 μ m along the 2 cm width of the die. The first element at the very edge of the die is a dummy element and cannot be used.

Fig. 2b schematically shows the side view of the experimental setup. The thickness of the silicon die was 720 μ m. A droplet of water was placed at the die's right side, and the surface tension kept the water in place. The acoustic pressure coupled from the silicon substrate into the water was measured with a fiber optic hydrophone (Precision Acoustics, UK) with a tip size of 10 μ m diameter. The hydrophone was carefully positioned with a motorized 3D axis stage. The distance between the hydrophone and the silicon sidewall was approximately 0.9 mm. In the vertical direction, the hydrophone was positioned near half the height of the CMUT. The output pressure was relatively insensitive to the vertical position of the hydrophone.

Fig. 3 shows a transient response when the 2nd CMUT element closest to the sidewall (element #2 in Fig. 1a) was driven with one cycle of sine wave at 4.5 MHz with 15 V amplitude and a bias voltage of 150 V. The response showed a ringing behavior because the CMUT membrane was in resonance at this frequency. The maximum peak-to-peak output pressure was 25 kPa.

To further increase the acoustic pressure, beam steering was applied using the first 32 CMUT elements closest to the water droplet. The in-house-built ultrasound driver system was based on the HV7351 pulser chip (Microchip Technology, USA). The driving signal was a unipolar square wave with 15 V amplitude, 15 cycles, 4.5 MHz frequency, a pulse repetition frequency (PRF) of 1 kHz and a bias voltage of 150 V. The acoustic pressure was measured as the Δt was increased from 5 ns to 150 ns in 5 ns steps. From Fig. 4, the output pressure constructively interfered when $\Delta t = 40$ ns and 65 ns. This corresponds to a sound velocity within silicon at 7875 m/s and 4846 m/s respectively based on equation (1). The maximum peak-to-peak pressure was 0.9 MPa. For comparison, the output pressure of 32 CMUT elements without beam steering is shown in Fig. 4 with a dashed line ($\Delta t = 0$ ns). The peak-to-peak output pressure was 140 kPa which was 6.4 times lower than when beam steering was applied.

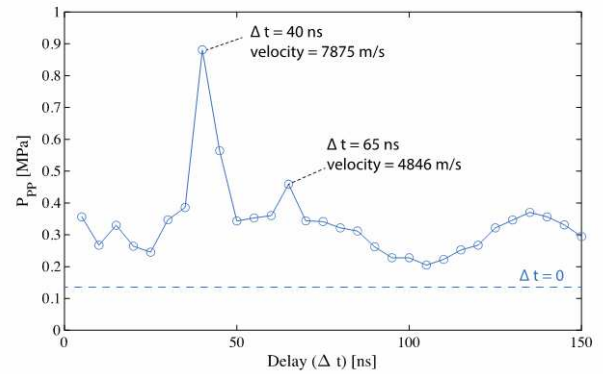


Figure 4: Peak-to-peak pressure when beam steering was applied with a time delay from $\Delta t = 5$ ns to 150 ns in 5 ns steps. $\Delta t = 0$ ns is the peak-to-peak pressure without beam steering.

Particle sorting

Fig. 5a, is the microscope view of the experimental setup used to demonstrate particle sorting. A droplet of water with 10 μ m latex beads was positioned next to the CMUT with a glass reflector at a 4 mm distance from the sidewall of the CMUT. To increase the contrast of the latex beads a thin silicon wafer with a thickness of 280 μ m was positioned beneath the water droplet. In the beginning, the particles were mixed, and there were no distinct patterns. The ultrasound was then turned on for a few seconds, using the same beam steering conditions found to generate the maximum output pressure ($f = 4.5$ MHz, $\Delta t = 40$ ns, $V_p = 15$ V, $V_{bias} = 150$ V, 15 cycles). The PRF was increased to 5 kHz for a slightly higher output power resulting in a duty cycle of 1.7 %. The effect of the ultrasound field on the particles is shown in Figure 5b. The particles aligned in stripes of 166 μ m pitch, which corresponds to half of the wavelength of 4.5 MHz ultrasound in water. The video recording of particle alignment can be seen in the link in the footnote¹. The video is not fast-forwarded. In the video, interesting streaming effects are also visible, but the study of this phenomenon was beyond the scope of this work.

DISCUSSION AND CONCLUSION

In this work, particle sorting using collapse-mode CMUTs was demonstrated for the first time. A beam steering approach was used to increase the output pressure.

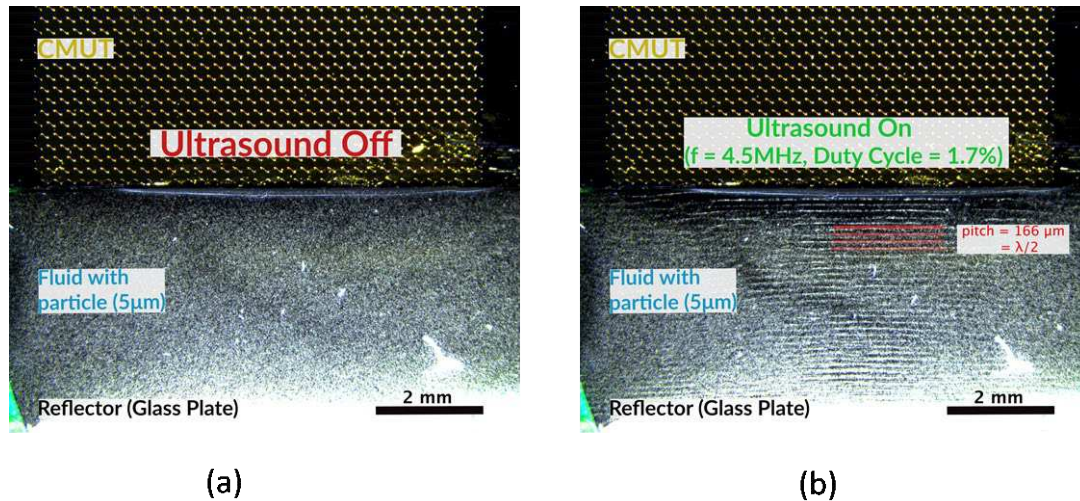


Figure 5: Ultrasound 10 μm latex beads sorting, (a) before the ultrasound and (b) after the ultrasound. The ultrasound parameter used: $f = 4.5 \text{ MHz}$, $\text{PRF} = 5 \text{ kHz}$, $V_p = 15 \text{ V}$, $V_{\text{bias}} = 150 \text{ V}$, $\text{Duty Cycle} = 1.7\%$, $\Delta t = 40 \text{ ns}$, 32 elements, and cycle number = 15. The video can be seen in the link in the footnote¹.

This improved the output pressure by 6.4 times compared to when no beam steering was applied. The maximum output peak-to-peak pressure of 0.9 MPa is much higher compared to prior work on acoustofluidic separation [6] and would allow higher throughput particle sorting.

However, there are still many unanswered questions regarding the mechanism of this sidewall acoustics. The time delay used for beam steering provided some insight on the velocity of the ultrasound wave travelling through silicon (i.e., 7875 m/s and 4846 m/s). According to [7] the ultrasound propagation along the $\langle 110 \rangle$ crystal orientation for longitudinal and transversal velocity is 9138 (m/s) and 4675 (m/s) respectively. The fact that there are two distinct peaks in Fig. 4 may be related to the two different velocity seen in literature, but the exact values do not match. Thus, it is difficult to make concrete statements whether we are using BAW or SAW. However, the hydrophone was vertically positioned near half the height of the die and there were no large changes when the hydrophone was moved vertically. Therefore, we expect that the ultrasound is transmitted from the entire sidewall which confirms that this is a BAW-based sorting device.

There are several other factors that also play a role in this work. For example, i) the ultrasound wave generated from the collapse-mode CMUT will propagate vertically within the substrate, ii) ultrasound waves will reflect internally at the boundary of the silicon substrate and may add coherently, iii) the acoustic driving parameters such as PRF and acoustic frequency may also have an influence. Thus, deepening our understanding of these mechanisms require a more detailed model and should be considered for future work.

ACKNOWLEDGEMENTS

The authors would like to thank the researchers working at Philips research. This project is funded by the ULIMPIA and Moore4Medical projects. ULIMPIA is labelled as a Penta Project Endorsed by Eureka under Penta cluster number E!9911 References. Moore4Medical receives funding from the ECSEL JU, under grant

agreement H2020-ECSEL-2019-IA-876190.

REFERENCES

- [1] Y. Gao, M. Wu, and Y. Lin, "Acoustic Microfluidic Separation Techniques and Bioapplications : A Review," 2020.
- [2] H. M. Ji, V. Samper, and Y. Chen, "Silicon-based microfilters for whole blood cell separation," pp. 251–257, 2008, doi: 10.1007/s10544-007-9131-x.
- [3] K. De Wijs *et al.*, "Micro vapor bubble jet flow for safe and high-rate fluorescence-activated cell sorting," *Lab Chip*, vol. 17, no. 7, pp. 1287–1296, 2017, doi: 10.1039/c6lc01560c.
- [4] M. Pekař, W. U. Dittmer, N. Mihajlović, G. van Soest, and N. de Jong, "Frequency Tuning of Collapse-Mode Capacitive Micromachined Ultrasonic Transducer," *Ultrasonics*, vol. 74, pp. 144–152, 2017, doi: 10.1016/j.ultras.2016.10.002.
- [5] M. Kluba, A. Arslan, R. Stoute, J. Muganda, and R. Dekker, "Single-Step CMOS Compatible Fabrication of High Aspect Ratio Microchannels Embedded in Silicon," *Proceedings*, vol. 1, no. 10, p. 291, 2017, doi: 10.3390/proceedings1040291.
- [6] P. Zhang, H. Bachman, A. Ozcelik, and T. Jun Huang, "Acoustic Microfluidics," *Annu. Rev. Anal. Chem.*, vol. 13, no. 1, pp. 17–43, 2020, doi: 10.1146/annurev-anchem-090919-102205.Acoustic.
- [7] M. K. Song and K. Y. Jhang, "Crack detection in single-crystalline silicon wafer using laser generated Lamb Wave," *Adv. Mater. Sci. Eng.*, vol. 2013, 2013, doi: 10.1155/2013/950791.

CONTACT

*Shinnosuke Kawasaki, tel: +31-6-30846976; shinnosuke.kawasaki@philips.com

¹ Acoustic particle sorting with CMUTs. (<https://youtu.be/NknlrxfTna8>)

BIBLIOGRAPHY

- [1] Y. Shen, Y. Yalikhun, and Y. Tanaka, "Recent advances in microfluidic cell sorting systems," *Elsevier, Sensors and Actuators B: Chemical*, vol. 282, pp. 268–281, 2019.
- [2] S.-J. Lo and D.-J. Yao, "Get to understand more from single-cells: Current studies of microfluidic-based techniques for single-cell analysis," *International Journal of Molecular Sciences*, vol. 16, pp. 16 763–16 777, 2015.
- [3] R. Stoute, J. Muganda, S. Dahar, A. Arslan, R. Henderikx, P. van Stiphout, J. den Toonder, and R. Dekker, "Cmos compatible embedded microchannels," *20th International Conference on Miniaturized Systems for Chemistry and Life Sciences, MicroTAS 2016*, pp. 164–167, 2016.
- [4] P. engineering solutions. Capacitive micromachined ultrasonic transducers. [Online]. Available: <https://www.engineeringsolutions.philips.com/looking-expertise/mems-micro-devices/mems-micro-devices-applications/capacitive-micromachined-ultrasonic-transducers-cmut/>
- [5] Y. Gao, M. Wu, Y. Lin, and J. Xu, "Acoustic microfluidic separation techniques and bioapplications: A review," *Micromachines*, vol. 11, pp. 1–21, 2020.
- [6] M. Evander, "Cell and particle trapping in microfluidic systems using ultrasonic standing waves," Ph.D. dissertation, Department of Electrical Measurements and Industrial Engineering and Automation, Lund University, 2008.
- [7] M. Wiklund, R. Green, and M. Ohlina, "Acoustofluidics 14: Applications of acoustic streaming in microfluidic devices," *Lab on Chip*, vol. 12, pp. 2438–2451, 2012.
- [8] A. Lenshof, M. Evander, T. Laurell, and J. Nilsson, "Acoustofluidics 5: Building microfluidic acoustic resonators," *Lab on a Chip*, vol. 12, pp. 684–695, 2012.
- [9] J. Shi, H. Huang, Z. Stratton, Y. Huang, and T. J. Huang, "Continuous particle separation in a microfluidic channel via standing surface acoustic waves (ssaw)," *Lab on Chip*, vol. 9, pp. 3354–3359, 2009.
- [10] Y. C. Liqiang Ren and, P. Li, Z. Mao, P.-H. Huang, J. Rufo, F. Guo, L. Wang, J. P. McCoy, S. J. Levine, and T. J. Huang, "A high-throughput acoustic cell sorter," *Lab on Chip*, vol. 15, pp. 3870–3879, 2015.
- [11] G. Liu, F. He, Y. Li, H. Zhao, X. Li, H. Tang, Z. Li, Z. Yang, and Y. Zhan, "Effects of two surface acoustic wave sorting chips on particles multi-level sorting," *Biomedical Microdevices*, vol. 21, p. 1–15, 2019.
- [12] K. Mutafooulos, P. Spink, C. Lofstrom, P. Lu, H. Lu, J. Sharpe, T. Franke, and D. A. Weitz, "Traveling surface acoustic wave (tsaw) microfluidic fluorescence activated cell sorter (μ facs)," *Lab on Chip*, vol. 14, pp. 2435–2443, 2019.
- [13] Y. Chen, M. Wu, L. Ren, J. Liu, P. H. Whitley, L. Wang, and T. J. Huang, "High-throughput acoustic separation of platelets from whole blood," *Lab on Chip*, vol. 16, pp. 3466–3472, 2016.
- [14] M. Pekař, S. H. Nispen, R. H. Fey, S. Shulepova, N. Mihajlović, and H. Nijmeijer, "A fluid-coupled transmitting cmut operated in collapse mode: Semi-analytic modeling and experiments," *Sensors and Actuators A: Physical*, vol. 267, pp. 474–484, 2017.

- [15] S. Olcum, M. Senlik, and A. Atala, "Optimization of the gain-bandwidth product of capacitive micromachined ultrasonic transducers," *IEEE transactions on ultrasonics, ferroelectrics, and frequency control*, vol. 52, pp. 2211–2219, 2005.
- [16] P. Zhang, H. Bachman, A. Ozcelik, and T. J. Huang, "Acoustic microfluidics," *Annual Review of Analytical Chemistry*, vol. 13, pp. 17–43, 2020.
- [17] "Microfluidics market size, share trends analysis report by technology (medical, non-medical), by application (lab-on-a-chip, organs-on-chips), by material (polymer, silicon, glass, pdms), by region, and segment forecasts, 2021 - 2028," 2021.
- [18] G. V. Research. Microfluidics market size, share trends analysis report by technology (medical, non-medical), by application (lab-on-a-chip, organs-on-chips), by material (polymer, silicon, glass, pdms), by region, and segment forecasts, 2021 - 2028. [Online]. Available: <https://www.grandviewresearch.com/industry-analysis/microfluidics-market>
- [19] E. Roy, A. Pallandre, B. Zribi, M. Horny, F. D. Delapierre, A. Cattoni, J. Gamby, and A. Haghiri-Gosnet, "Overview of materials for microfluidic applications," in *Advances in Microfluidics: New Applications in Biology, Energy, and Materials Sciences*, X.-Y. Yu, Ed. IntechOpen, 2016, pp. 336–355.
- [20] Elveflow. Microfluidics: A general overview of microfluidics. [Online]. Available: <https://www.elveflow.com/microfluidic-reviews/general-microfluidics/a-general-overview-of-microfluidics/>
- [21] B. Mimoun, V. Henneken, A. van der Horst, and R. Dekker, "From microfluidics for biotechnology to biomicrofluidics," *IEEE Sensors Journal*, vol. 13, pp. 3873–3882, 2013.
- [22] T. Franke, S. Braunnüller, L. Schmid, A. Wixforth, and D. A. Weitz, "Surface acoustic wave actuated cell sorting (sawacs)," *Lab on Chip*, vol. 10, pp. 789–794, 2014.
- [23] A. Nilsson, F. Petersson, H. Jönssonband, and T. Laurell, "Acoustic control of suspended particles in micro fluidic chips," *Lab on Chip*, vol. 4, pp. 131–135, 2004.
- [24] A. Fornell, K. Cushing, J. Nilsson, and M. Tenje, "Binary particle separation in droplet microfluidics using acoustophoresis," *Applied Physics Letters*, vol. 112, pp. 063701–1–4, 2018.
- [25] Overview of acoustofluidics," overview of acoustofluidics — acoustofluidics lab. [Online]. Available: <https://acoustofluidics.pratt.duke.edu/research/overview-acoustofluidics#:~:text=Acoustofluidics%20has%20a%20combination%20of%20advantages%20that%20competing,particle%20manipulation%20and%20compatibility%20with%20other%20lab-on-a-chip%20components.>
- [26] R. K. Bansal. Difference between laminar flow and turbulent flow. [Online]. Available: <https://www.hkdivedi.com/2018/08/difference-between-laminar-flow-and.html#:~:text=Difference%20between%20Laminar%20flow%20and%20Turbulent%20flow%20,in%20turbu%20...%20%203%20more%20rows%20>
- [27] H. Bruus, "Acoustofluidics 1: Governing equations in microfluidics," *Lab on a Chip*, vol. 11, pp. 3742–3751, 2011.
- [28] F. Barbaresco, L. Racca, L. Spigarelli, M. Cocuzza, S. L. Marasso, C. F. Pirri, and G. Canavese, "Focalization performance study of a novel bulk acoustic wave device," *Nanomaterials*, vol. 11, pp. 2630:1–20, 2021.

- [29] A. Fornell, P. Söderbäck, Z. Liu, M. D. A. Moreira, and M. Tenje, "Fabrication of silicon microfluidic chips for acoustic particle focusing using direct laser writing," *Micromachines*, vol. 11, pp. 1–13, 2020.
- [30] G. P. Gautam, T. Burger, A. Wilcox, M. J. Cumbo, S. W. Graves, , and M. E. Piyasena, "Simple and inexpensive micromachined aluminum microfluidic devices for acoustic focusing of particles and cells," *Anal Bioanal Chem.*, vol. 410, pp. 3385–3394, 2019.
- [31] G. Destgeer, K. H. Lee, J. H. Jung, A. Alazzamb, and H. J. Sung, "Continuous separation of particles in a pdms microfluidic channel via travelling surface acoustic waves (tsaw)," *Lab on Chip*, vol. 13, p. 4210–4216, 2013.
- [32] N. G. Durmuş, R. L. Lin, M. Kozberg, D. Dermici, A. Khademhosseini, and U. Demircit, "Acoustic-based biosensors," in *Encyclopedia of Microfluidics and Nanofluidics*, D. Li, Ed. Springer, 2015, pp. 28–39.
- [33] A. S. Ergun, X. Zhuang, Y. Huang, O. Oralkan, G. G. Yaralioglu, and B. Khuri-Yakub, "Capacitive micromachined ultrasonic transducer technology for medical ultrasound imaging," *Proceedings of SPIE - The International Society for Optical Engineering*, vol. 5750, pp. 58–68, 2005.
- [34] K. ya Hashimoto, *Surface Acoustic Wave Devices in Telecommunications*. Springer-Verlag Berlin Heidelberg GmbH, 2000.
- [35] M.-K. Song and K.-Y. Jhang, "Crack detection in single-crystalline silicon wafer using laser generated lamb wave," *Advances in Materials Science and Engineering*, vol. 2013, pp. 1–6, 2013.
- [36] F. Laermer, S. F. abd Lauri Sainiemi, and K. Kolari, "Deep reactive ion etching," in *Handbook of Silicon Based MEMS Materials and Technologies (Second Edition)*, M. Tilli, T. Motooka, V.-M. Airaksinen, S. Franssila, M. Paulasto-Kröckel, and V. Lindroos, Eds. Willium Andrew, 2015, p. 469.
- [37] X. Ding, Z. Peng, S.-C. S. Lin, M. Geri, S. Li, P. Li, Y. Chen, M. Dao, S. Suresh, and T. J. Huang, "Cell separation using tilted-angle standing surface acoustic waves," *PNAS*, vol. 111, pp. 12 992–12 997, 2014.